DIRECT NUMERICAL SIMULATION OF 3D SPARSE MULTISCALE GRID GENERATED TURBULENCE AND KINEMATIC SIMULATION OF INERTIAL PARTICLE PAIR DIFFUSION

BY

SYED MUHAMMAD USAMA

A Dissertation Presented to the

DEANSHIP OF GRADUATE STUDIES

KING FAHD UNIVERSITY OF PETROLEUM & MINERALS

DHAHRAN, SAUDI ARABIA

In Partial Fulfillment of the
Requirements for the Degree of

DOCTOR OF PHILOSOPHY

In
MATHEMATICS

JANUARY 2019

KING FAHD UNIVERSITY OF PETROLEUM & MINERALS
DHAHRAN 31261, SAUDI ARABIA

DEANSHIP OF GRADUATE STUDIES

This dissertation, written by **SYED MUHAMMAD USAMA** under the direction of his dissertation adviser and approved by his dissertation committee, has been presented to and accepted by the Dean of Graduate Studies, in partial fulfillment of the requirements for the degree of **DOCTOR OF PHILOSOPHY IN MATHE-MATICS**.

Dissertation Committee

Dr. Nadeem A. Malik (Adviser)

Dr. Mustapha Kassem (Co-Adviser)

Dr. Ashfaque H. Bokhari (Member)
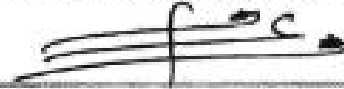
Dr. Faisal A. Fairag (Member)

Dr. Fiaz Ud Din Zaman (Member)

Dr. Husain Al-Attas
Department Chairman

Dr. Salam A. Zummo
Dean of Graduate Studies

25/4/19

Date

Dedicated to the memory of my mother

ACKNOWLEDGMENTS

TABLE OF CONTENTS

LIST OF TABLES

LIST OF FIGURES

xiv

DISSERTATION ABSTRACT

NAME: Syed Muhammad Usama

TITLE OF STUDY: Direct Numerical Simulation of 3D Sparse Multiscale Grid Generated Turbulence and Kinematic Simulation of Inertial Particle Pair Diffusion

MAJOR FIELD: Mathematics

DATE OF DEGREE: January 2019

Fundamental problems in turbulence were investigated using numerical methods. For the first time, a new type of turbulence generating grid, the Sparse 3D Multiscale Grid Turbulence Generator [Malik, N. A. Patent US 9,599,269 B2, (2017); Malik N. A. Patent EP 2,965,805 B1, (2017)], or 3DS for short, is investigated using Direct Numerical Simulations (DNS). In the 3DS each scale in a (typically) fractal grid is held in its own co-frame and is separated from the next co-frame by some distance in an overall co-planar arrangement. This expands the parameter space in the 3DS as compared to 2D flat fractal grids (2DF) and classical regular grids (RG). The objective is that the 3DS system could provide better control of turbulence than previous grids. Turbulence characteristics downstream of all three grids placed in a conduit

with periodic walls and inflow and outflow in the streamwise direction are compared for Kolmogorov scale Reynolds number $Re_\eta = 300$. The blockage ratio (solidity) of the RG and 2DF grids was $\sigma = 32\%$, while in the 3DS it was varied: $\sigma_{3DS}^{Max} = 15\%$, 24%, and 32%. Variations in the ordering of the co-frames in the 3DS for the case: $\sigma_{3DS}^{Max} = 32\%$ was also investigated. However, the separation distances between the three co-frames were kept constant throughout this work. It was found that: (1) the 3DS generates much higher peak turbulence intensities, $I = u'/U_{mean}$, than the RG and 2DF for the same blockage ratio. (2) 3DS with $\sigma_{3DS}^{Max} = 24\%$ is closest to the performance of the 2DF. (3) The downstream turbulence can be divided in to three regions: (a) near-field region close to the grid where the turbulence is generated, (b) the intermediate region where the turbulence decays rapidly, (c) the far-field region downstream where the turbulence intensity is sustained and even increases along the channel centerline. (4) There exists a central core region around the centerline which is approximately homogeneous and isotropic in the far-field. (5) The main mechanism that sustains the turbulence intensity in the far-field is re-entrainment of turbulent fluid from outside of the central core region in to it; if the rate of entrainment is high enough then the turbulence intensity may increase downstream. (6) The order of arrangement of co-frames in the 3DS has comparatively less effect on the turbulence intensities than changes in blockage ratio, the case with decreasing scales (the natural case) produces the highest intensities. (7) Fully developed Kolmogorov spectrum was observed in the 3DS systems with blockage ratio 32%, but the best spectrum was in the natural case. (8) The distribution of vorticity intensity $I_\omega(x) = \|\omega'\| L/U_{mean}$ shows much less variation suggesting that vorticity generation plays a relatively weak role

in 3DS systems. (9) Passive scalar transport was investigated for different Schmidt numbers $0.25 \leq Sc = \nu/D \leq 2$; the overall trends in scalar fluctuations decay were similar in all 3DS systems. In a second part of this study, a new theory for turbulent inertial particle pair diffusion in the inertial subrange was postulated and investigated numerically using Kinematic Simulations (KS) [N. A. Malik, PLoS ONE, 10(10): e0189917 (2017)]. The new theory is an extension of the non-local fluid particle pair diffusion theory; here we postulate that for all Stokes numbers, in the limit of heavy point particles released close together inside the inertial subrange, with one-way coupling, pair separation will be ballistic because the particle kinetic energy dominates over the small scale turbulence energy, and the pair diffusion coefficient will scale like $K_p(l) \sim l$ where l is the pair separation variable. As the particle pair separation increases, and if the subrange is large enough, the pair diffusion transits slowly towards the fluid pair diffusion, $K_p(l) \rightarrow K_f(l) \sim l^\gamma$, which has been shown to follow non-Richardson scaling laws because of non-local effects [Malik, N. A. PLoS ONE (2018)] with $\gamma > 4/3$ for Kolmogorov turbulence. By considering the balance of momentum and energies, the transition length scale l_c at which the ballistic regime starts to transit towards the non-ballistic regimes scales like, $l_c/\eta \sim St^{0.5}$ if $St < 1$, and scales like $l_c/\eta \sim St^1$ if $St > 1$, where η is the Kolmogorov scale; a crossover between these two scalings occurs at $St = 1$. All of the predictions of the new theory have been confirmed numerically using KS.

ملخص الرسالة

الاسم: سيد محمد اسامه

عنوان الدراسة: دايركت نوميريكل سيموليشن من اضطراب بالثلاثية الأبعاد سبارس متعددة النطاقات المتولدة بالشبكة و كيناميتك

سيموليشن من نشر من زوج من الجسيمات بالقصورالذاتي

التخصص: الرياضيات

تاريخ الدرجة العلمية: يناير 2019

في هذه الأطروحة يتم إجراء محاكاة عددية مباشرة للاضطراب الذي تولده الشبكات متعددة الحواس باستخدام حوسبة عالية الأداء. يتم تحليل الناتج الناتج عن هذه المحاكاة ومقارنتها بالأدبيات التجريبية والعددية ذات الطبيعة المتشابهة. تم التحقق من صحة النتائج القديمة وتم التأكيد على أنه بالنسبة لنفس نسبة الانسداد ، تكون شدة الاضطراب الناتج عن الشبكة المربعة الفركتالية أعلى من الشبكة العادية الكلاسيكية. تم تقديم فئة جديدة من الشبكات متعددة القياسات ، وهي ثلاثة شبكات متعددة الأبعاد متفرقة الأبعاد ، وهي تعميم للشبكات الفركتالية ، بمعنى أن كل تكرارية متعددة المفاصل للنموذج الفركتالي تكمن في مستوى موازٍ إلى آخر. وبهذه الطريقة ، تضيف المسافات بين كل التكرار الفركتلي إلى مجموعة من المعلمات اللازمة لوصف الشبكات متعددة النقاط المتناثرة ثلاثية الأبعاد ، ومن ثم فهي تعميم للشبكات العادية والفركتالية. المعلمات الرئيسية هي نسبة الانسداد للشبكات ، والحجم الشبكي الفعال ، والمسافة بين تكرار الفركتلات ، وسمك وطول القناة. تمت دراسة تأثير هذه الخصائص الهندسية للشبكات على الخواص الفيزيائية مثل تقلبات السرعة ، وتدرج الضغط ، والجزئيات ، والتناضح الخ. لتدفق القنوات المضطرب. لوحظ ارتفاع كثافة الاضطراب مع تأثير دائم ومزيج أعلى بشكل عام في القناة لشبكات متفرقة بالمقارنة مع الشبكتين المستطقتين. يتم إجراء دراسة حدية لانتشار أزواج الجسيمات بالقصور الذاتي باستخدام المحاكاة الكيميائية على حجم رقم القصدير الغريب و لمراقبة وتوقع قوانين القياس الجديدة التي تحكم هذه الظاهرة.

CHAPTER 1

INTRODUCTION

Fluid mechanics is concerned with the mechanical properties of fluids, forces acting upon them and their movement. It is a challenging phenomenon that scientists and engineers have been investigating for centuries and turbulence is the area in fluid mechanics which is considered one of the most difficult problem in science. The fluid (liquid, gas, plasma etc.) is assumed to be a continuum leaving the information out that it is made up of atoms and molecules and only considering a macroscopic perspective, Turbulence remains a largely unsolved problem in the sense that it is not predictable except in some broad statistical sense. This makes turbulence extremely hard to control and can be hazardous in some cases such as during flight. On the other hand, turbulence is also necessary for life because without it pollen and seeds would not spread far and climate would not be. For this reason control of turbulence is important and highly desirable.

1.1 Literature Review

Turbulence is common in natural flow as well as in engineering fields. Navier-Stokes equations describe the mechanics of fluids as detailed in Section 2.2. Although existence and uniqueness of three-dimensional Navier-Stokes equations is an unsolved problem, it is the best representation of the two most important fluid motions namely laminar flow and turbulent flow. Laminar flow is defined as the flow in which layers of the fluid flow parallel to each other without disruption or perpendicular motion [1]. Laminar flow is smooth, predictable and has parallel layers of fluid flowing over each other forming streamlines [2]. Turbulent flow is chaotic, has eddies and is an agent of mixing (see Figure 1.1). The transition from laminar flow to turbulent flow was experimentally studied for the first time by Reynold in 1880 and it is still an unsolved mystery. Prandtl in 1925 [3] introduced mixing length theory, which states that velocity fluctuation is equal to component of velocity gradient times a length scale. He gave the idea of boundary layer, which is now recognized as fundamental to aerodynamics. Taylor in 1931 [4], developed the theory of statistical approach towards turbulence.

After some groundbreaking contribution by great scientists like Poincare [4], Reynold and Prandtl [5], the Russian Mathematician Kolmogorov in 1941 revolutionized the approach towards turbulence statistics by giving an exact measurement of the rate of homogeneous isotropic turbulence [6]. Other notable names in the 1950's are Burgers [7], Lipschitz [8], Hopf, von Karman, Batchelor [2], Corrsin, Hiesenberg, Landau [5], Lumley, Townsend and Hinz [1]. In the 1970's the use of powerful com-
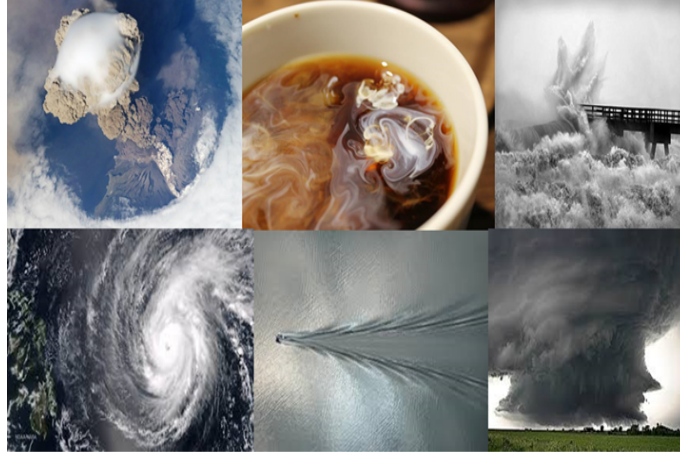
Figure 1.1: Examples of turbulence in nature (left to right) Volcano, cup of tea, barrage, hurricane, boat in the sea and a tornado.

putational tools was a key factor in the development of turbulence studies [9], [10], [11], [12], [13], [14], [4], [15], [16].

In 1970, Deardoff proposed Large eddy simulation model (LES) [17]. In LES large scales are resolved exactly whereas the small scales are modeled. In 1972, Launder et. al. introduced RANS (Reynold's averaged Navier-Stokes equations) in which you solve directly for the mean turbulence quantities [5]. When small scale details are not so important then RANS model is used, as in weather prediction, where as in most of the industrial and engineering applications LES is considered favorable.

Direct Numerical Simulation (DNS) was introduced by Orszag and Patterson in 1972 [18]. DNS is different from LES in that all scales are resolved down to the smallest grid scale. In effect DNS is the exact solution of Navier-Stokes equation to a given resolution [19]. It is more accurate than RANS and LES as there is no modeling involved. DNS is being extensively used as a benchmark for other turbulence experiments and simulations as it produces exact solution at the grid points [20]. Although DNS is highly accurate and simple, it is not applicable in real world problem

solving because it requires very high computing power which comes at high costs and it will continue to be a challenge in the coming years [1].

Onsager (1949) first noted the near singular flow pattern of turbulence [21]. Pioneering works by Novikov (1970), Mandelbrot (1974), Frisch, Sulem and Nelkin (1978), Lundgren (1982), Parisi and Frisch (1985) dealt with this subject theoretically and the common conclusion was that turbulence is multiscale phenomenon and fractal like, and without an 'absolute' self similarity. The same observation was numerically studied by Frisch (1995), Hunt and Vassilicos (1991). Extensions of those results as multifractals and multispirals were developed by Perry, Henbest and Chong (1986). Lesieure and McComb (1990), Smith and Woodruff (1998) and Sain, Pandit and Pandit (1998) made the modifications that enabled the scientists to solve Navier-Stokes equation directly [5]. Classical Regular grids are cross patterns with fixed length, width and thickness that generate turbulence close to the grid [22].

Caratheodory (1914) and Housdorff (1918) gave ideas of non-integer dimensions [23]. The concept of fractals echoed in geometric function theory which has contributed to many areas of pure and applied mathematics with the most recent contribution in solving Fermat's last theorem. Mandelbrot (1970) developed the mathematics of self-similar fractal geometries. DNS was introduced by Fox and Lily (1972), Orzag and Patterson (1972) were among the pioneers in using DNS as a tool [1]. Rogallo (1981) improved the DNS model to include homogeniety in it. Rogallo and Moin (1984) then used those techniques to study near wall behavior of fluid in turbulent flow. Kim et al. performed DNS of plane channel for the first time in 1987. Other contributions came from Moin (1987), Kristoffersson and Andersson (1993), Sumitani and Kasagi

4

(1995), Neves and Moin (1994), Choi et al. and Kasagi et al. (1992). Bradshaw (1994) said that perhaps the biggest fallacy about turbulence is that it can be reliably described (statistically) by a system of equations which is far easier to solve than the full time-dependent three-dimensional Navier-Stokes equations [5]. Feiereisen et al. (1981) studied compressible flows using DNS followed by Lee et al. (1991), Blaisdell et al. (1993), Coleman et al. (1995) and Vreman et al. (1996).

The use of grids as turbulence generators to investigate flow characteristics for better understanding and testing is common place in experimental framework [2]. In the 1980's fractal geometry attracted the attention of the fluid dynamics community and applications were found in grid generated turbulence. Figure 1.2 shows some examples of the fractal patterns found in nature.

Figure 1.2: Examples of fractals in nature (left to right) an ice crystal, cracks in ice, leaves, bronchus, shell, pollen, broccoli, and aloe.

A regular grid (see Figure 3.1) can be completely described by its mesh size and blockage ratio where as fractal grid (see Figure 3.2) requires more parameters for

complete description. Queiros et al. (2001) used fractal grids to generate turbulence in wind and water tunnels. Staicu et al. (2003) studied the effect of fractal grids on the transport of scalars. Experiments on various fractal grids were performed by Hurst and Vassilicos (2007) where they showed that fractal square grids produce higher average turbulence intensity as compared to regular grids and the rate of energy decay of fractal grids does not follow the power law decay of regular grids . Seoud and Vassilicos (2007), Stresing, et al. Mazellier and Vassilicos (2010) performed experiments of similar nature. Discetti, et al., Laizet and Vassilicos, Valente and Vassilicos, (2011) performed experiments as well as simulations to validate the fractal grid turbulence phenomenon. In 2011, Laizet and Vassilicos used DNS to show that fractal square grids show higher turbulence intensity on average as compared to regular grid having the same solidity [24], [13], [17], [22].

Lindstedt et al. (2013) used fractal grids in experiments such as flames and thrust analysis of turbulence. New scaling laws have been formulated for energy decay and some old ones have been validated by Laziet et al. (2015) [12]. Vassillicos et al. (2016) showed that vortex can trap eddies and as a result slow down mixing in grid generated turbulence [25]. Flow quality can be improved by using grid in channel flow both for producing turbulence as well as for regulating it, depending of course on the Reynolds number of the flow. Grid generated turbulence studies have become the new benchmark for turbulence studies as it has provided a new insight into the process and generation of turbulence especially since the emergence of multi-scale grids. Turbulence is a multiscale phenomenon and hence multi-scale grids affect it differently as compared to classical regular ones. Nagata et al. (2017) studied the

effect of multiscale grids on non-equilibrium dissipation of grid generated turbulence using particle image velocimetery [26]. Zhang et al. (2018) recently presented how different scales of fractals effect mixing in channel flow. Malik (2017) generalized fractal grid design by developing the concept of three-dimensional sparse multi-scale grids and this is the main topic of this thesis [27].

1.2 Motivation

Turbulence generated by multi-scale grids is a relatively new idea. Wind tunnel experiments on grids have revealed that regular grid generated turbulence displays high intensity but decays very fast where as fractal grid with the same surface area displays higher average peak intensity and decays more slowly downstream [24], [10]. Computational fluid dynamics (CFD) is a multi-disciplinary area in which fluid flow is simulated for engineering as well as research purposes. It is the biggest consumer of computational resources in the world as this usually means that Navier-Stokes equations are solved on a high resolution domain over a long period of time.

Accurate numerical schemes, code optimization strategies and parallelization techniques are combined to perform massive calculations. Computer Aided Design (CAD) softwares help engineers and scientists to use these packages for practical applications resulting in reduction of prototype testing and costs and experimental complexities. The standard procedure followed in these studies is as follows:

- Observing a fluid dynamics problem.

- Describing the problem.
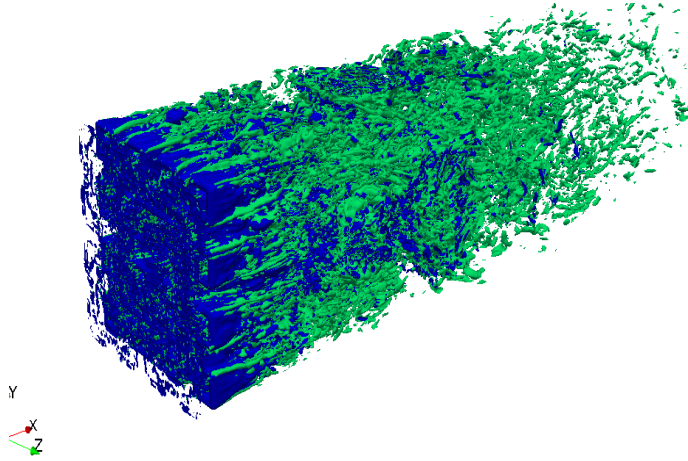
Figure 1.3: Isosurfaces at value 0.5 of normalized vortices in x-direction (in blue) and vorticity magnitude (in green) of fractal grid generated turbulence at a point in time.

- Selecting or developing appropriate discretization scheme and solver.

- Designing the simulation domain and setting up the flow system.

- Providing necessary initial and boundary conditions, fluid properties etc.

- Discretizing the domain using appropriate scheme. (This is very important and time consuming.)

- Running simulation either in serial or on a parallel setup depending upon the size and refinement level for the simulation domain and mesh.

- Post processing and analysis of the results after obtaining numerical solutions once the desired accuracy has been achieved.

Available commercial and open-source CFD packages, cover a vast range of fluid systems with new packages being added on a regular basis. Benchmark level studies of turbulence requires significantly higher computation resources and exceptionally good numerical techniques.

In this work, we have used the latest algorithms on state of the art computation environment to get a better understanding of grid generated turbulence and explored some of its endless possibilities.

1.3 Aims and Objectives

The aim of this investigation is to study a new type of multi-scale turbulence that has been introduced recently, the three dimensional sparse multi-scale grid turbulence generator (3DS) [27] using high performance computing.

- The objective is to use DNS of 3DS generated turbulence in a channel and to compare the turbulence characteristics with those generated by RG and 2DF grids.

- Data generated by DNS will be analyzed and results compared to those by Laizet and Vassilicos [24] for comparison and validation. Since the results of [24] are already validated against experiments [10], it suffices for us to compare our numerical simulations to theirs.

- A parametric study of 3DS for different values of blockage ratios and different grid arrangements will be performed.

- Of particular interest in this study are turbulence characteristics such as intensity, velocity, vorticity and concentration profiles. Also, energy spectra and scalar transport and mixing characteristics will be computed.

Some questions that we address in our investigation are:

- How does the turbulence intensity from 3DS compare to the intensity for same blockage ratio as RG and 2DF grids?

- Does the energy decay region of 3DS depend upon the position and geometry of the grids?

- Is the turbulence generated by 3DS homogeneous and isotropic in any region within the channel?

- Does turbulence generated by 3DS follow the same scaling laws of energy decay as RG and 2DF?

- Which of the three grids causes better mixing in the sense of distribution of scalar concentration?

CHAPTER 2

INTRODUCTION TO

TURBULENCE

2.1   The Phenomenon of Turbulence

Turbulence is one of the most common naturally occurring phenomenon. The flow of fluids is sensitive to many variables such as temperature, pressure, viscosity, density, particles and obstacles and electromagnetism. Turbulent flow is random, essentially three dimensional, multiscale, rotational and strongly dependent on initial and boundary conditions. A journey in this field is challenging, exciting and inspiring. From the scales of microorganisms to atmosphere and beyond, turbulence is extensively studied and applied in all areas of science and technology.

The onset of turbulence can be predicted roughly by Reynolds number $Re = \frac{ul}{\nu}$ which describes the ratio between inertial and viscous forces. When inertial force dominates $Re >> 1$, the flow is turbulent and when viscous force dominates the inertial ones $Re < 1$, then the flow is laminar.

Navier-Stokes equations is an accurate description of the momentum balance for incompressible Newtonian fluids in terms of mass and momentum conservation. Newtonian fluid is a fluid whose viscosity does not change with the rate of the flow. Fortunately, most common fluids are Newtonian. However, non-linearity and coupling between pressure and velocity pose immense difficulty in solving the system of equations for which reason computational methods are employed to solve these equations subject to numerical constraints. Another approach is performing experiments which also prove extremely expensive and in most cases, downright impossible, especially at high Reynolds number. Wind tunnel experiments are often used to validate numerical simulation followed by prototype testing. These findings have paved the way for experimental and numerical investigations in grid generated turbulence.

2.2 Navier-Stokes Equations

The Navier-Stokes equations (NSE) can be derived by applying continuum hypothesis on fluids and using conservation of mass and momentum laws on a fluid element such as a cube. NS equations governing three dimensional incompressible flow are given by:

$$\rho \left(\frac{\partial \mathbf{u}}{\partial t} + \mathbf{u}.\nabla \mathbf{u} \right) = -\nabla p + \mu \nabla^2 \mathbf{u} + f, \tag{2.1}$$

$$\nabla.\mathbf{u} = 0, \tag{2.2}$$

where $\nabla = \langle \frac{\partial}{\partial x}, \frac{\partial}{\partial y}, \frac{\partial}{\partial z} \rangle$ is the gradient, $\mathbf{u}(\mathbf{x}, t) = \langle u, v, w \rangle (\mathbf{x}, t)$ is the velocity vector, p is pressure, ρ is density (constant), μ is dynamic viscosity and f is any

external force such as gravity.

Exact or analytic solution of this system of equations in 2D or 3D are very few, even under very restrictive conditions for example the analytic solution of burger's equation in cartesian coordinates. The reason is non-linearity through the advection term and non-locality through the pressure gradient term, and also the velocity pressure coupling. Equation (2.1) is the momentum conservation equation describing Newton's second law of motion. The left hand side of the equation is the total derivative of velocity consisting of time derivative and convection term.

$$\frac{D}{Dt} = \frac{\partial}{\partial t} + \mathbf{u} \cdot \nabla \tag{2.3}$$

On the right hand side of equation (2.1) we have the pressure gradient, the diffusion and the external force. For time dependent three dimensional flow, independent variables are x, y, z and t where as p and $\mathbf{u}$ are the dependent variables, so the incompressibility constraint (2.2) and momentum equation (2.1) are a system of four non-linear, second order, partial differential equations with four independent variables and four unknowns which together with initial fields and appropriate boundary conditions can be solved numerically.

Euler equations are a special ideal case of NS equations with $\mu = 0$ meaning the fluid has no viscosity. This marks a clear distinction between a fluid with no viscosity and a fluid where viscosity approaches to zero, because the order of the spatial differentiation is reduced from second order to first order only when $\mu = 0$.

It is a good idea to reduce the number of parameters in NS equations by non-

dimensionalization. If L, U and L/U are characteristic length, velocity and time scales respectively then (2.1) is non-dimensionalized as:

$$\frac{\partial \mathbf{u}^*}{\partial t^*} + (\mathbf{u}^* \cdot \nabla^*)\mathbf{u}^* = -\nabla^* p^* + \frac{1}{Re}\nabla^{*2}\mathbf{u}^* + f^* \qquad (2.4)$$

where $\mathbf{u}^* = \mathbf{u}/U$, $t^* = Ut/L$, $p^* = p/\rho U^2$, $\nabla^* = L\nabla$ and Reynolds Number

$$Re = \frac{\rho U L}{\mu} \qquad (2.5)$$

Re is the ratio of inertial forces to the viscous forces and in turbulent flow, inertial forces dominate viscous forces and thus turbulent flows are high Reynolds number flows as evident from the scaled Navier-Stokes Equations.

At the end of this section it is important to mention that for three dimensional Navier-Stokes equations, long time existence of weak solution has been established but uniqueness has not been proven up till now [28]. Uniqueness of only short time strong solution is established but the existence and uniqueness of regular solution to the Navier-Stokes equations has been an unsolved mathematical problem for over a century [28]. However, from an application point of view, the numerical solution of Navier-Stokes equations when compared with experimental investigation has established these equations as a fruitful approach to fluid mechanical problems over a wide range of parameter values and over a wide range of applications from aerodynamics to turbulent diffusion.

2.3 Reynolds Decomposition

The random motion of fluid masses or eddies describes turbulent flow and therefore a statistical approach to study the phenomenon was inevitable. Reynolds introduced the decomposition of turbulence velocity signal [5], [29] into its mean and fluctuating components in 1884 as

$$\mathbf{u}(\mathbf{x}, t) = U(\mathbf{x}) + \mathbf{u}'(\mathbf{x}, t), \tag{2.6}$$

where $U(\mathbf{x}) = \overline{\mathbf{u}(\mathbf{x}, t)}$ denotes the mean velocity and $\mathbf{u}' = U - \mathbf{u}(\mathbf{x}, t)$ is the turbulent fluctuation velocity.

This defines **turbulence intensity** I given by:

$$I = \frac{k}{U} \tag{2.7}$$

where U is the mean velocity and k is the **turbulence kinetic energy (TKE)** given by

$$k = \sqrt{\frac{1}{3}\left(u_x'^2 + u_y'^2 + u_z'^2\right)} \tag{2.8}$$

where $\mathbf{u}' = \langle u_x', u_y', u_z' \rangle$.

The **temporal average** of $u(x, t)$ where $x \in \Omega \subset R^j$, $j = 2, 3$ and $t > 0$ is given by:

$$\overline{\mathbf{u}} = U(\mathbf{x}) = \lim_{T \to \infty} \frac{1}{T} \int_{t_0}^{t_0 + T} \mathbf{u}(\mathbf{x}, t)\, dt. \tag{2.9}$$

where $t_0 > 0$ is initial time.

The **root mean square velocity fluctuation** is defined as:

$$(u'^2)^{1/2} = \lim_{T \to \infty} \sqrt{\frac{1}{T} \int_0^T [\mathbf{u}'(\mathbf{x}, t)]^2 \, dt,} \qquad (2.10)$$

as a result we get a signal that shows the deviation of velocity from its mean at desired locations in the domain.

Sometimes **spatial averaging** is needed based on the physical requirements. Spatial average at time t of $\mathbf{u}(\mathbf{x}, t)$ is denoted by $\tilde{\mathbf{u}}$ defined as:

$$\tilde{\mathbf{u}}(t) = \frac{1}{V_\Omega} \int_\Omega \mathbf{u}(\mathbf{x}, t) \, d\mathbf{x}. \qquad (2.11)$$

where V_Ω is the volume of the domain.

Consider a sequence $\{\mathbf{u}_j(\mathbf{x}, t)_{j=1}^N\}$ of realizations of $\mathbf{u}(\mathbf{x}, t)$ where $\mathbf{x} \in \Omega \subset R^3$ and $t \in [0, T]$, then the **ensemble average** $\langle . \rangle$ is

$$\langle \mathbf{u}(\mathbf{x}, t) \rangle = \frac{1}{N} \sum_{j=0}^N \mathbf{u}^j(\mathbf{x}, t). \qquad (2.12)$$

Ensemble average is the average over flow realizations which is based on the probability density function approach (see Appendix (A.3)). In experiments we do not have an ensemble of velocity field realizations and therefore rely on Taylor's Frozen Field Hypothesis given in Equation (2.6) to convert temporal averages into spatial ones [30].

2.4 Correlations and Energy Spectrum

Let $u \in L^2(0, T)$, then the **autocorrelation function** of a stationary signal u for $\tau < T$ is defined as:

$$R_u(\tau) = \frac{\langle u(t), u(t + \tau) \rangle}{\|u(t)\|^2}. \tag{2.13}$$

Cauchy-Schwartz inequality shows that $\mid R_u \mid \leq 1$ showing that the function is normalized. The correlation function can be used to define an **integral time scale** T as:

$$T = \int_0^\infty r_u(\tau) \, d\tau \tag{2.14}$$

The time scale refers to the time over which the signal is correlated thereby serving as a type of memory of the signal.

For a sequence of statistically stationary functions $\{u_j(t)\} \subset L^2(0, T)$, **crosscorrelation** function is defined as

$$R_{jk}(\tau) = \langle u_j(t), u_k(t + \tau) \rangle. \tag{2.15}$$

Crosscorrelation is generalization of autocorrelation that represents how two different signals are correlated over time. The quantity $R_{jk}(0) = \langle u_j(t), u_k(t) \rangle$ is the Reynolds stress which is the fundamental quantity to model in CFD.

Consider the Fourier transform pair for Equation (2.15):

$$\Phi_{jk}(\omega) = \frac{1}{2\pi} \int_{-\infty}^\infty e^{-iw\tau} R_{jk}(\tau) \, d\tau \tag{2.16}$$

$$R_{jk}(\tau) = \int_{-\infty}^{\infty} e^{iw\tau} \Phi_{jk}(\omega)\, d\omega \tag{2.17}$$

If $R_{jk}(\tau)$ represents cross-correlation function of velocity fluctuations, then (2.16) for $\tau = 0$ and $j = k$ we obtain turbulence kinetic energy

$$k = \int_{0}^{\infty} \Phi_{jj}(\omega)\, d\omega \tag{2.18}$$

where k is formally defined in Appendix (A.4). It must be noted that here we have used the symmetry of both R_{jk} and Φ_{jk}.

Similarly, if cross-correlation of velocity fluctuations in space are considered, then we get the following Fourier Transform pair:

$$\Phi_{jk}(\mathbf{K}) = \iiint_{-\infty}^{\infty} e^{-i\mathbf{K}\cdot\mathbf{x}} R_{jk}(\mathbf{x})\, d^3\mathbf{x} \tag{2.19}$$

$$R_{jk}(\mathbf{x}) = \frac{1}{2\pi^3} \iiint_{-\infty}^{\infty} e^{i\mathbf{K}\cdot\mathbf{x}} \Phi_{jk}(\mathbf{K})\, d^3\mathbf{K} \tag{2.20}$$

where $\mathbf{K}$ is the wave number vector from the Fourier transform of the space vector $\mathbf{x} \in \Omega$.

Substituting $\mathbf{x} = 0$ and $j = k$, we have

$$R_{jj}(0) = \int \int \int_{-\infty}^{\infty} \Phi_{jj}(\mathbf{K})\, d\mathbf{K} \tag{2.21}$$

Let $K = \| \mathbf{K} \|$, then Equation (2.21) becomes :

$$R_{jj}(0) = \int_{-\infty}^{\infty} \oint \Phi_{jj}(\mathbf{K})\, dS(K) dK \tag{2.22}$$

18

where $S(K)$ is an element of the surface area defined in terms of K in wave number space.

Energy density function is defined by:

$$E(K) = \oint \frac{1}{2}\Phi_{jj}(\mathbf{K})dS(K) \tag{2.23}$$

which is also referred to as the Energy Spectrum.

Therefore, the turbulence kinetic energy $k = \frac{1}{2}\langle u_j(\mathbf{r}), u_j(\mathbf{r})\rangle$ can be obtained as:

$$k = \int_0^\infty E(K)\,dK. \tag{2.24}$$

where we have again used the symmetry of Φ_{jj}. The Equation (2.24) reveals that energy spectrum is the turbulence energy density per wave number.

2.5 Turbulence Scales

We conceive of turbulence as consisting of a continuous range of scales of eddying motion which are continuously interacting among themselves, transferring kinetic energy among different scales of motion. The largest scales contain most of the energy and it is thought that on average the transfer of energy proceeds down the scale to the smaller scales until the smallest viscous scales are reached where the kinetic energy dissipates to heat. In general turbulence looses energy to the mean flow. Thus unforced turbulence is a decaying phenomenon - it requires external agent (like stirring) to be sustained. Kolmogorove in 1941 proposed a scaling law called K41 theory which

is one of the few exact results in the study of turbulence [4].

Turbulence Reynold's Number based on the integral length scale and turbulence kinetic energy is given by,

$$Re_\ell = \frac{u'\ell}{\nu} \tag{2.25}$$

where $u' = \sqrt{\frac{\overline{u'^2}+\overline{v'^2}+\overline{w'^2}}{3}}$ is the turbulence kinetic energy per unit mass. ℓ is the integral length scale. Considering the rate of dissipation ϵ as a function of vorticity $\omega' = \nabla \times u'$, we have $\epsilon = \nu < \omega'.\omega' >$, so we can construct on dimensional grounds,

$$\ell = \frac{u'^3}{\epsilon}. \tag{2.26}$$

Thus we obtain the Kolmogorov's length scale η,

$$\eta = \left(\frac{\nu^3}{\epsilon}\right)^{\frac{1}{4}} \tag{2.27}$$

Kolmogorov's time scale is,

$$\tau = \left(\frac{\nu}{\epsilon}\right)^{\frac{1}{2}}. \tag{2.28}$$

The ratio of these quantities gives the Kolmogorov's velocity scale. The ratio between Kolmogorov's lengthscale and integral lengthscale is an important quantity in turbulence research. Here we will see why. From (2.27)

$$\eta \sim \left(\frac{\nu^3}{|u'|^3/\ell}\right)^{\frac{1}{4}},$$

using (2.5) we have

$$\frac{\eta}{\ell} \sim Re_\ell^{-\frac{3}{4}},$$

so that

$$\frac{\ell}{\eta} \sim Re_\ell^{\frac{3}{4}}. \tag{2.29}$$

So the ratio between Kolmogorov's microscale and integral lengthscale is related to the Reynold's number. If $E(K)$ is the energy spectrum with wave number K, dimensional analysis of (2.5) gives

$$E(K) = C_K \epsilon^{\frac{2}{3}} K^{-\frac{5}{3}} \tag{2.30}$$

the Kolmogorov Spectrum. C_K is Kolmogorov's constant which has been experimentally found to be around 1.5 [6] and $K^{-\frac{5}{3}}$ provides the essential inertial subrange where energy cascades from larger scales to the smaller scales and so on as shown in Figure 2.1.

2.6 Taylor's Hypothesis

Taylor introduced the hypothesis which asserts that turbulence at a point in time is approximately the same as due to convection of a spatial pattern [2]. This phenomenon is arguably true for any low intensity turbulent flow such as the ones being studied in this work. This is known as Taylor's frozen field hypothesis and it means that flow properties obtained over time are approximately equal to those obtained over space via the transformation

$$\frac{\partial}{\partial t} = u \frac{\partial}{\partial x}. \tag{2.31}$$
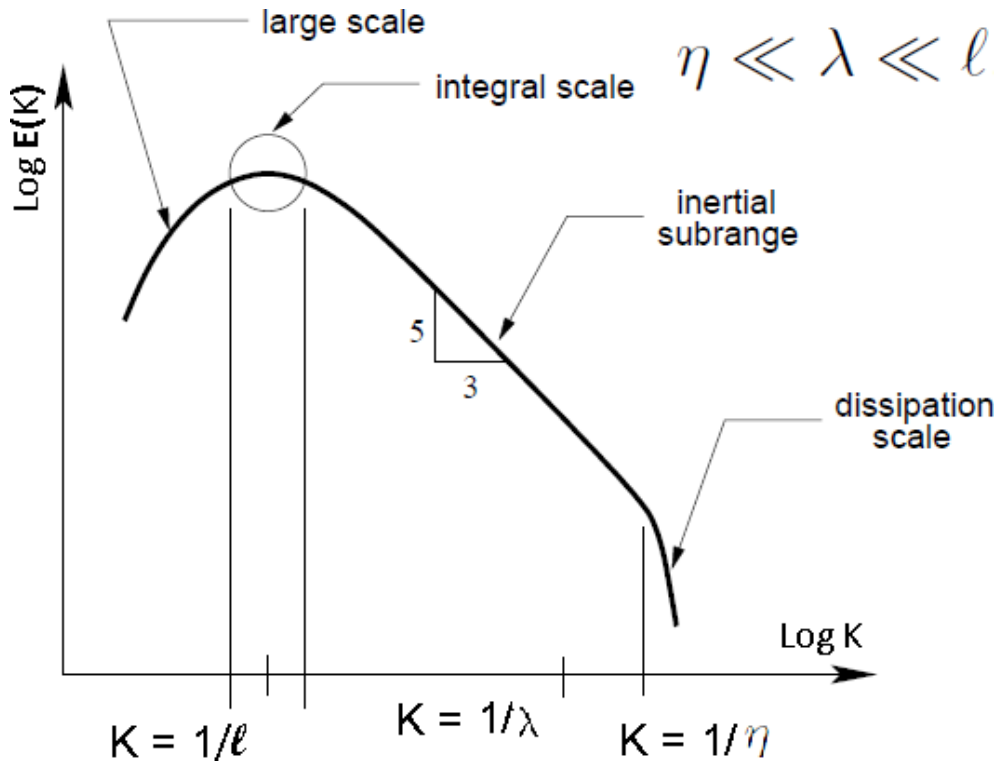
Figure 2.1: turbulence energy cascade [1]

This result is widely used in experiments to convert temporal data into spatial data and vice versa. There are some contentions as to whether the hypothesis is valid on a large scale but for the purpose of this study, it is valid and we see it being used on many occasions for such experiments in the literature.

CHAPTER 3

MULTI-SCALE GRIDS

In this chapter details of two-dimensional classical, fractal and the new three-dimensional sparse multiscale grids are given. The lengths, thicknesses and scales of the grids are defined as functions of physical characteristics such as blockage ratio, effective mesh size and distance between each co-frame. It needs to be mentioned here that all the grids studied in this work are passive grids meaning . Here a parametric study is performed by varying some parameters such as scaling factors, blockage ratios and grid thicknesses.

3.1 Classical Regular Grid

Classical grids have a flat square pattern (see Figure 3.1) that causes turbulence when a fluid flows through the square gaps. These grids have been extensively used as benchmark experimental method for the study of homogeneous isotropic turbulence. Corrison (1963) [5] showed that turbulence decays as a function of time (or space through Taylors hypothesis) when produced using classical grids. By performing ex-

periments on grids, he concluded that there is a power law decay of turbulence if thickness of the bars is very small as compared to the length of the bars. Regular grid (RG) can be completely described by its thickness d and number of bars N. An important scale of RG is the mesh number M defined as the distance between the centers of two consecutive squares of the grid. Blockage ratio σ is the ratio between areas of grid and channel cross section. If H^2 is the area of cross-section of a square channel of length H, then $M = H/N$. Then blockage ratio of RG is given by

$$\sigma_{RG} = 1 - (1 - \frac{d}{M})^2. \tag{3.1}$$

The perimeter P of a single square of RG is $4M(1 - \frac{d}{M})$ and there are N^2 squares in total so

$$P = 4M \left(\frac{H}{M}^2 \right) \left(1 - \frac{d}{M} \right) \tag{3.2}$$

Equating $\frac{d}{M}$ in Equation (3.1) and Equation (3.2) we get an expression for the mesh size of RG defined in terms of blockage ratio, channel width and perimeter as

$$M = \frac{4H^2}{P} \sqrt{1 - \sigma} \tag{3.3}$$

This defines a generalized mesh size for multi-scale grids. Experiments on RG [10] reveal that regular grid generated turbulence decays over the region $x/M \geq 20$. Mesh size is a scale length that characterizes turbulence as detailed in the later chapters.
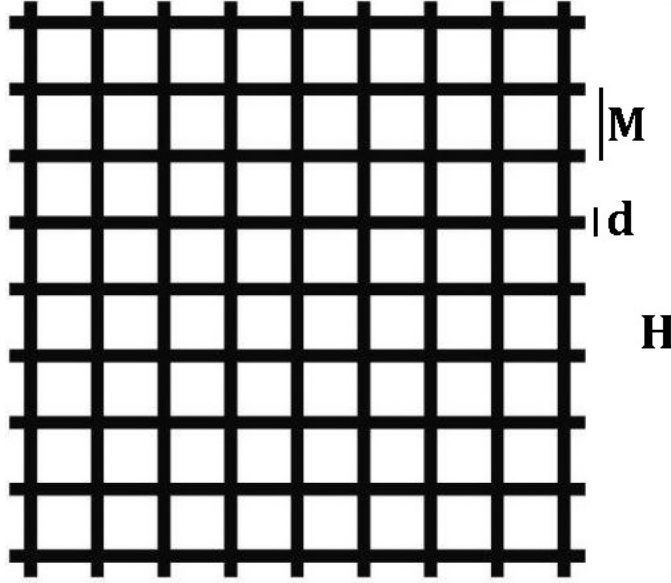
Figure 3.1: Classical regular grid

Decay of kinetic energy as function of time t is given by [10]

$$\langle \mathbf{u}^2 \rangle = t^{-n} \tag{3.4}$$

Using Taylors hypothesis, we have

$$\langle \mathbf{u}^2 \rangle = \left(\frac{x - x_0}{M}\right)^{-n}. \tag{3.5}$$

where x_0 is the position of the grid in the channel. It is believed that $1 \le n \le 1.4$ for homogeneous isotropic turbulence, however some studies suggest that the decay rate goes up to $n = 2$ [10] which is quite far from the established norm. The same studies have suggested that this decay is affected by initial conditions but for fully developed turbulent flow, initial conditions should not be this significant according to [2]. Hence this is another area in regular grid generated turbulence research which

requires further investigation. Any study showing marked difference from the classical

grid generated turbulence case is of interest in the scientific circles.

3.2 Fractal Grid

Fractal square grid (2DF) is a multiscale grid with repeating self-similar square fractal

pattern as shown in Figure 3.2. 2DF display a higher peak turbulence intensity on

average as compared to RG [13] with the same blockage ratio. This is attributed to

the multi-scale nature of the fractal grids which resembels the multiscale nature of

turbulence. It is important to define 2DF in terms of blockage ratio and mesh size

because they affect physical properties of the flow. Let l_j and d_j denote, respectively,

the length and thickness of the jth iteration ($0 \leq j \leq N - 1$) of fractal in 2DF, then

2DF can be described by the largest length l_0 and highest thickness d_0 of the initial

pattern and the ratio of lengths R_l and thicknesses R_d defined as,

$$R_l^j = \frac{l_j}{l_0},$$ (3.6)

where R_l is the ratio of lengths of jth to the maximum length l_0 of the fractal and

$$R_d^j = \frac{d_j}{d_0}.$$ (3.7)

R_d is the ratio of thickness of jth to the maximum thickness d_0 of the fractal. Let

a^j be the number of fractal patterns on the jth fractal, then in case of fractal square

grids, $a = 4$. For there to be no crossing over of the fractals $R_l \leq 1/2$ and $R_d << 1$.
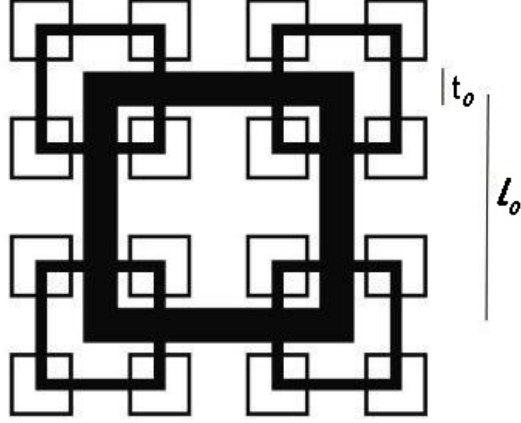
Figure 3.2: Flat fractal square grid

The surface area of 2DF is then given by

$$A := \sum_{j=0}^{N-1} a^{j+1} l_j d_j = a \sum_{j=0}^{N-1} l_0 d_0 (a R_l R_d)^j. \tag{3.8}$$

This means that the blockage ratio of 2DF is

$$\sigma_{2DF} := \frac{a l_0 d_0}{H^2} \frac{1 - (a R_l R_d)^N}{1 - a R_l R_d}. \tag{3.9}$$

Note that in the above formula which is generally used in most experiments, the overlapping of bars is not considered, hence the actual blockage should be slightly less than the value given in Equation (3.9). The error can be removed by deleting all the overlaps, then the corrected area of 2DF is

$$A_{2DF} := \sum_{j=0}^{N-1} a^j \left[a l_j d_j - \frac{a}{2} d_j d_{j-1} \right]. \tag{3.10}$$

Then corrected blockage ratio of fractal grid with patterns a number of iteration N length ratio R_l, thickness ratio R_d cross-section length and width $2l_0$ and largest length

and thickness l_0 and d_0 is given by,

$$\sigma_{2DF} := \frac{ad_0}{4l_0^2}\left[l_0\frac{1-(aR_lR_d)^N}{1-aR_lR_d} - \frac{d_0}{2R_d}\frac{1-(aR_d^2)^N}{1-aR_d^2}\right].\tag{3.11}$$

Fractal dimension D is the scaling exponent of fractals and is defined as,

$$D = \frac{log(a)}{log(1/R_l)}.\tag{3.12}$$

This shows that, for a fractal square grid with scaling factor $1/R_l = 2$, the fractal dimension $D = 2$.

RG is a special case of 2DF with $a = R_l = R_d = 1$, $l_0 = H$ and $d_0 = d$.

3.3   Sparse Multiscale Grids

A recent innovation in multi-scale grid generated turbulence is the three dimensional sparse grid (3DS) [27]. The 3DS (Figure 3.3) is generalization of 2DF as each multi-scale iteration is separated into its own plane in a co-planar arrangement. This results in an overall reduction in the blockage ratio of 3DS as compared to 2DF of the same projected surface area. Moreover, a new parameter is introduced in 3DS as compared to 2DF in the form of separation distance between consecutive co-frames.

The surface area of jth iteration of 3DS is given by

$$A_j = a^{j+1}l_jd_j = al_0d_0(aR_lR_d)^j.\tag{3.13}$$
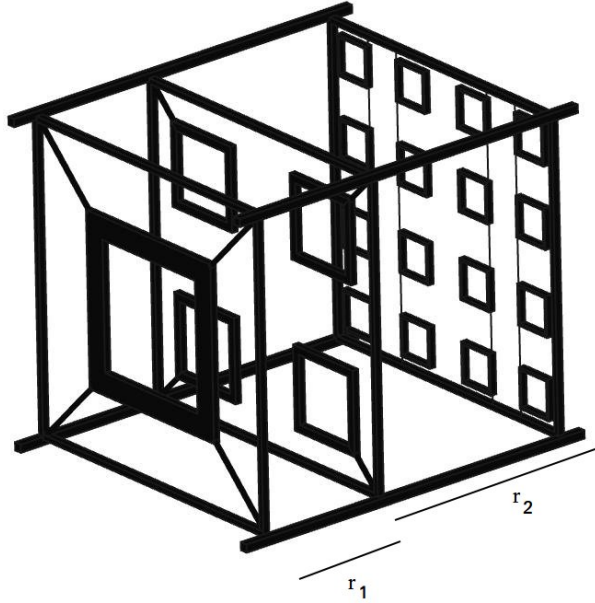
Figure 3.3: 3D sparse multiscale grid

So that the maximum blockage ratio of 3DS is

$$\sigma_{3DS}^{Max} = Max_{j=0}^{N-1}\{\frac{al_0d_0(aR_lR_d)^j}{H^2}\}.\tag{3.14}$$

Now let us compare a special case of 3DS and 2DF of the same total surface areas. Although the length and thickness ratio of multi-scale grids need not be equal but for the sake of simplicity, let $R_l = R_d = r$ for $r < 1$ and number of grid iterations $N = 3$. Suppose further that $l_0 = sH$ for $s < 1$ and $d_0 = w$. Then the maximum blockage ratio of three fractal iteration square grid is

$$\sigma_{2DF} = (sw - w^2)(4 + 16r^2 + 64r^4) - w^2(8r + 32r^3).\tag{3.15}$$

Let σ_1, σ_2 and σ_3 be the blockage ratios of the first, second and third fractal

iterations of 3DS, then

$$\sigma_1 = 4(qw - w^2), \tag{3.16}$$

$$\sigma_2 = 4r^2\sigma_1, \tag{3.17}$$

$$\sigma_3 = 16r^4\sigma_1. \tag{3.18}$$

So that $\sigma_{3DS}^{Max} = Max\{\sigma_1, \sigma_2, \sigma_3\}$.

Clearly $\sigma_{3DS}^{Max} \leq \sigma_{2DF}$.

Figures 3.4 show the variation in blockages σ as function of r with $w = 0.05$ for cases $s = 0.5$ and $s = 0.7$. It can be seen that the optimal value of length and thickness ration is $r = 0.5$ at which point we can see that σ_j are all equal and nearly one-third of σ_{2DF}, because $\sigma_1 = \sigma_2 = \sigma_3 = \sigma$ and $\sigma_{2DF} = \sigma_1 + \sigma_2 + \sigma_3 = 3\sigma$ Relative blockage
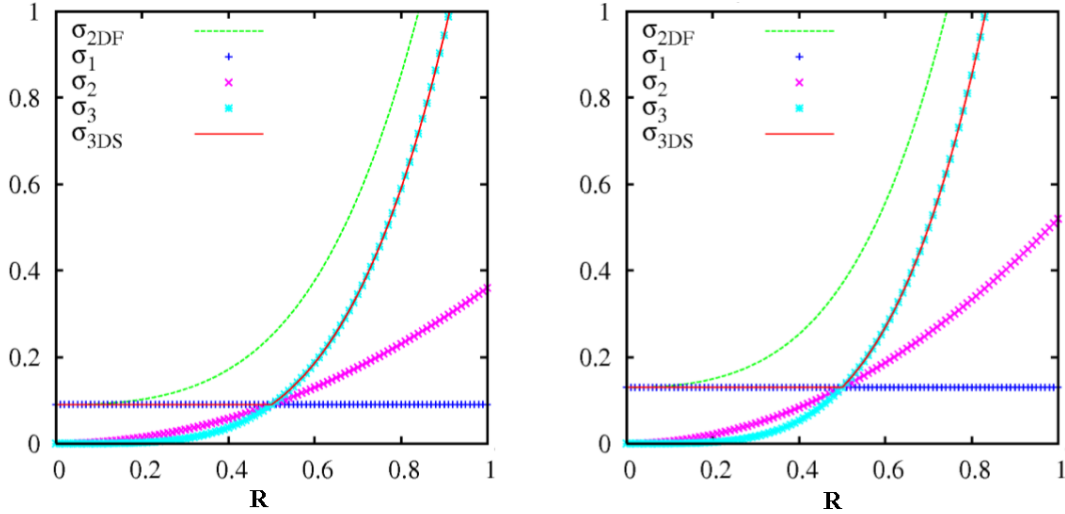
Figure 3.4: Blockage ratio σ vs scaling ratio r of 3DS and 2DF grids with $w = 0.05$ and $a = 0.5$ (left) and $a = 0.7$ (right).

ratio from 2DF to 3DS is defined as

$$R(\sigma, s, r) = \frac{\sigma_{3DS}^{Max}}{\sigma_{2DF}}. \tag{3.19}$$

For each separate iteration of multi-scale grids, scale by scale relative blockage ratio is defined as

$$R_1(\sigma, s, r) = \frac{\sigma_1}{\sigma_{2DF}} \tag{3.20}$$

$$R_2(\sigma, s, r) = \frac{\sigma_2}{\sigma_{2DF}} \tag{3.21}$$

$$R_3(\sigma, s, r) = \frac{\sigma_3}{\sigma_{2DF}}. \tag{3.22}$$

Investigation of different relative blockages of multi-scale grids is displayed in Figure 3.5. Relative blockage R as a function of scaling factor r are shown in Figure 3.5 for $w = 0.05$ with $s = 0.5$ and $s = 0.7$ respectively. A minimum of R_σ can be observed at $r = 0.5$. Moreover the solidity of 3DS is much lower as compared to 2DF, for a three generation multi-scale grid, the solidity of 3DS is one third the solidity of 2DF and this is one of the main features of using 3DS for turbulence investigation. We have seen so far that the optimal reduction of relative solidity occurs when $r = 0.5$. The mass flux rate M through this system of a given pressure drop can be approximated as,

$$M = (1 - \sigma)F(Re; \rho, U, \mu, l) \tag{3.23}$$

where F is some function for example, propotional to the pressure drop $F \propto \nabla p$. Usually F is a function of the pressure p, μ the dynamic viscosity, ρ the density, U the
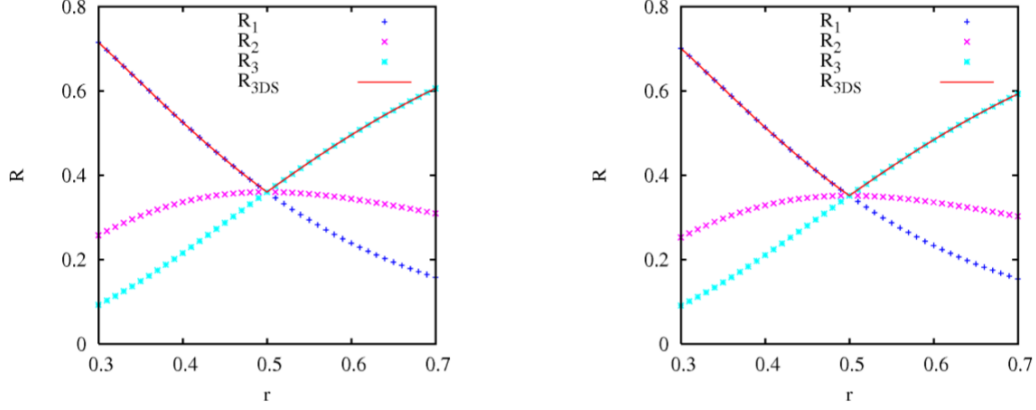
Figure 3.5: Relative solidity R vs scaling ratio r of 3DS and 2DF grids with $w = 0.05$ and $s = 0.5$ (left) and $s = 0.7$ (right).

mean velocity and l the characteristic length scale with Reynolds number Re defined in these terms. The relative rate of increase in mass flow from 2DF to 3DS can be defined as

$$f_\sigma(w, s, r) = \frac{M_{3DS}}{M_{2DF}} \cong \frac{1 - \sigma_{3DS}}{1 - \sigma_{2DF}}. \tag{3.24}$$

Similarly for each separate iteration, mass flux rate is

$$f_1(w, s, r) = \frac{1 - \sigma_1}{1 - \sigma_{2DF}} \tag{3.25}$$

$$f_2(w, s, r) = \frac{1 - \sigma_2}{1 - \sigma_{2DF}} \tag{3.26}$$

$$f_2(w, s, r) = \frac{1 - \sigma_3}{1 - \sigma_{2DF}}. \tag{3.27}$$

So that

$$f_\sigma \cong f_1 + f_2 + f_3. \tag{3.28}$$

In Figure 3.6, mass flux rates for $w = 0.05$ with $s = 0.5$ and $s = 0.7$ are plotted against r. For $s = 0.5$ and $w = 0.05$, 3DS shows a 21% increase in mass flux as

32
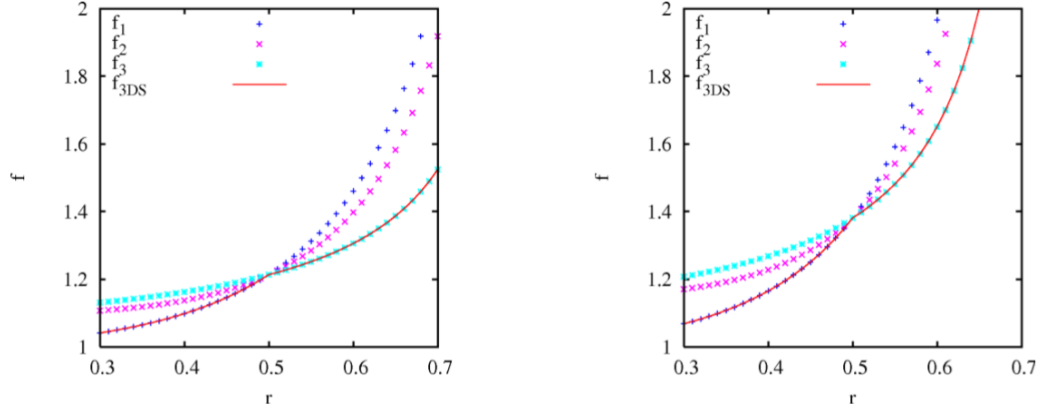
Figure 3.6: Mass flow rate f vs scaling ratio r of 3DS and 2DF grids with $w = 0.05$ and $s = 0.5$ (left) and $s = 0.7$ (right).

compared to 2DF whereas for $s = 0.7$ there is a 40% increment. Although for large values of r, we see a rapid increase in the mass flux rate, we know that as $1 - \sigma \to 0$ and mass flux goes to zero.

From a theoretical point of view, 3DS grids display lower maximum blockage ratio and higher mass flux rate than 2DF grids. Another important conclusion is that the optimum scaling value for length and thickness is $1/2$. Now the question is how these differences translate in the study of grid generated turbulence using numerical simulations of actual turbulent flows.

<center>

CHAPTER 4

NUMERICAL SETUP

</center>

In this chapter, continuity and momentum equations are discretized on a three dimensional cubic structured mesh using finite volume method. Numerical technique is discussed in detail and the simulation algorithm is described.

4.1 Discretization of NS Equations

Consider a three dimensional domain $\Omega \subset R^3$. The problem can be described using the following system.

$$
\begin{cases}
\frac{\partial \mathbf{u}}{\partial t} + \nabla \cdot \mathbf{u}\mathbf{u} = -\nabla P + \nu \Delta \mathbf{u}, & \text{in } \Omega \times (0, T) \\[2mm]
\nabla \cdot \mathbf{u}(\mathbf{x}, t) = 0, & \text{in } \Omega \times (0, T) \\[2mm]
\mathbf{u}(\mathbf{x} - \mathbf{h}, t) = \mathbf{u}(\mathbf{x} + \mathbf{h}, t), & \text{on } \partial\Omega \times (0, T) \\[2mm]
\mathbf{u}(\mathbf{x}, 0) = u_0(\mathbf{x}), & \text{in } \Omega
\end{cases}
\tag{4.1}
$$

The system of equations(4.1) describes the momentum and mass conservation equations with periodic boundary conditions in lateral direction and an initial inflow field

<center>34</center>

in the streamwise direction describing Navier-Stokes equations for a incompressible Newtonian fluid with constant dynamic viscosity ν, dynamic pressure $P = p/\rho$ and velocity vector $\mathbf{u}$. The exact solution for the above problem in three dimensional space over all times is called the last unsolved problem of classical physics. The numerical solution to the above problem of turbulence will be solved using finite volume approach.

Consider a collocated mesh arrangement where all flow variables are recorded at the cell centers. In tensorial notation, the jth momentum equation $2 \leq j, k \leq 3$ can be written as

$$\frac{\partial u_j}{\partial t} + \frac{\partial u_j u_k}{\partial x_k} = -\frac{\partial P}{\partial x_j} + \nu \frac{\partial^2 u_j}{\partial x_k \partial x_k} + f_j \tag{4.2}$$

In the above equation the first term is called **unsteady term** as it represents rate of change over time, the second term is the **convection term** and on the right hand side, we have **pressure gradient**, **diffusion** and **body forcing** terms. Tensoral notation is used here. Integrating the above equation over time interval $[t, t + \triangle t]$ and control volume V we get

$$\int_t^{t+\triangle t} \iiint_V \left[\frac{\partial u_j}{\partial t} + \frac{\partial u_j u_k}{\partial x_k} \right] dV dt = \int_t^{t+\triangle t} \iiint_V \left[-\frac{\partial P}{\partial x_j} + \nu \frac{\partial^2 u_j}{\partial x_k \partial x_k} + f_j \right] dV dt \tag{4.3}$$

Using divergence theorem with outward pointing unit vector n on the surface S of control volume V

$$\iiint_V \nabla \cdot \overline{G} dV = \iint_S \overline{G} \cdot \mathbf{n} dS \tag{4.4}$$

35

on convection, pressure and diffusion terms and using backward Euler time stepping technique we have

$$\frac{u_j - u_j^{(0)}}{\Delta t}V + \iint_A u_j u_k n_j dA = -\iint_A P n_j dA + \iint_A \nu \frac{\partial u_j}{\partial x_k} n_k dA + f_j V \qquad (4.5)$$

where $u_j^{(0)}$ is the previous time step and backward Euler is a first order implicit technique where next time step is solved using the previous one. Assuming that the mesh is cuboid and there is no body force, the surface integrals can be written as summation over each face, so that

$$\frac{u_j - u_j^{(0)}}{\Delta t}V + \sum_{k=nb} (u_j u_k n_k A) = -\sum_{k=nb} (P n_j A) + \sum_{k=nb} \left(\nu \frac{\partial u_j}{\partial x_k} n_k A\right) \qquad (4.6)$$

Here the sum is taken over each neighboring face to the jth cell in the domain. For a two dimensional domain, the discretised x-momentum equation with cell center j and velocity vector (u, v) is given by

$$\begin{aligned}
&\frac{u_j - u_j^{(0)}}{\Delta t} - \left(\frac{u_j u}{\Delta x}\right)_w + \left(\frac{u_j u}{\Delta x}\right)_e - \left(\frac{u_j v}{\Delta y}\right)_s + \left(\frac{u_j v}{\Delta y}\right)_n \\
&= -\left(\frac{P n_j}{\Delta x}\right)_w - \left(\frac{P n_j}{\Delta x}\right)_e - \left(\frac{P n_j}{\Delta y}\right)_s - \left(\frac{P n_j}{\Delta y}\right)_n \\
&- \left(\nu \frac{\partial u_j}{\partial x} \frac{1}{\Delta x}\right)_w + \left(\nu \frac{\partial u_j}{\partial x} \frac{1}{\Delta x}\right)_e - \left(\nu \frac{\partial u_j}{\partial y} \frac{1}{\Delta y}\right)_s + \left(\nu \frac{\partial u_j}{\partial y} \frac{1}{\Delta y}\right)_n
\end{aligned} \qquad (4.7)$$

where w,e,n,s are the west east north and south neighbor grid points of the two dimensional system of equations and $n_1 = (1,0)$, $n_2 = (0,1)$, $u_1 = u$ and $u_2 = v$. Partial derivatives can be calculated using some interpolation techniques. In practice, finite volume method is the closest to an exact solution at the grid points of the

domain. However, interpolations, truncation and approximations introduce errors.

Continuity equation for Newtonian, incompressible fluid is given by

$$\nabla \cdot \mathbf{u} = 0 \tag{4.8}$$

Using divergence theorem (4.4) implies

$$\iiint_V \nabla \cdot \mathbf{u} \, dV = \iint_S \mathbf{u} \cdot \mathbf{n} \, dS = \sum_{k=nb} u_k n_k A = 0. \tag{4.9}$$

This means that the mass flux is conserved since the amount of fluid entering and leaving through the cell faces is balanced out.

4.2   Numerical Method

Pressure Implicit Split Operator Algorithm (PISO) was proposed in 1986 by Issa and it requires lesser computing effort than many similar algorithms to solve Navier-Stokes equations.

- The equation (4.6) is solved using the initial velocity $\mathbf{u}^{(0)}$, pressure p and boundary conditions to get an intermediate velocity field, the pressure thus obtained is not correct. As mentioned before we have used finite volume discretisation, the non-linearity is removed by using $u_k^\gamma \frac{\partial u_j^\gamma}{\partial x_k} = u_k^{\gamma-1} \frac{\partial u_j^\gamma}{\partial x_k}$ where $\gamma - 1$ represents a fractional time step. Gauss linear scheme is used in spacial discretisation and the resulting system of linear equations is solved using biconjugate gradient method. The velocity thus obtained is $\mathbf{u}^*$. The pressure p^* may or may not be

37

correct.

- Since the velocity and pressure fields on the previous time step are known, in matrix form, the momentum equation can be written as,

$$a_P^{\mathbf{u}}\mathbf{u}_P = \mathbf{H}(\mathbf{u}) - \nabla P \qquad (4.10)$$

where $\mathbf{H}(\mathbf{u}) = \sum a_N^{\mathbf{u}}\mathbf{u}_N + \mathbf{r}$. Applying gradient and using divergence free condition on equation (4.10) we have the pressure equation,

$$\nabla \cdot \left[(a_P^{\mathbf{u}})^{-1}\nabla p\right] = \nabla \cdot \left[(a_P^{\mathbf{u}})^{-1}\mathbf{H}(\mathbf{u})\right]. \qquad (4.11)$$

The term on the right hand side represents the mass flux on each cell face and the equation (4.11) is Poisson equation for pressure. By calculating the flux on right hand side of the equation (4.11) we can solve the resulting poisson equation.

- Once the the equation (4.11) is solved, we get pressure correction p^{**} to the NS system. The pressure correction can now be used to correct the mass flux.

- Define $p' = p^{**} - p^*$ and $\mathbf{u}' = \mathbf{u}^{**} - \mathbf{u}^*$ as the correction factors for pressure and velocity. Now velocity is corrected by using p^{**} as the initial pressure in (4.6) to calculate the corrected $\mathbf{u}^{**}$. This is called the first corrector step. In PISO, second corrector step is recommended [31]. The procedure is repeated until prescribed tolerance is achieved.

- The same procedure is repeated for each time step.

The Pressure Implicit Split Operator method is favored over others because of its unconditional stability over collocated mesh [32] as we have used in our work. It also permits a larger time step and thus reduces CPU time.

4.3 Direct Numerical Simulation

Direct Numerical Simulation (DNS) is the numerical solution of Navier-Stokes equations to study turbulence without modeling. DNS is a benchmark investigation of fluid flow where all scales of turbulence are resolved up to machine accuracy. Due to the very high mesh resolution requirement of DNS, it is not yet feasible to adopt this method for industrial purposes as for many coming years, even at the current rate of rise in computation powers, the computational cost of DNS will remain an unresolved issue [33].

Kolmogorov microscale η defined in equation (2.27) is the smallest scale that has to be resolved so that for a mesh size h, $h < \eta$. Moreover the resolution $N \geq \ell/h$ for the largest scales to remain within the domain, where ℓ is integral length scale as defined in (2.26). Using (2.26) and (2.27) we have

$$\frac{\ell}{\eta} \sim \left(\frac{u'\ell}{\nu}\right)^{3/4} \tag{4.12}$$

So that

$$\frac{\ell}{\eta} \sim Re^{3/4} \tag{4.13}$$

This implies that for a three dimensional cubic domain $N^3 \leq Re^{9/4}$. If N_t is the number of time steps and $N_t \leq N$ because of the courant condition $\frac{u\Delta t}{\Delta x} < 1$, then $N^3 N_t \leq Re^3$. The total number of operations to perform on a cubic domain with mesh points N and time steps N_t grows like Re^3. Computation power is measured in flops which is the number of floating point operations per second. Therefore on a large domain such as atmosphere or hurricane etc., where Reynolds number is very high, it is impossible to use DNS whereas for investigation of grid generated turbulence, it is the ideal tool.

4.4   Simulation Setup

Flow in a conduit under the influence of multiscale grids is investigated in a cuboid domain

$$\Omega = \{(x, y, z) \subset \Re^3 | 0 \leq x \leq T, -l_0 \leq y, z \leq l_0\}. \tag{4.14}$$

The numerical setup as discussed in the previous section has been applied in the simulation setup.

General purpose open source CFD packages are robust and effective for numerical simulation of fluid flow but the challenge that they are so far unable to meet is that they do not support a very high resolution mesh which in our case is essential. We have used a second order finite-volume discretisation with Pressure Implicit Split Operator (PISO) Algorithm to simulate incompressible fluid flow. The advantage of

PISO algorithm is its unconditional stability on collocated grids [31] and larger time step admissibility. Such simulations produce tera-bites of data as output which is impossible to visualize on a normal computer or laptop. Parallel Python script has to be used to visualize simulation outputs through Paraview and parallellized Matlab codes for some plotting. The idea is to write a robust algorithm for incompressible flow simulation on burst-buffer for Domain Discretization, Numerical Simulation and Post-Processing all-in-one. Details of the simulation are as follows:

Parameters	Case 1			Case 2		
	RG1	2DF1	3DS1	RG2	2DF2	3DS2
$\sigma(\%)$	32	32	15	32	32	15
l_x/d_{min}	460.8	460.8	460.8	576	576	576
l_0/d_{min}	115.2	57.6	57.6	115.2	57.6	57.6
l_1/d_{min}	-	28.8	28.8	-	28.8	28.8
l_2/d_{min}	-	14.4	14.4	-	14.4	14.4
d_0/d_{min}	2.6	8.5	8.5	2.6	8.5	8.5
d_1/d_{min}	-	2.915	2.915	-	2.915	2.915
d_2/d_{min}	-	1	1	-	1	1
r_1/d_{min}	-	-	17	-	-	17
r_2/d_{min}	-	-	8.5	-	-	8.5

Table 4.1: Details of grid designs for two sets of simulations. All lengths are normalized by the smallest bar thickness d_{min} of 2DF1. These grids vary according to parameters such as channel length $d_{min}j$, blockage ratio σ, scaling factor $R_l = 0.5$ and $R_d = 0.343$ as defined in equation (3.6)

- The turbulence generating grid G is placed slightly downstream of conduit to avoid spurious initial flow field effects. Let $x_0 > 0$ be the position of the grid inside the domain Ω defined in (4.14). Mathematically, the grid $G \subset \Omega$ and for a cell $b \in \Omega$ with $b \cap G \neq \emptyset$, then $G = \{b \in \Omega | u_b = 0\}$ i.e. a set of cells in the domain where no-slip boundary condition is imposed so that the grid acts as a blockage in the path of the flow.

- Table 4.1 refers to a set of simulations that have been carried out to investigate grid generated turbulence. The three set of grids are RG, 2DF and 3DS and there are different cases based on various parameters. The cases are based on the blockage ratio σ of the various grids. Comparisons made for the same projected blockage. In Case 1, the channel length $l_x = 460.8d_{min}$ and for all other cases $T = 576d_{min}$. The channel width $2l_0 = 115.2$ for all cases.

- The doamin is discretized using finite volume method with $\Delta x = \Delta y = \Delta z = 0.2d_{min}$. The total number of spatial discretization cells in Case 1 is $2304 \times 576 \times 576$ and for all other cases, the number of cells is $2880 \times 576 \times 576$. Table 4.2 describes a set of 3DS grids exclusively with grids differing either in their blockage ratios or the order in which the co-frames are arranged. Since the number of parametric variations to consider is limitless, the grid separations have been kept constant in this work at $r_1 = 17 \ d_{min}$ and $r_2 = 8.5 \ d_{min}$.

- The values of r_2 and r_2 where chosen in a way that the wakes generated by the next co-frame interact with the solid surface of the next co-frame and thereby disrupt the velocity field even further than 2DF grids. A parametric study on was performed to see what optimum position of r_1 and r_2 should be taken, however the values are not optimum.

- In order to perform DNS on such a fine mesh, the domain is decomposed into 2048 classes where each of these classes is assigned to a CPU core. So in Case 1, 2048 CPU cores are used on HPC facility and in all other cases 2360 CPU cores are used to perform parallel simulations.

- Probes and pencils are placed in places of interest to record physical characteristics over time. The probes record various flow characteristics such as velocity, gradients, pressure, vorticity, Reynolds stress tensors and passive scalars etc. A pencil is a sequence of probes placed in the domain.

Parameters	Case 3 (a)		Case 3 (b)	
	3DS3	3DS4	3DS5	3DS6
$\sigma(\%)$	25	32	32	32
l_x/d_{min}	576	576	576	576
l_0/d_{min}	57.6	57.6	57.6	57.6
l_1/d_{min}	28.8	28.8	28.8	28.8
l_2/d_{min}	14.4	14.4	14.4	14.4
d_0/d_{min}	14.4	18.4	18.4	18.4
d_1/d_{min}	2.915	2.915	2.915	2.915
d_2/d_{min}	1	1	1	1
order (by Z_j)	Z_0, Z_1, Z_2	Z_0, Z_1, Z_2	Z_1, Z_0, Z_2	Z_2, Z_1, Z_0
r_1/d_{min}	17	17	17	17
r_2/d_{min}	8.5	8.5	8.5	8.5

Table 4.2: Case 3(a) of comparison of grids varying according to the blockage ratio. Case 3(b) of comparison of 3DS grids having equal blockage ratios but different arrangement of the sparse iterations Z_j. Z_j are defined in the figures 4.1c.

- Passive scalars transport is studied by solving the convection diffusion equation

$$\frac{\partial c}{\partial t} + \nabla \cdot (\mathbf{u}c) = \nabla \cdot (D\nabla c) \tag{4.15}$$

where c is the scalar being transported, $\mathbf{u}$ is the flow velocity and D is the diffusivity of the scalar. Scalar transport is analogous to a dye or ink in a fluid to see how it mixes.

- All quantities are normalized by the smallest bar thickness $d_2 = d_{min}$ of the fractal grid (2DF) and a time scale based on d_{min} is defined by $\frac{d_{min}}{U_\infty}$ where U_∞
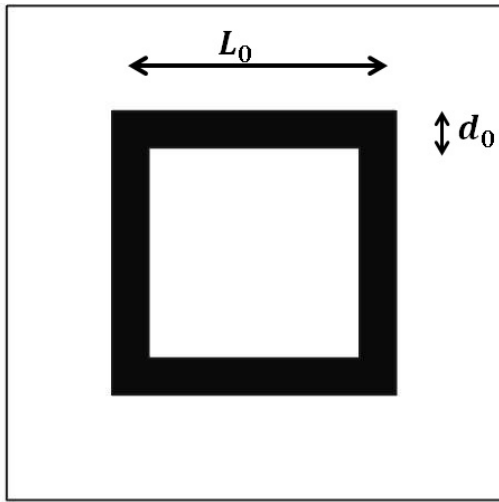
(a) Z_0
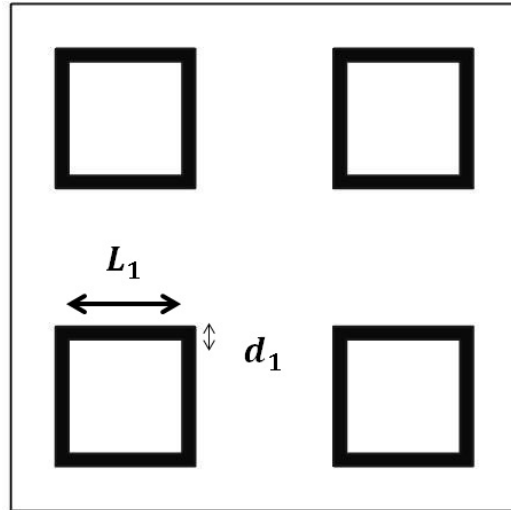
(b) Z_1
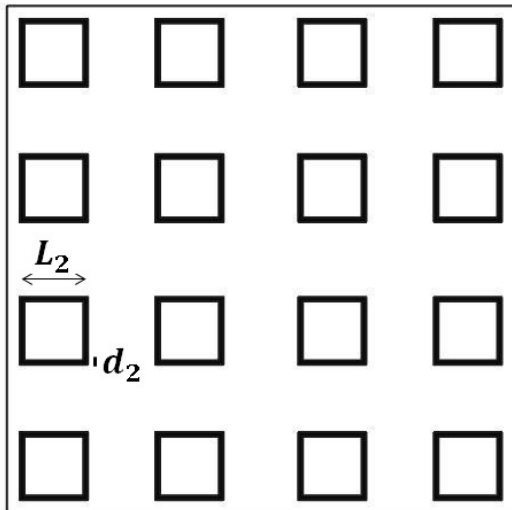
(c) Z_2

Figure 4.1: Three different fractal iterations of the sparse multiscale grid. Each iteration is separated by a distance r_j and held in its own frame in the yz-plane at different locations along the x-axis.

is the inflow velocity.

- Reynolds number $Re_{d_{min}} = \frac{d_{min}U_\infty}{\nu} = 300$ where ν is the dynamic viscosity of the fluid and normalized inflow velocity $U_\infty = 1$. All the parameters were chosen to match the DNS of LV2012 in order to facilitate the validation and the comparison with our own DNS.

- Total simulation time was based on experience and literature [13] which suggests that around fifty thousand times steps are required to get a fully developed turbulent flow.

- Time averaging is done over the time when the flow is fully developed. The time from $350d_{min}/U_\infty$ to $650d_{min}/U_\infty$ is a good sample set for statistical analysis of turbulence [24]. We took averages over different time intervals starting from 200 d_{min}/U_∞ and found that the variation in results are no more than 5%.

- Channel is long enough to establish turbulence developed all the way downstream and wide enough to allow generation of large scales from the mean flow.

The grids used in this study are chosen from literature review. These studies suggest that the channel length should be atleast 10 times the width for homogeneity and isotropy, but that would be computationally very expensive. Also $D_f = 2$ is the optimum fractal dimension and physically accurate blockage ratio of sparse grid is the maximum of blockage of the co-frames rather than their sum. Moreover, to resolve all scales of turbulence, the simulation resolution should be five times smaller than smallest bar thickness. This implies $\Delta x = \Delta y = \Delta z \leq d_{min}/5$. Time step

$\Delta t = 0.015 d_{min}/U_\infty$ and the mesh size $\Delta x = 0.2 d_{min}$. The flow is simulated for total time of $800 d_{min}/U_\infty$ but due to computation costs and storage limitations only 30 full field snapshots are recorded randomly out of the total 55 thousand flow realizations. Inflow velocity is uniform U_∞ with inlet outlet boundary conditions along x-axis and periodic boundary conditions along y- and z-axis. Probes and pencils were also placed at important locations in the channel to record flow characteristics over the entire simulation time resulting in a few tera bites of simulation output requiring heavy computation resources for post processing images, graphs and other calculations. All simulations were carried out on the Falcon High Performance Computing Platform at King Abdullah University of Science and Technology KAUST Shaheen II HPC.

CHAPTER 5

RESULTS AND DISCUSSION

5.1 Comparison of RG1, 2DF1 and 3DS1

In this section three grids, the classical regular grid (RG1) Fig.3.1, the flat fractal square grid (2DF) Fig.3.2 and the 3D sparse grid (3DS) Fig.3.3 are investigated in a channel flow configuration. The purpose is to firstly, validate the results of our direct numerical simulation against those of Laizet and Vassillicos [24] and secondly, to compare those results with the new 3DS grids. As we will see, there is a large number of co-frame arrangements and co-frame solidities of the same maximum solidity and it will not be possible to cover all the cases in this piece of work, so we have selected a few cases to be investigated as an initial case study of the 3DS grids. This section describes simulation of RG, 2DF and 3DS grids having equal effective mesh sizes and compares the results with [24]. The channel is a conduit of dimensions $L_x \times L_y \times L_z$, where $L_x/d_{min} = 460.8$ and $L_y/d_{min} = L_z/d_{min} = 115.2$. The grid is placed at $x_0/d_{min} = 10$ inside the channel to avoid any spurious effects from the initial flow field. The streamwise thickness of the three grids RG1, 2DF1 and 3DS1 is $2.4d_{min}$.

The inflow velocity is a uniform $U_\infty = 1$ and initial velocity field is set at $(U_\infty, 0, 0)$ at the inlet of the channel, which yields a Reynolds number based on d_{min} to be,

$$Re = \frac{U_\infty d_{min}}{\nu} = 300. \tag{5.1}$$

Inlet-outlet boundary condition is set on the outlet boundary to avoid any reverse flow that might cause the system to violate mass conservation. The inlet-outlet boundary condition is a type of mixed boundary condition which has a switch whereby at the outlet we have a Drichlet type boundary condition if the streamwise velocity is directed into the channel but it switches to Neumann type boundary condition if the streamwise velocity is directed out of the channel. Periodic boundary conditions are applied at the walls in the other two directions. Blockage ratio $\sigma_{RG1} = \sigma_{2DF1} = 32\%$ where as $\sigma_{3DS1} = 15\%$. The parameters of 2DF1 are $\{l_j, d_j\}$. In 3DS1 grids, there are additional parameters $r_1 = x_1 - x_0$ and $r_2 = x_2 - x_1$ which are the inter-frame distances between consecutive co-frames, making its parameter space larger than that of RG1 and 2DF1. x_j is the plane of jth frame in 3DS1 ($j = 0, 1, 2$) in the channel and the non-dimensionalized distances between the frames $r_1/d_{min} = 17$ and $r_2/d_{min} = 8.5$. Details of the grids are given in Table 4.1 and Fig.5.1 describes the 3D sparse grid in a channel flow configuration.

Figures 5.2-5.13 show comparisons of turbulence characteristics obtained from RG1, 2DF1, and 3DS1 grids from DNS. The RG1 and 2DF1 plots match the results of Laziet & Vassilicos [24], which validates the current DNS for these calculations because our parameter values have been based upon the simulations that they ran.
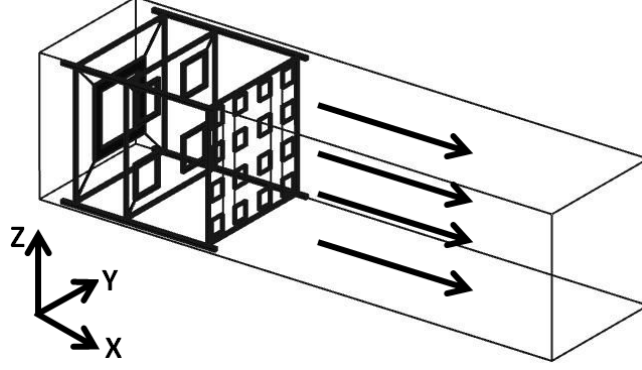
Figure 5.1: 3DS grid in a conduit where 3D sparse multiscale grid having three frames is placed at the inlet of the conduit and the arrows represent the streamwise direction in which the fluid is flowing.

Results from DNS of Laizet et.al. [24] were validated against experiments on fractal grid turbulence given in Hurst et. al. [10] which adds to the authenticity of the DNS results of Laizet et. al (2012) and therefore, also our work.

Figures 5.2a,5.2b and 5.2c show the plots of the streamwise turbulence intensity $\langle (u'(x))^2 \rangle^{1/2}/U_\infty$ where the mean is taken over time, and the streamwise mean flow, $U(x)/U_\infty$, along the centerline of RG1, 2DF1 and 3DS1 respectively. The values of mean flows in the 2DF1 and 3DS1 are close for most of the channel length, and both are significantly higher than in the RG1 grid. The turbulence intensity peaks at $x/d_{min} \cong 10$, dies slowly downstream of the grid in RG1 and dies down close to the grid but sustains till the end of the channel. In 2DF1, the intensity increases close to the grid till it reaches a peak around $x/d_{min} \cong 180$, which we call the production region but farther downstream both RG1 and 2DF1 decay down to a low intensity. In 3DS1, the intensity seems to be half that of 2DF1 which is understandable as the blockage ratio of 3DS1 is also half that of 2DF1.

Figures 5.3a,5.3b and 5.3c compare the streamwise turbulence intensities

49
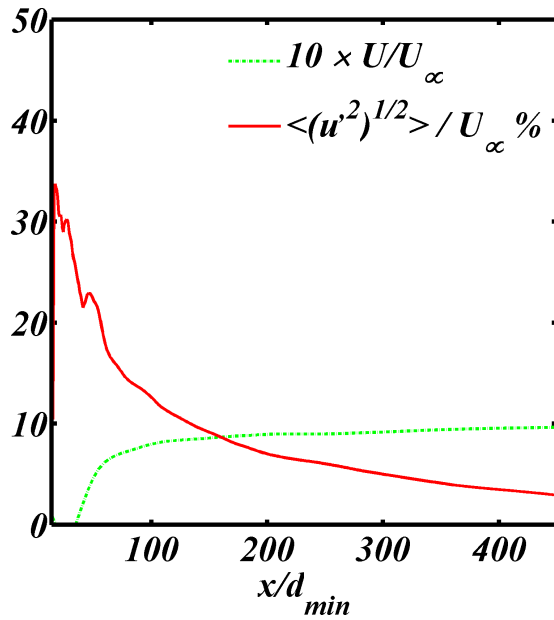
(a) RG1
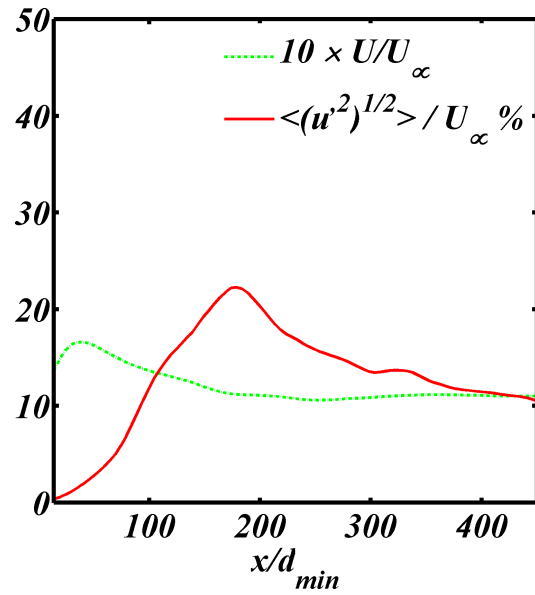
(b) 2DF1
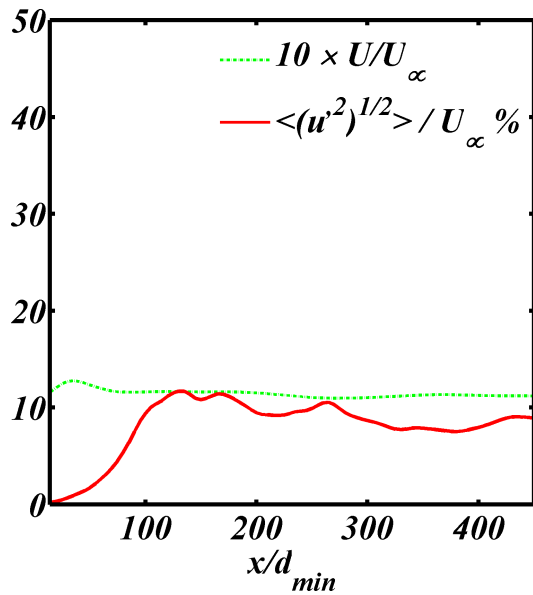
(c) 3DS1

Figure 5.2: Streamwise root mean square velocity and time averaged velocity along centerline of the channel.

$\langle (u')^2 \rangle^{1/2}/U_\infty$ along pencils in the streamwise direction of the channel, starting at various $(0, y, z)$ locations as indicated by the different colors.

The peak intensities in the RG1 case occurs very early downstream but then dies down rapidly (possibly indicating rapid mixing). The peak intensities in the 2DF1 is comparable to RG1, but the peaks in the 3DS1 are about 50% lower. The locations of the peaks in the 2DF1 and 3DS1 occur at similar locations between $x/d_{min} = 25-180$. Furthermore, the intensities in the 2DF and the 3DS is sustained for much longer downstream than in the RG1 – in the former two the intensities are still significant at the end of the channel. But although the 3DS1 shows lower peak intensities, the level of intensity towards the end of the channel after $x/d_{min} \approx 200$ is only slightly lower than in the 2DF1 – this is remarkable considering that the blockage ratio in the 3DS1 is 15%, which is half that of the 2DF1. In fact, the intensity profile in the 2DF1 is declining faster than in the 3DS, so it is possible that in a longer channel the 3DS1 may yet show higher level much further downstream – this will be investigated in the next section.

Figures 5.4 show the mean streamwise velocity, $U(y)/U_\infty$, against the transverse coordinate, y/d_{min}, in different planes downstream of the channel as indicated by the colours. The RG1 mean flow is close to unity and nearly flat for $x/d_{min} > 150$. The 2DF1 mean flow shows a flat region with $U(y)/U_\infty \approx 1.2$ in the central portion, and $U(y)/U_\infty \approx 0.85$ further out from the center at $x/d_{min} \geq 150$. This profile then smoothens out and decays to lower peak values for $x/d_{min} > 150$. The 3DS1 profile at $x/d_{min} = 150$ is nearly flat at a level comparable to the 2DF1 at $U(y)/U_\infty \approx 1.1$, but further downstream develops a central plateau like the 2DF1 case that flattens at
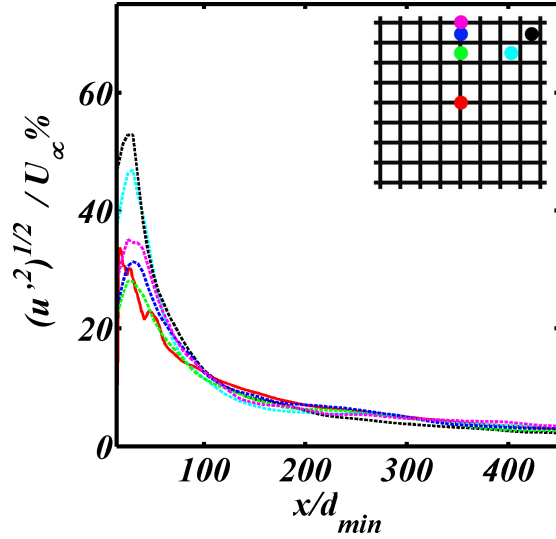
(a) RG1
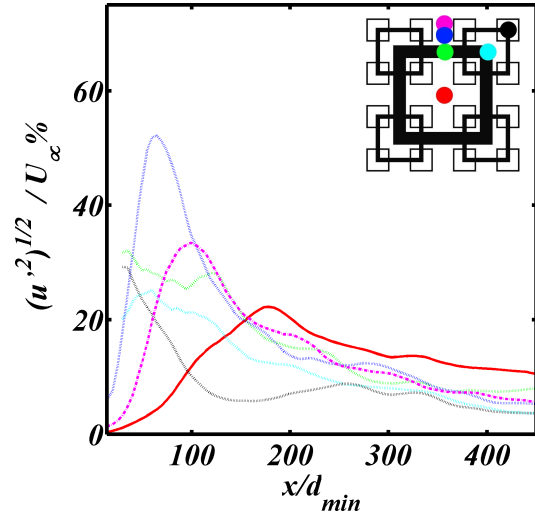
(b) 2DF1
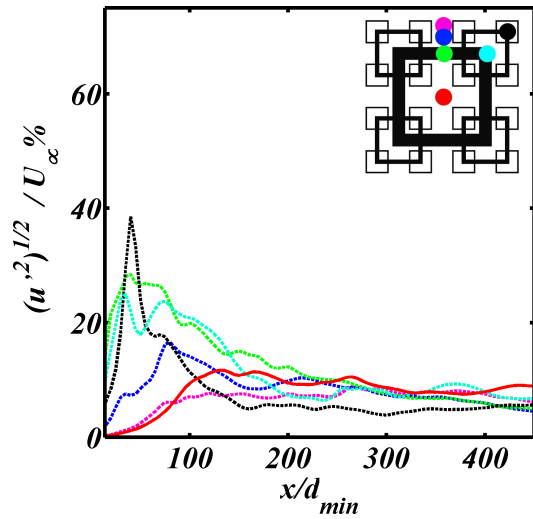
(c) 3DS1

Figure 5.3: Streamwise root mean square velocity along x-axis of six different pencils in yz-plane as shown in the legends.
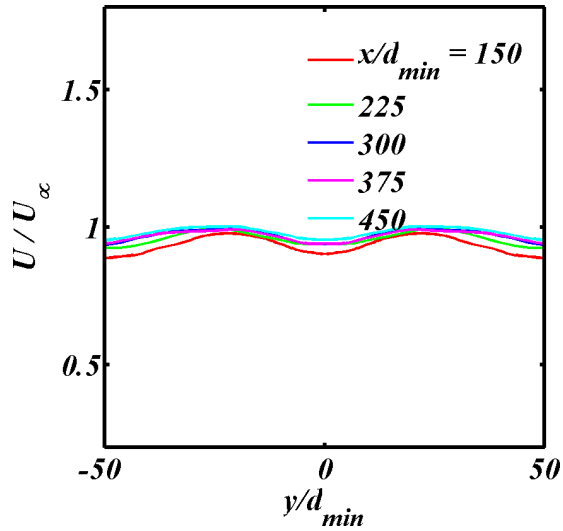
(a) RG1
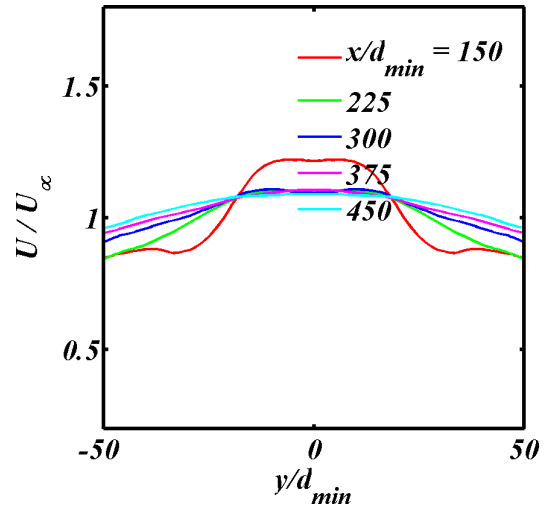
(b) 2DF1
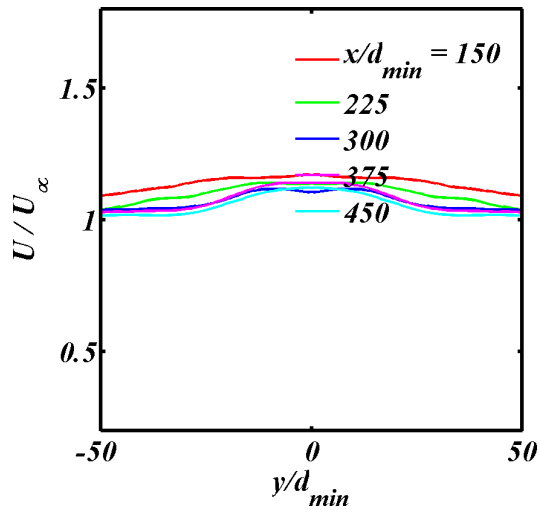
(c) 3DS1

Figure 5.4: Time mean of x-component of velocity at five different locations from $x/d_{min} = 150$ to $x/d_{min} = 450$ along y-axis where z=0.

the edges close to unity.

Figures 5.5 show the streamwise turbulence intensites, $\langle (u')^2 \rangle^{1/2}/U_\infty$ against y/d_{min}, for the three grid cases. The RG1 is essentially flat at $x/d_{min} = 150$ around 8% and then decaying towards zero further downstream, and the 2DF1 starts at much higher intensity of around 25% and decays to a nearly flat 10% by the end of the channel. In the 3DS1, the intensity averages around 10% throughout the length of the channel although it is much more peaked in the center than in the RG1 or the 2DF1 grids, which suggests that the turbulence activity is more confined within a narrower central region.

Figures 5.6 and 5.7 are the transverse velocity counterparts to Fig.5.4 and Fig.5.5 respectively, $V(y)/U_\infty$ and $\langle (v')^2 \rangle^{1/2}/U_\infty$, against the transverse direction, y/d_{min}, taken in the same yz-planes as before. Figures 5.6 show that mean y-velocity is almost always negative for 2DF1 and 3DS1 case. Figure 5.7 show that y-intensity is highest at the center in 2DF1 and lowest at the center in 3DS1.

Figures 5.8 and 5.9 are the vertical velocity counterparts to 5.4 and 5.5, respectively, $W(y)/U_\infty$ and $\langle (w')^2 \rangle^{1/2}/U_\infty$, against the transverse direction, y/d_{min}, taken at different stations along the channel as indicated by the colours in the legend.

Figure 5.4, 5.6 and 5.8 show that the mean velocities in the lateral directions are on average close to zero. This is excepted because the inflow is streamwise. However, the order of magnitude of the turbulence intensities in the lateral directions, and also in 5.3, in the respective grids are non-zero and of comparable magnitude, indicating roughly isotropic production of turbulence energy in all cases.

Figure 5.10a, 5.10b and 5.10c show the turbulence energy frequency spectrum
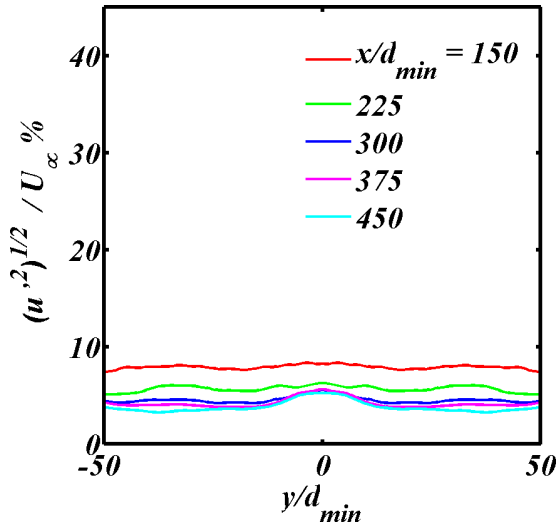
(a) RG1
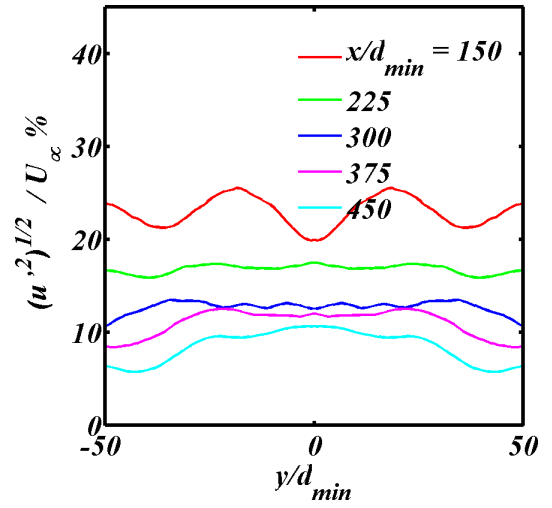
(b) 2DF1
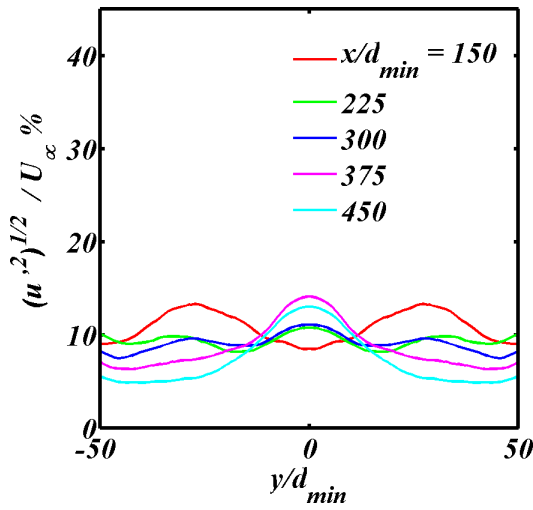
(c) 3DS1

Figure 5.5: Root mean square of x-component of velocity fluctuations at five different locations from $x/d_{min} = 150$ to $x/d_{min} = 450$ along y-axis where z=0.
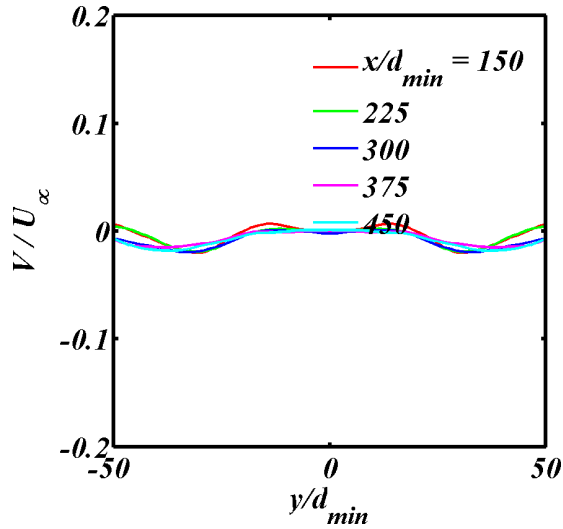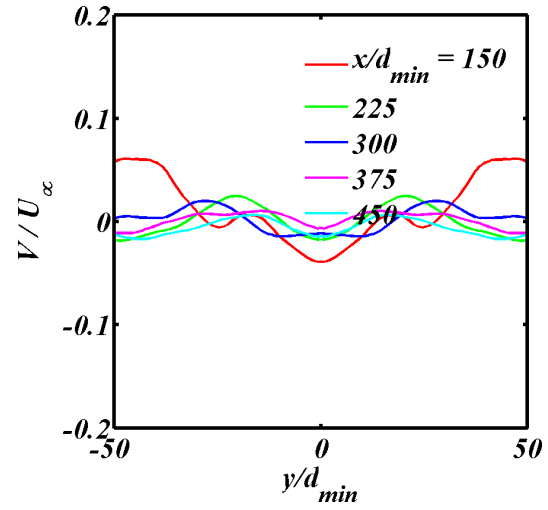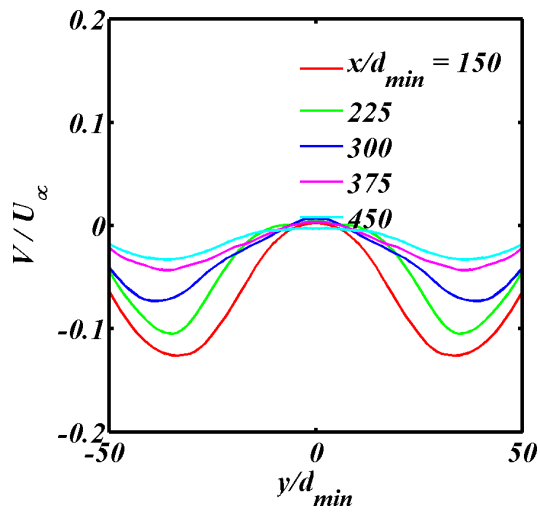
(a) RG1

(b) 2DF1

(c) 3DS1

Figure 5.6: Time mean of y-component of velocity at five different locations from $x/d_{min} = 150$ to $x/d_{min} = 450$ along y-axis where z=0.
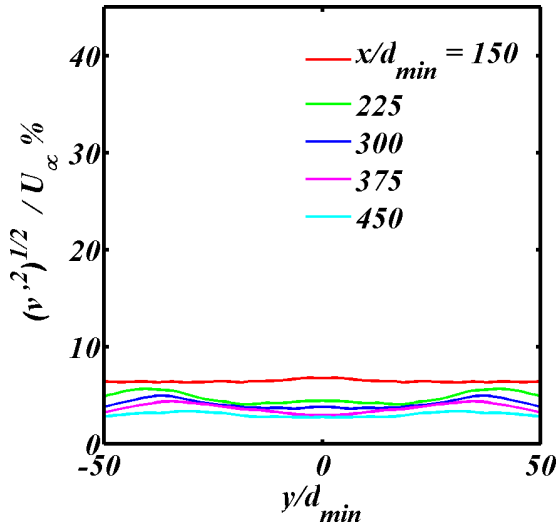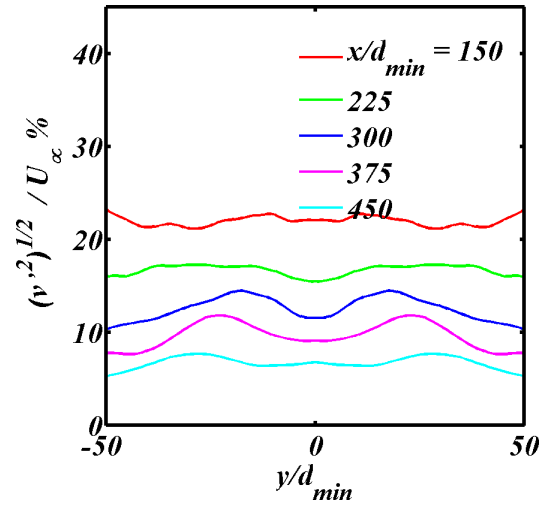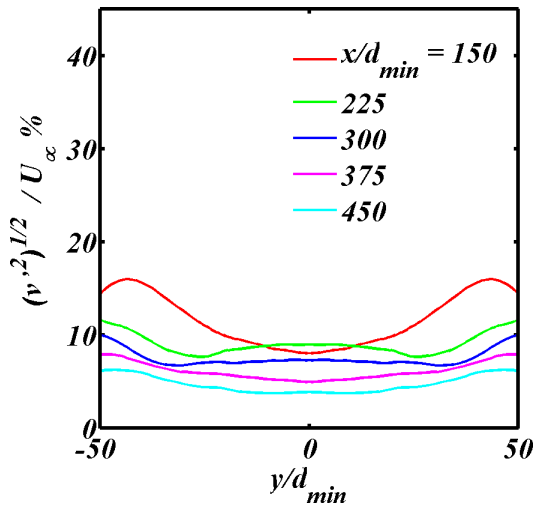
(a) RG1

(b) 2DF1

(c) 3DS1

Figure 5.7: Root mean square of y-component of velocity at five different locations from $x/d_{min} = 150$ to $x/d_{min} = 450$ along y-axis where z=0.
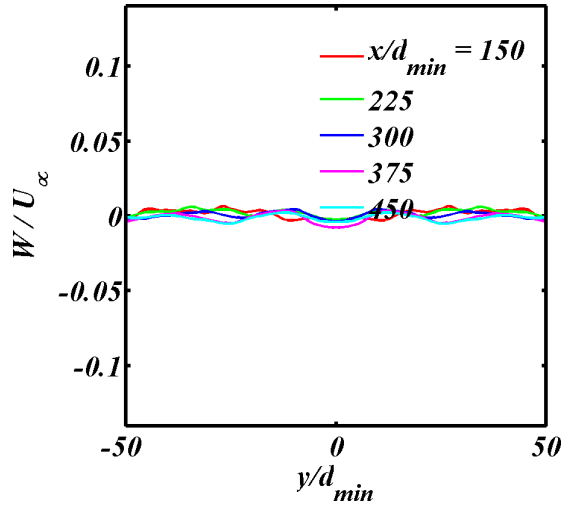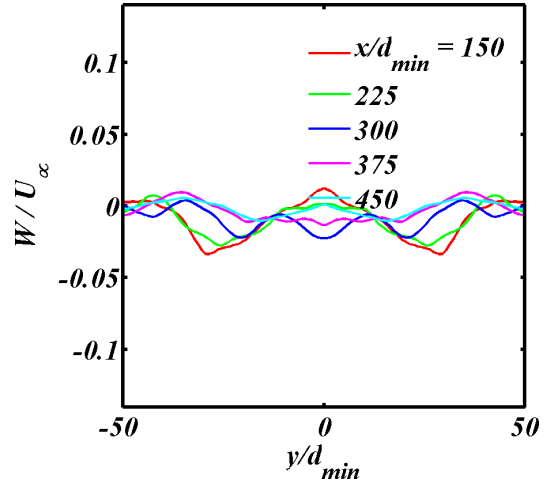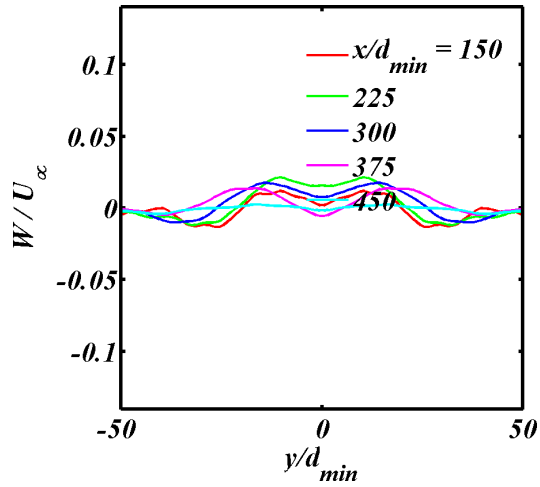
(a) RG1

(b) 2DF1

(c) 3DS1

Figure 5.8: Time mean of z-component of velocity at five different locations from $x/d_{min} = 150$ to $x/d_{min} = 450$ along y-axis where z=0.
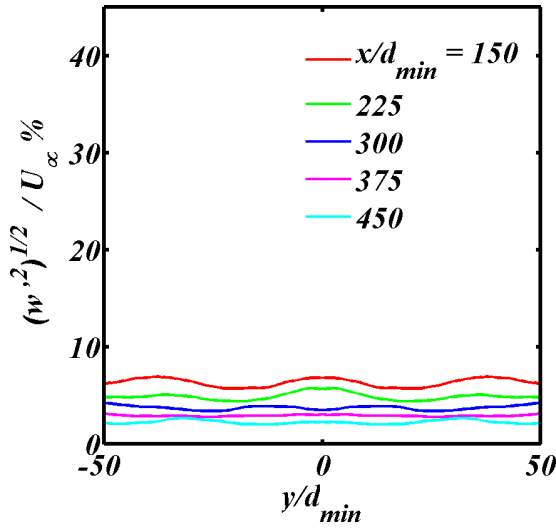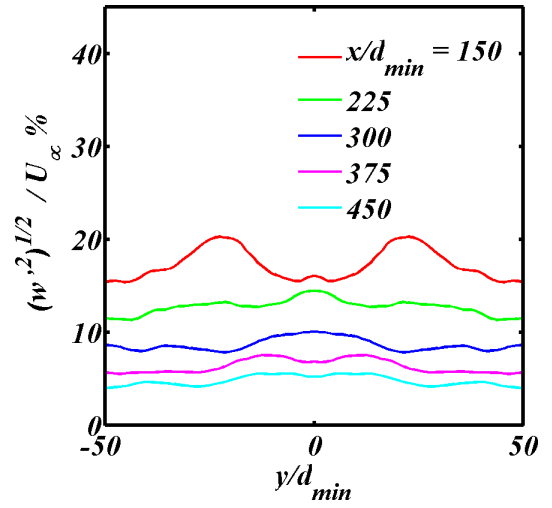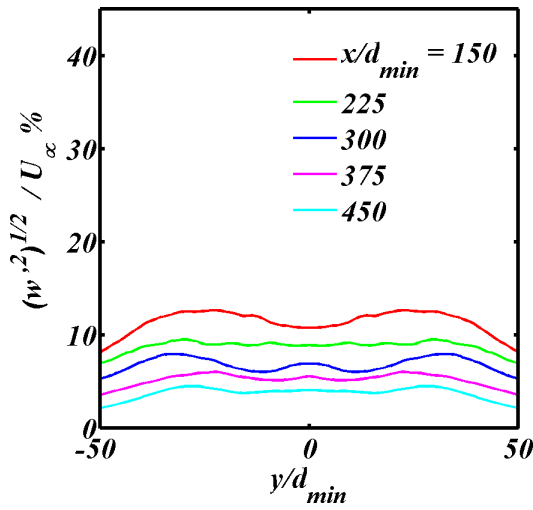
(a) RG1

(b) 2DF1

(c) 3DS1

Figure 5.9: Root mean square of z-component of velocity at five different locations from $x/d_{min} = 150$ to $x/d_{min} = 450$ along y-axis where z=0.
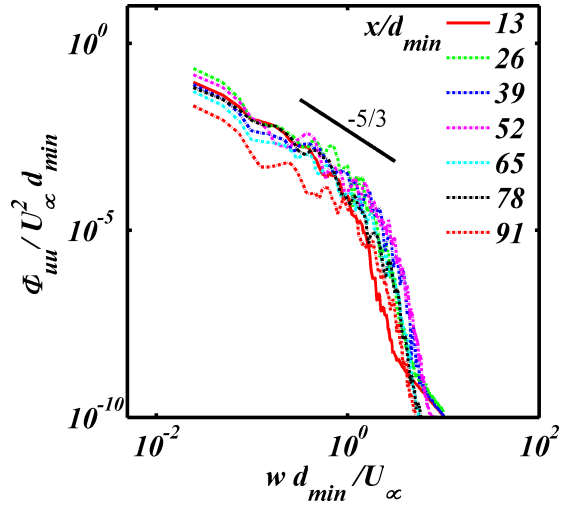
(a) RG1
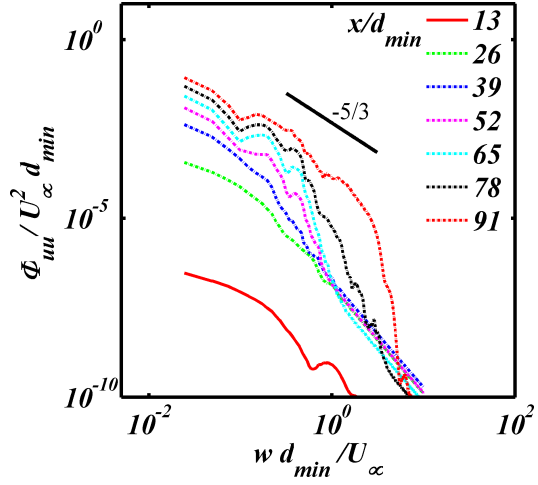
(b) 2DF1
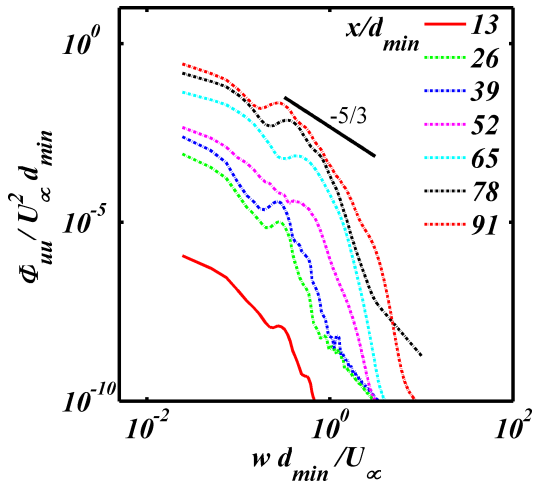
(c) 3DS1

Figure 5.10: Log-log of the Power spectra of streamwise component of velocity fluctuation at seven locations from $x/d_{min} = 13$ to $x/dmin = 91$.

along the centerline of the channel in the production region. The probes were located at different x_k/d_{min}, $(k = 1, 2, ..7)$ that recorded streamwise velocity $u(x_k, t)$ of the flow which were converted into frequency spectrum using Welch window. Equation (2.22) is used to convert the velocity field into turbulence energy spectrum as explained in [5], [4]. Taylor's frozen field hypothesis is then applied to convert the freqeuncy spectra into wavenumber spectra as it implies that frequency spectrum $K \sim w/U_\infty$ where K is the wavenumber as defined in equation (2.22). The results of 5.10a and 5.10b match with those of [24] and therefore validate the accuracy of our numerical simulation. 5.10c shows log-log of turbulence energy spectrum $E(K) = \Phi_{uu}/U_\infty^2 d_{min}$ against Kd_{min} $(\omega d_{min}/U_\infty)$ from 3DS1. The Kolmogorov turbulence $E \sim K^{-5/3}$ develops quite early in RG1 and over a range of scales in the 2DF1, $K^{-5/3}$ spectrum develops further downstream $x/d_{min} \geqslant 90$. But in 3DS1 the range of $K^{-5/3}$ spectrum is much smaller. The spike in 3DS1 at around 8×10^{-2} could be the reason of the turbulence caused from the smallest frame in 3DS1. Clearly 3DS1 delays the onset of fully developed turbulence as compared to RG1 and 2DF1. 2DF1 clearly follows $-5/3^{rd}$ law at the probes farthest from the grid and RG1 displays quick energy dissipation as there is no significant difference in the values of Φ_{uu} downstream of the channel. It can be concluded that in the production region, 2DF1 and 3DS1 display trends towards Kolmogorov energy spectrum but the mechanism for the energy cascade is not fully apparent [29], [5], [11].

Figures 5.11 show the root mean square vorticity $(\omega'^2(x))^{1/2}$ profiles of RG1, 2DF1 and 3DS1 grids respectively, along the axial direction of the channel. RG1 shows higher vorticity intensity which also decays very fast. Theory suggests that vortex

(a) RG1

(b) 2DF1

(c) 3DS1
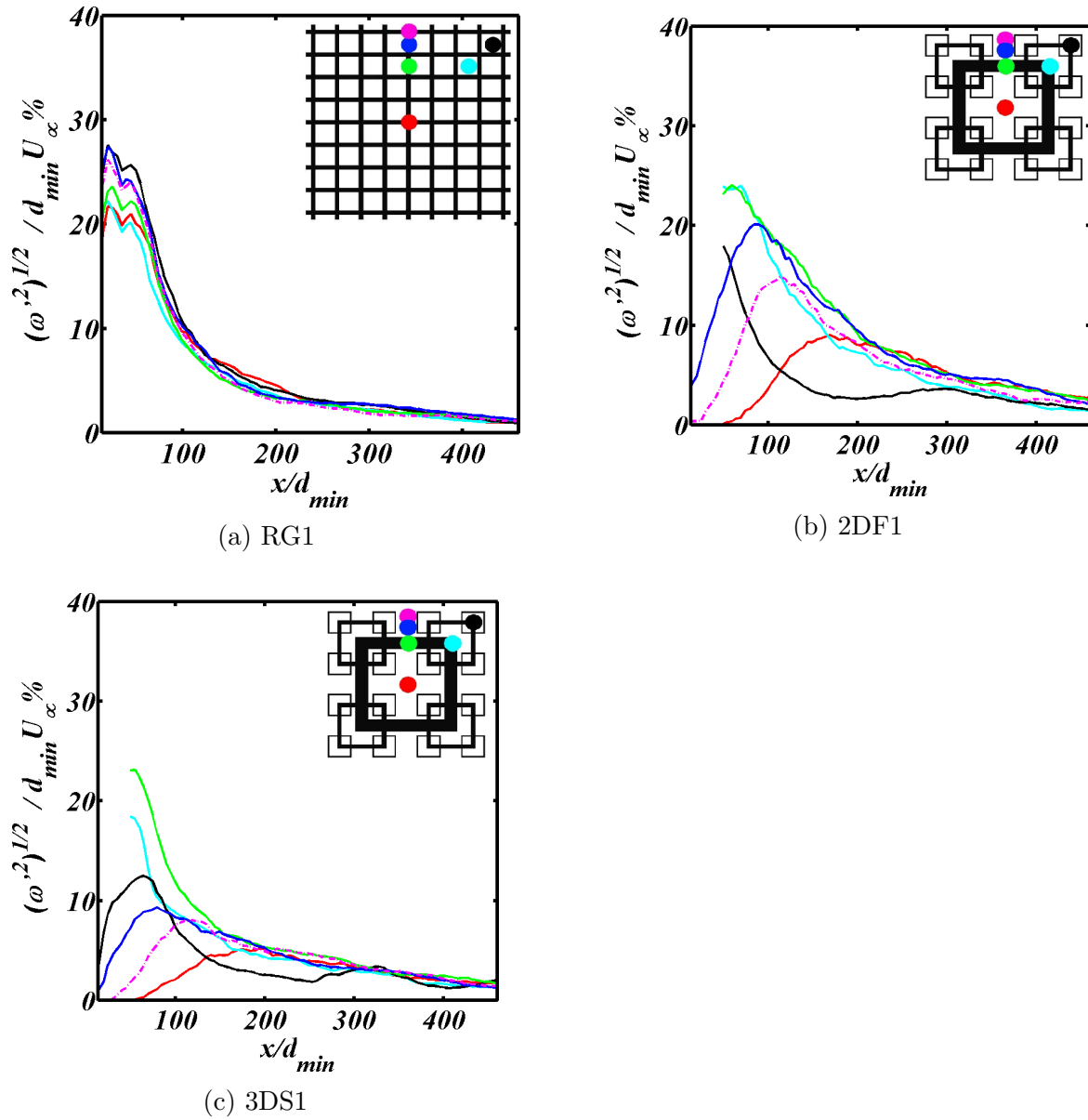
Figure 5.11: RMS of the streamwise component of vorticity along x-axis at six different points in the yz-plane shown in colors on the grid legend.

tubes play vital role in energy transfer in turbulence due to their interaction with the mean flow and each other [29]. However vortices by themselves are not effective in mixing since the local motion is like solid body rotation. The turbulent vorticity production and decay is notably different in the 2DF1 and 3DS1. Both show staggered or delayed peaks downstream depending upon the pencil - an indication of inhomogeneity. Although the locations of the peaks in the 2DF1 and 3DS1 are at similar yz-planes, the peaks in 3DS1 are about 50% of that in the 2DF1 along most of the pencils.

Mean scalar transport profiles of RG1, 2DF1 and 3DS1 are shown in Fig.5.12 for a range of turbulence Schmidt numbers $Sc_t = \frac{\nu_t}{Dt}$ where $\nu_t = 1d^3_{min}/U_\infty$ is the local eddy viscosity and $D_t = 0.25, 0.5, 0.75, 1, 1.33, 2d^3_{min}/U_\infty$ is the diffusivity. The passive scalar is a line along the z-axis where $x/d_{min} = 5, y/d_{min} = 0$, with initial concentration set equal to unity. The trends in all scalar concentrations for different Sc_t values are very similar quantitatively, with the only exception of $Sc_t = 0.5$ at where higher intensity can be seen in Fig.**??**.

RMS scalar fluctuations along centerline of RG1, 2DF1 and 3DS1 is displayed in Fig.5.13 for a range of turbulence Schmidt numbers $Sc_t = 0.5, 0.75, 1, 1.333, 2, 4$. As Sc_t increases, concentration variation of scalar decays steadily downstream of the channel. For $Sc_t > 0.5$ the scalar concentration fluctuations are also qualitatively similar. This is an indicator of better mixing and Fig.5.13c shows how concentration intensity rises throughout for all variations of Sc_t consistently. This is equivalent of a concentrated dye being placed in the fluid at the center and recording the variation in its concentration along the centerline of the channel. At the end, the dye will have
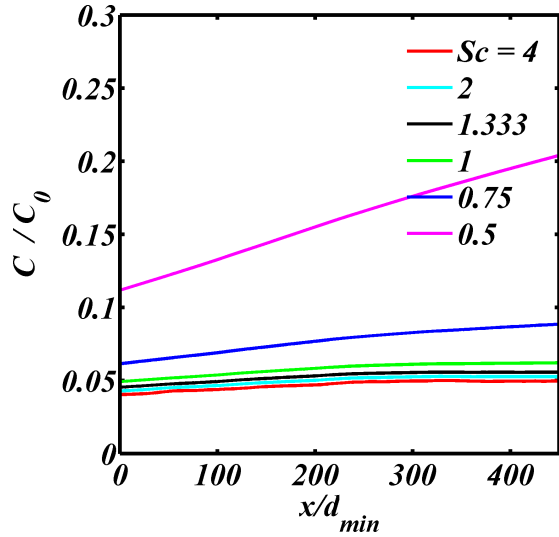
(a) RG1
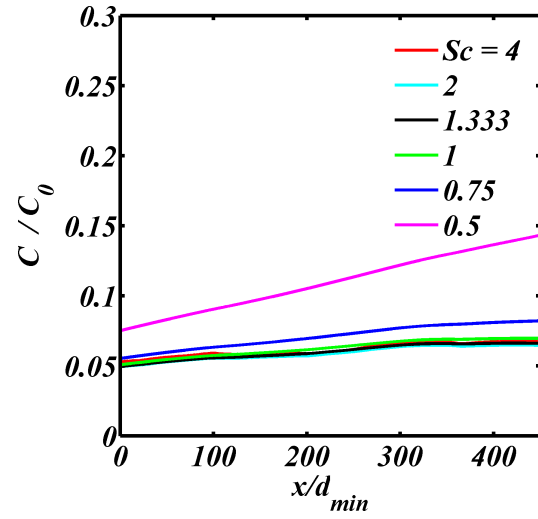
(b) 2DF1
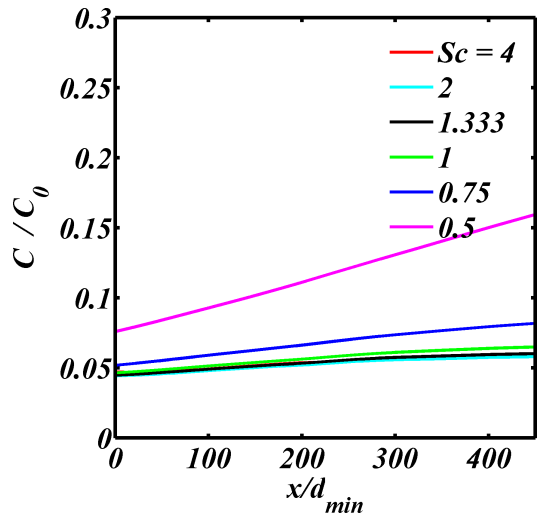
(c) 3DS1

Figure 5.12: Streamwise mean scalar concentration profile of a passive scalar pencil along centerline of the channel with six different turbulence schmidt numbers Sc_t.
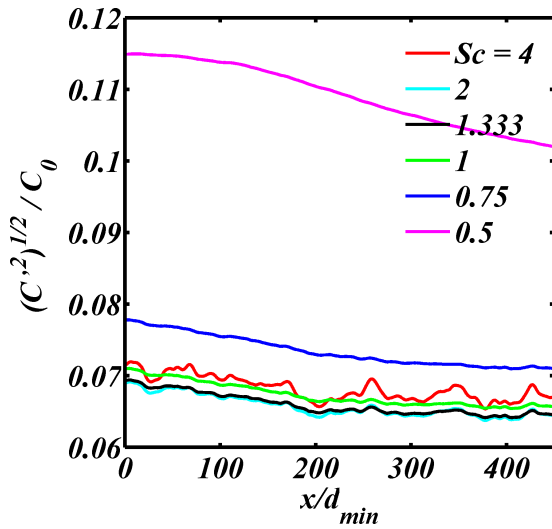
(a) RG1
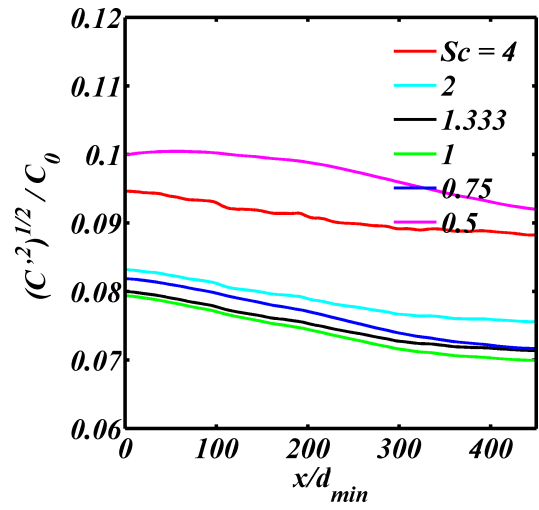
(b) 2DF1
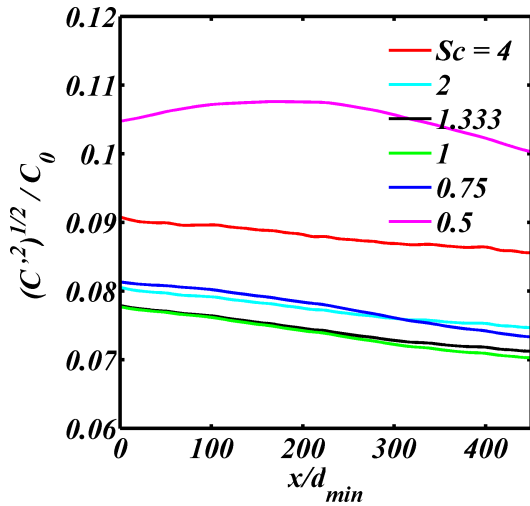
(c) 3DS1

Figure 5.13: Streamwise RMS fluctuations of the concentration of a passive scalar pencil along centerline of the channel with six different Schmidt numbers $Sc_t = 0.5, 0.75, 1, 1.333, 2, 4$.

dissolved in 3DS1 as well as it would in the grids 2DF1 and RG1 grids which have a much higher blockage ratio than 3DS1. Because of the large parameter space that 3DS grids offer, one can cover a vast range of parametric studies of turbulence which spans almost all aspects of grid generated turbulence.

5.2   Comparison of RG2, 2DF2 and 3DS2

The study of 2DF1 and 3DS1 in the previous section reveals that the domain considered in the previous section is not sufficiently large to make conclusive remarks on how turbulence is carried farther downstream of the grid. Keeping all other parameters the same as in Case 1, a longer channel is now considered. The new grid Cases with channel length $L_x/d_{min} = 576$, $L_y/d_{min} = L_z/d_{min} = 115.2$ are named RG2, 2DF2 and 3DS2 and the aspect ratios of the new channel are $5 : 1 : 1$. This does not change the numerical method but due to the addition of millions of new discretization cells to the simulation, number of CPUs required has to increase to be able to complete the simulation withing a reasonable time. 2560 CPU cores on Shaheen HPC platform at KAUST University were employed in a project for the simulation. Around 50 hours of clock time per simulation generated the results discussed in this section. The clocktime for postprocessing of those results was an additional 4 hours per simulation on 16 CPU cores. Moreover, the design of the grid and channel, adjustments in the algorithm according to the new configuration and continuous monitoring of the simulations adds additional clock time.

Fig.5.14 shows root mean square velocity fluctuation contours in the yz-planes at
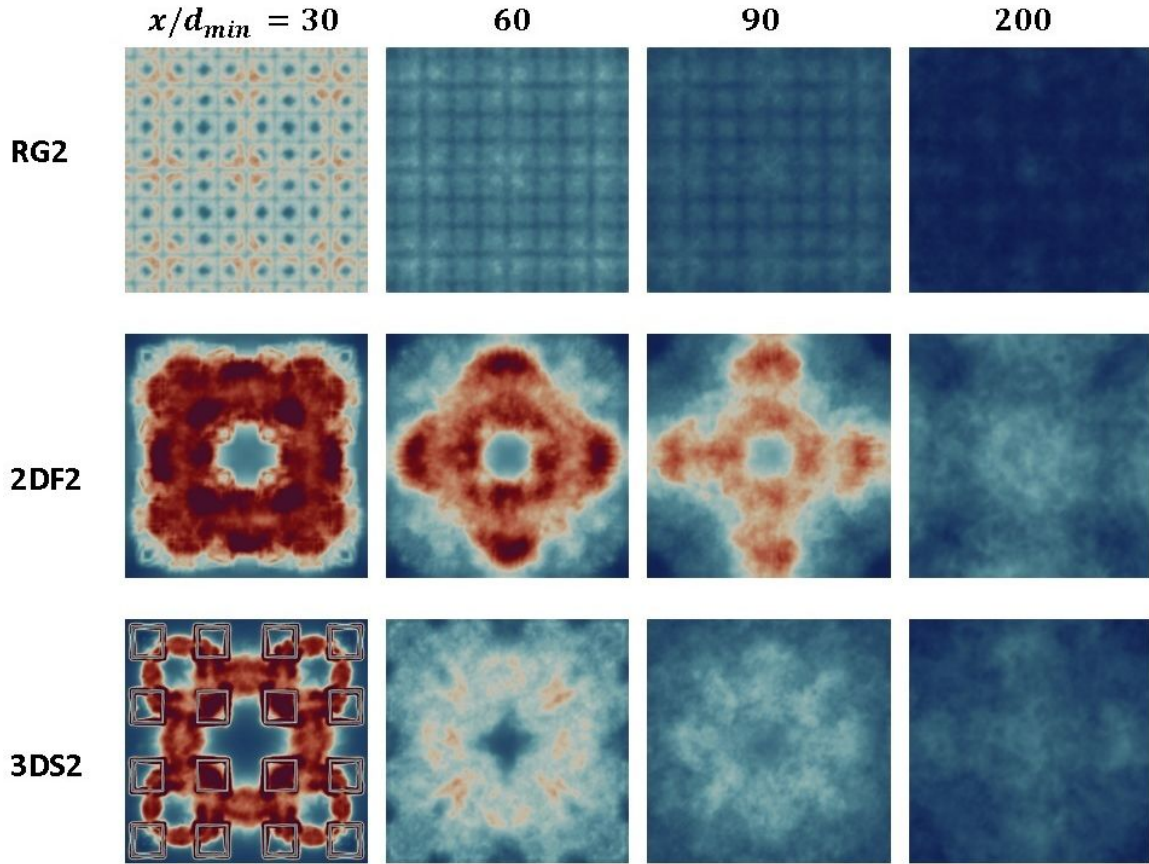
Figure 5.14: RMS velocity fluctuations of RG2, 2DF2 and 3DS2 in the yz-plane at locations $x/d_{min} = 30, 60, 90, 200$ where dark blue color indicates RMS velocity fluctuation value of 0 and dark red color indicates RMS velocity fluctuations at value of 0.5. Lighter colors indicate values somewhere in between. The RMS is calculated over the time from $300T$ to $600T$.

four different downstream locations of the RG2, 2DF2 and 3DS2 grids. As we move farther from the grid we see the blue color dominating which shows that intensity is decreasing. In RG2, even at $x/d_{min} = 30$ we can already see that the intensity is not as high as that shown by 2DF2 and 3DS2. The signatures of the grids can be seen in both 2DF2 and 3DS2 all the way down to $x/d_{min} = 200$ but in RG2, the image of the grid has almost complete drowned out that far away from the grid.

RMS velocity fluctuations are retained in 2DF2 and 3DS2 even farther downstream of the conduit which, considering the low blockage ratio and low peak intensity of 3DS2
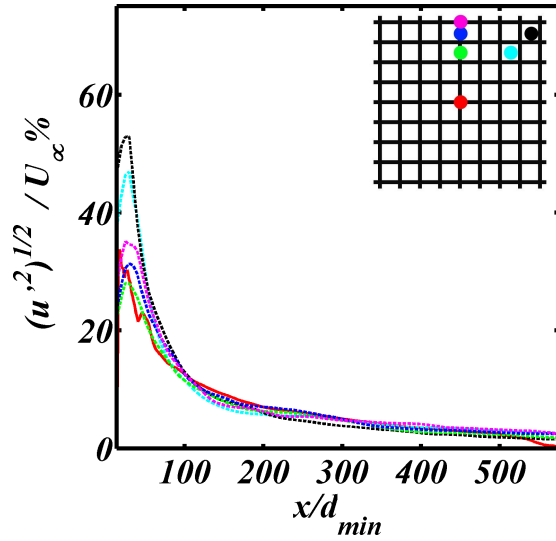
(a) RG2
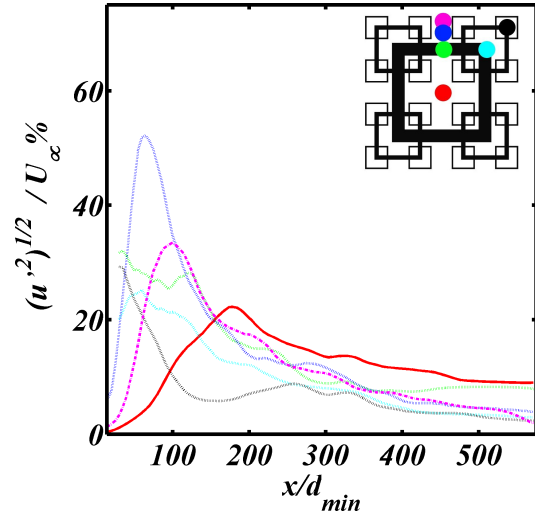
(b) 2DF2
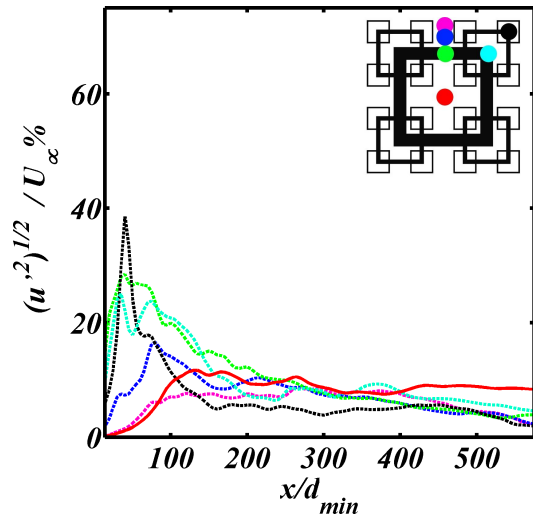
(c) 3DS2

Figure 5.15: Streamwise root mean square velocity percentage profile along x-axis of six different points in yz-plane as shown in the legends.

it wasn't expected to happen as seen in Fig.5.15. In Fig.5.17c this can be more clearly observed along the centerline. Both 2DF2 and 3DS2 show a signature of turbulence and mixing far downstream of the conduit and both grids retain intensity of around 10% for $x/d_{min} > 400$.
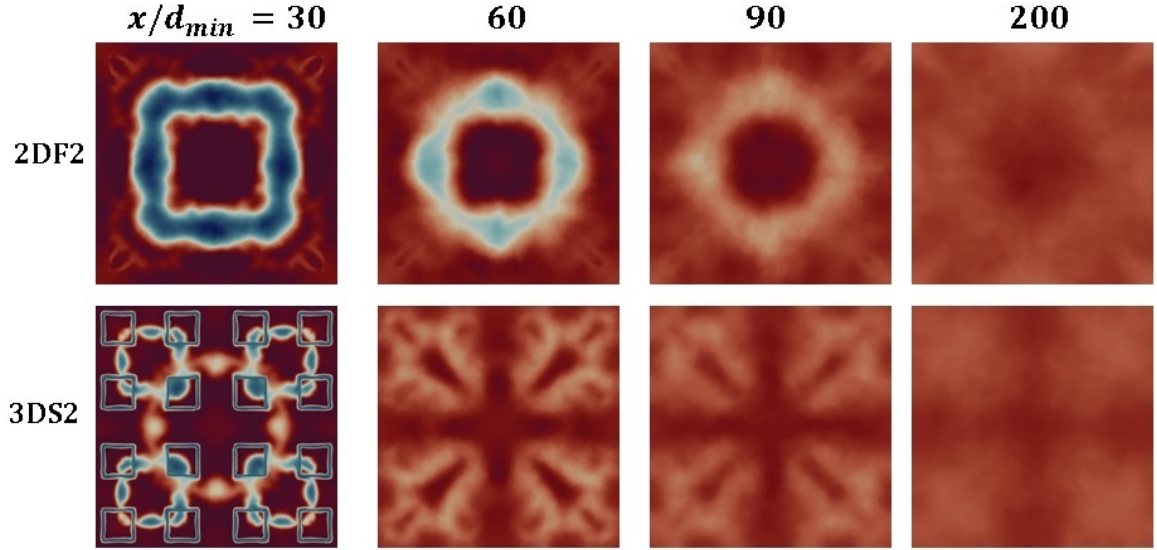
Figure 5.16: Mean x-components of velocity contours of 2DF2 and 3DS2 in the yz-plane at locations $x/d_{min} = 30, 60, 90, 200$ where dark blue color indicates mean velocity value of -0.5 and dark red color indicates mean velocity of 1.5. Lighter colors indicate values somewhere in between. The mean is taken over the time from $300 - 600T$

Contours of mean velocity profiles of 2DF2 and 3DS2 are shown in figure 5.16. In 2DF2 reverse flow can be observed in the form of the blue color present at $x/d_{min} = 30 - 90$ while in 3DS the signature of the reverse flow has already died out at $x/d_{min} = 60$. In both 2DF2 and 3DS2, symmetry of the flow is evident as suggested by the theory of homogeneous turbulence [4]. At $x/d_{min} = 200$, both grids show similar averaged velocities except that 2DF2 shows higher velocity along the centerline whereas in 3DS2 higher average velocities are along planes $y = 0$ and $z = 0$.

In Fig.5.17c, mean velocity of RG2 and 2DF2 are similar but rms of velocity fluc-
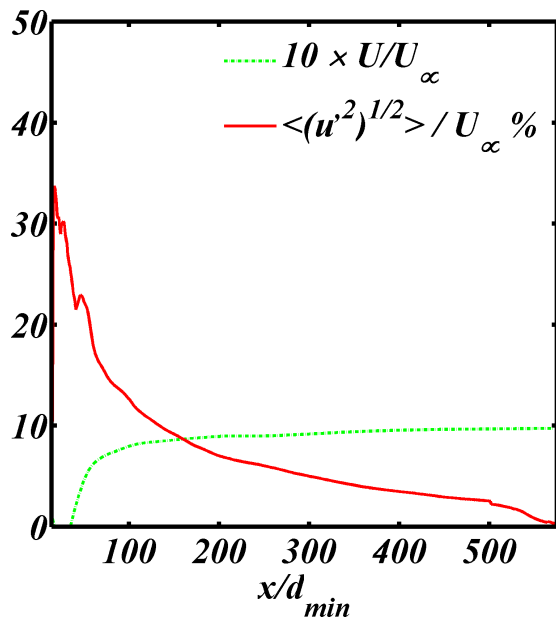
(a) RG2
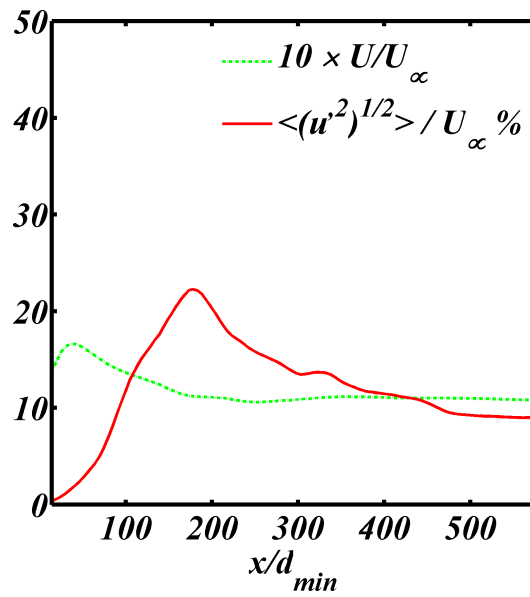
(b) 2DF2
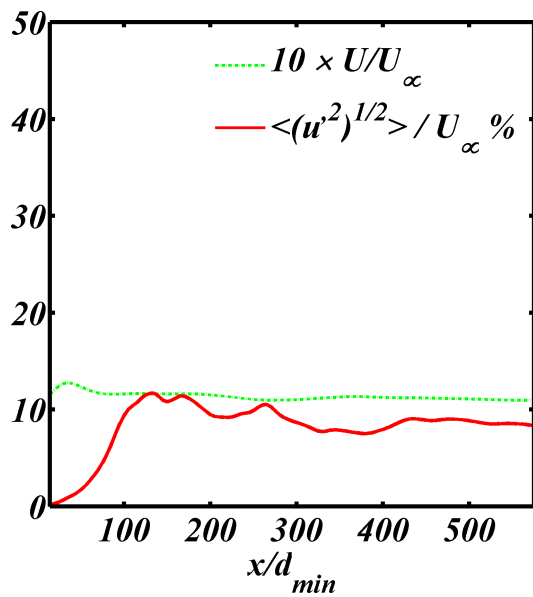
(c) 3DS2

Figure 5.17: Streamwise root mean square percentage velocity and time mean velocity along centerline of the channel.

tuations in 2DF2 are higher than 3DS2 due to its higher blockage ratio. However farthest downstream of the grid, both 2DF2 and 3DS2 display sustained rms fluctuations. 3DS2 having blockage ratio of only 15% compared to 32% of 2DF2, this is remarkable. Therefore further investigation of 3DS grids having comparable blockage ratios to those of RG and 2DF will be covered in the next section.
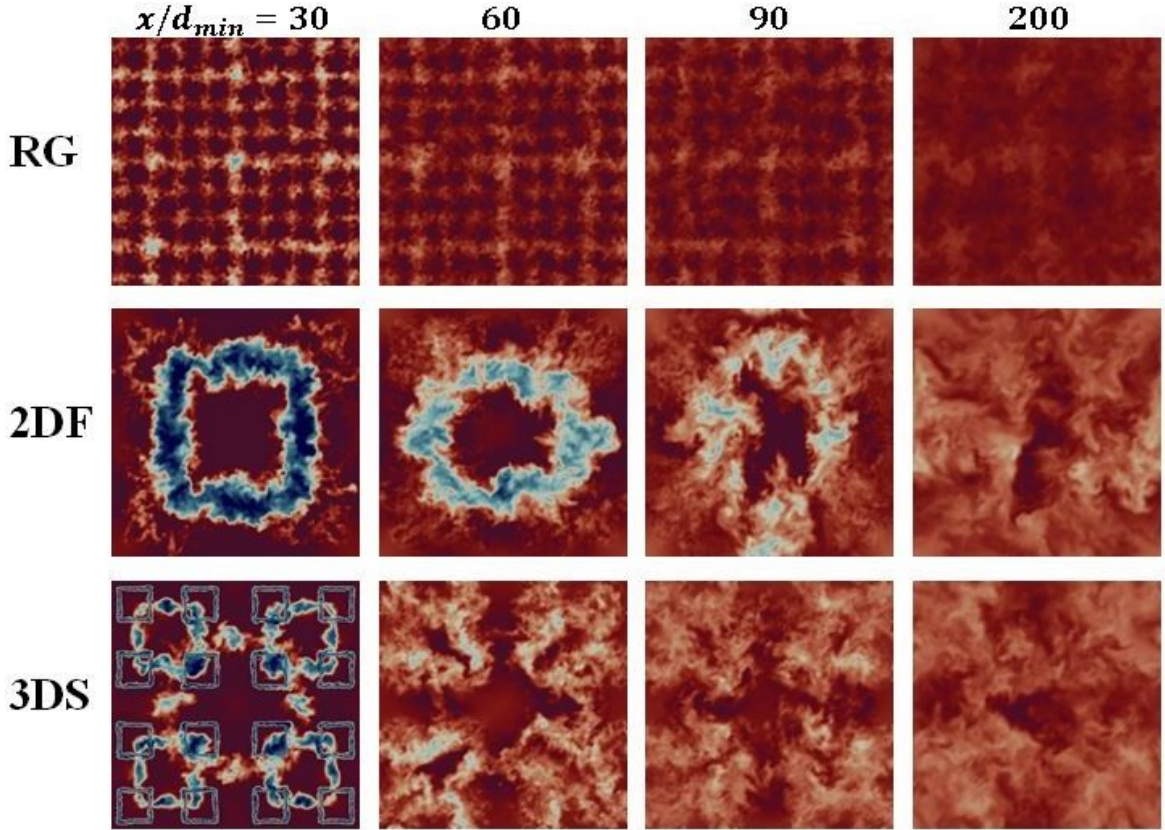
Figure 5.18: x-component of instantaneous velocity contours of RG2, 2DF2 and 3DS2 in the yz-plane at locations $x/d_{min} = 30, 60, 90, 200$ where dark blue color indicates velocity -0.5 and dark red color indicates velocity 1.5. Lighter colors indicate values somewhere in between. The velocity contour snapshots are taken at the simulation time $500T$.

In the figure 5.18 we see instantaneous streamwise velocity component slices in the yz-plane at locations $x/d_{min} = 30, 60, 90, 200$ of the conduit. At $x/d_{min} = 30$, RG2, shows almost no reverse flow unlike 2DF2 and 3DS2 where dark blue color represents

reverse flow. At $x/d_min = 60$, only 2DF2 shows signs of reverse flow still present where as in RG2 and 3DS2 the flow is directed along the streamwise direction. The effect of the grids is visible even at $x/d_{min} = 90$ in all three grids but 2DF2 shows more randomness which indicate better mixing that RG2 and 3DS2 and it can be seen that this is still the production region $10 \leq x/d_{min} \leq 180$ of the conduit. At $x/d_{min} = 200$ the velocity field has homogenized in all three grids, the contours of 2DF2 and 3DS2 are very similar and in RG2 no variations are visible from this point on.

All the plots of 2DF2 and 3DS2 show strong evidence of entrainment. Entrainment occurs across the boundary of two bodies of flows, such as in the boundary of jets and wakes. Swirling and fluctuating motions regularly engulf small bodies of fluid from the outside to the inside. In Fig.5.18 it can be seen that although the turbulence along the centerline is primarily low, but it is being continuously swept from around the centerline into the center. Thus it is a mechanism which maintains the centerline turbulence intensity for so long downstream. Such a mechanism is not possible in the case of RG grids which are homogenized very early.

Mean scalar concentration along the centerline of the channel is shown in Fig.5.19 for a range of schmidt number values $Sc = 0.5, 0.75, 1, 1.3, 2, 4$ as seen in the legend. The concentration profiles of RG2, 2DF2 and 3DS2 are very similar. Increasing the length of channel has no effect on the mean scalar diffusion in the sense that the mean scalar concentration in steady state is almost constant all along the centerline of the conduit for all variations of the turublent schmidt number except when Schmidt number is 0.5. As schmidt number grows, diffusivity is reduced and hence the rate of increase in concentration as a function of channel length decreases with increase
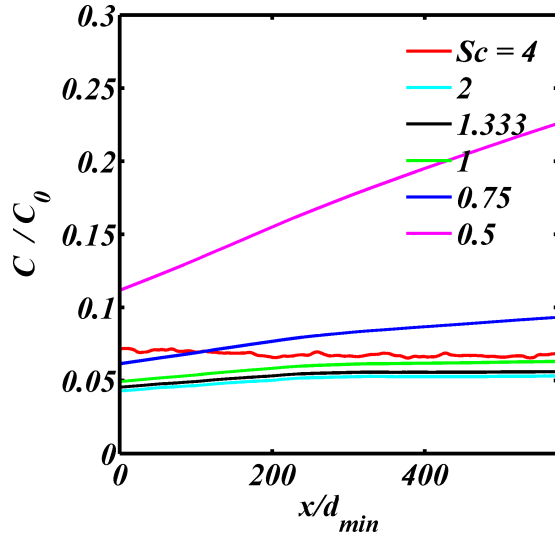
(a) RG2
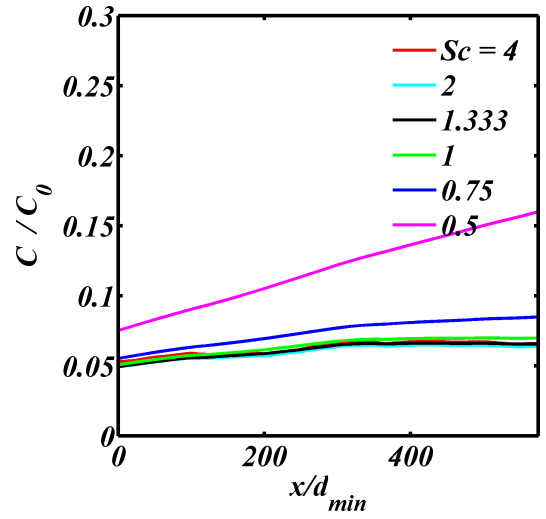
(b) 2DF2
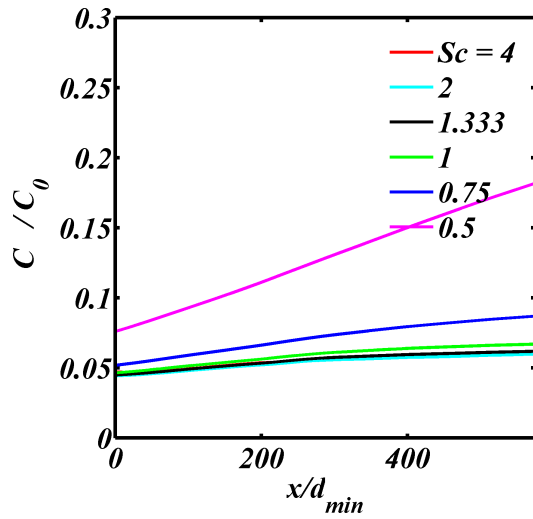
(c) 3DS2

Figure 5.19: Streamwise mean scalar concentration profile of a passive scalar pencil perpendicular to the centerline of the channel with seven different Schmidt numbers.

in schmidt number. This indicates that steady state is reached and the increase in mean scalar concentration along the axial direction of the flow indicates homogeneity farthest downstream of the channel. The mean scalar profile of 3DS2 lies somewhere between those of RG2 and 2DF2 with RG2 having the highest concentrations followed by 3DS2, while 2DF2 displays slightly lower concentration of the passive scalar downstream.

Root mean square of scalar concentration fluctuations in axial direction of the flow for RG2, 2DF2 and 3DS2 is shown in Fig.5.20. Highest levels of scalar fluctuations are seen in RG2 when schmidt number is very small. But as the turbulence schmidt number grows, the scalar fluctuations rise in 2DF2 grid as well as in 3DS2. Overall, the concentration fluctuations decrease downstream of the channel and become almost constant after $x/d_{min} = 450$ for all the grids. From the graphs it can be stated that when schmidt number of the passive scalar increases, the concentration fluctuations rise in the multiscale grids. On the other hand increasing schmidt number does not affect the classical regular grid as much. An overall flat scalar concentration profile for all the grids indicates homogeneity and continuous mixing of the passive scalar. Lowest value of scalar concentration fluctuation is observed for $Sc = 1$ and highest value is observed for $Sc = 0.5$.
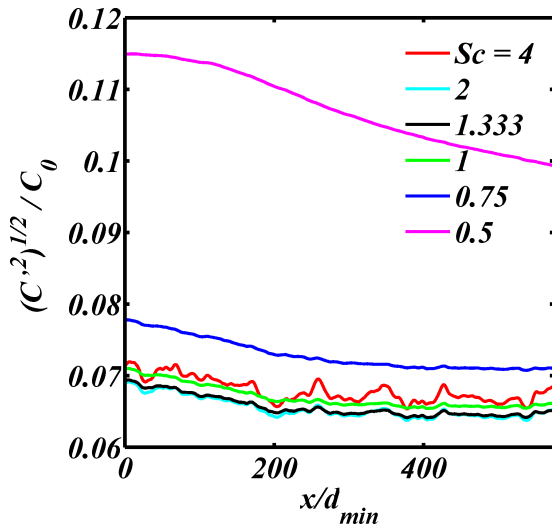
(a) RG2
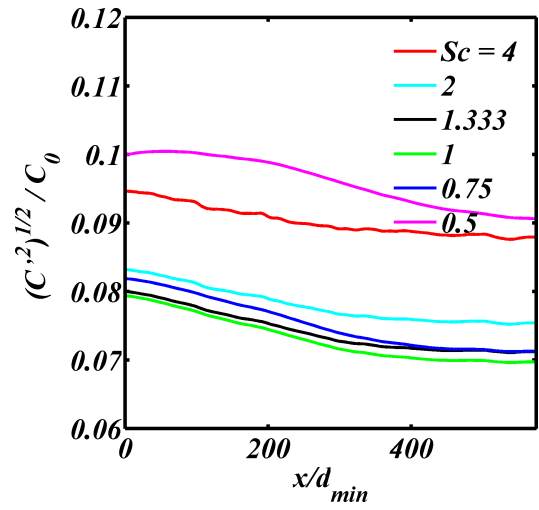
(b) 2DF2
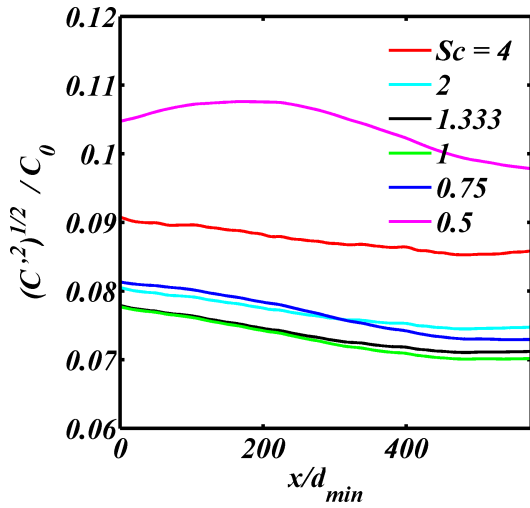
(c) 3DS2

Figure 5.20: Streamwise root mean square scalar diffusion profile of a passive scalar pencil perpendicular to the centerline of the channel with six different turbulence Schmidt numbers Sc_t.

5.3   Comparison of 3DS2, 3DS3, and 3DS4

The 3DS grids possess a much larger parameter space than 2D fractal grids. The new parameters exclusive to the 3DS grids are maximum blockage ratios $\sigma_{3DS}^{Max} = Max\{\sigma_0, \sigma_1, \sigma_2\}$ where σ_j's are the blockage ratios of the jth co-frame of the 3DS grid system, frame separation r_j and order of co-frame arrangement Z_j. In this section the 3DS grids 3DS2, 3DS3 and 3DS4 are compared as the grids have equal frame separation $\{r_1 = 17d_{min}, r_2 = 8.5d_{min}\}$ and the same order of co-frame arrangement Z_0, Z_1, Z_2 but different maximum blockage ratios. The blockage ratios of 3DS2, 3DS3 and 3DS4 are 15%, 24% and 32% respectively which is achieved by altering the thickness d_0 of the first co-frame of each of the sparse grid system. Since all other parameters are the same, this study will highlight the effect of variation in the blockage ratios of the grids. The set of simulations was also conducted using the robust finite volume based PISO algorithm on KAUST Shaheen HPC environment using C++ based toolbox. As before, probes and pencils were placed in the channel to record spatial and temporal sequences of data over a time over which the flow reached steady state. Over fifty thousand time steps of data is recorded and at the same time, complete snapshots of the domain at thirty random points in time are also saved. Due to limitations in data storage, not everything can be saved as the data generated by these simulations is very large.

Starting with 3DS2 as our base case we increase the maximum blockage ratio of the new grid 3DS3 to 24% and eventually reach 3DS4 whose blockage ratio is 32% which is equal to that of the 2D flat grids RG2 and 2DF2. There are many ways

(a) 3DS3   (b) 3DS4
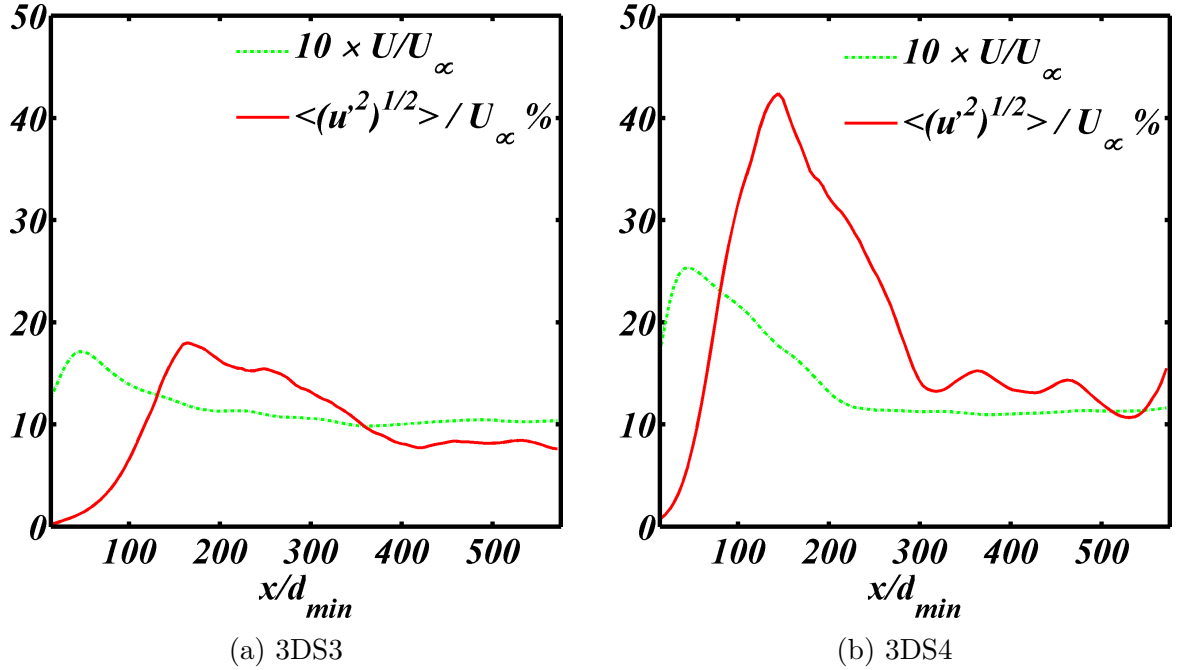
Figure 5.21: Streamwise component of the mean velocity in green and RMS velocity fluctuations in red along the centerline of the channel for sparse grids 3DS3 and 3DS4.

to obtain σ_{3DS}^{Max} and all the cases cannot be covered in this study, we have therefore restricted ourselves to minimalistic variation in the parameters, we selected a few cases vt altering the thickness d_0 of the largest co-frame. It should be noted that it is not necessary to only change the blockage ratio of only one of the three frames. We could as well have chosen to make the blockage ratios of all the frames equal but that would be a completely different comparison than the one as we are doing here with 2DF2 and RG2. The immense size of the new parameter space that the 3DS offers is impractical to be covered in one.

Fig.5.21a and Fig.5.21b show mean and RMS velocity profiles from the 3DS3 and 3DS4 grids and we are comparing them with the profiles of 3DS2 and 2DF2 as given in Fig.5.21a and Fig5.17b respectively. These results are remarkable as 3DS3 and 3DS4 generate higher peak intensities along the centerline of the grids than from 2DF2

77

with blockage ratio 32% which is the same as that of 3DS4. The intensity and average velocity of 2DF2 is roughly comparable to that of 3DS3. This is a remarkable reduction in the blockage ratio from 32% to 24%. If we compare the 3DS2 from figure 5.34 with 3DS3 and 3DS4 from Fig.5.21, the mean flow $U(\mathbf{x})$ develops in a similar manner in all the grids, it peaks around $x/d_{min} \cong 30$. The peak value in the mean $U(\mathbf{x})/U_\infty$ and rms velocity fluctuations $\langle (u'^2)^{1/2} \rangle / U_\infty$ is strongly dependent on σ_{3DS}^{Max} . The mean velocity peaks at $\cong$ 1.5, 1.8 and 2.6 in the 3DS2, 3DS3 and 3DS4 respectively. The rms turbulence intensities peak at $\cong$ 1.0, 1.9 and 4.3 respectively. The peak is most pronounced in 3DS4 and it decays down to around 12% at $x/d_{min} \cong 200$ and is then sustained at this level all the way down the channel. The rms turbulence peak intensity is around the same location $x/d_{min} \cong 150$ and the peak intensity in 2DF2(32%) is almost equal to that of 3DS3(24%). The peak intensity in 3DS4(32%) is almost 143% which is twice as high as that of 2DF2(32%), then it decays down until $x/d_{min} \geq 300$ where it oscillates around 15% to the end of the channel.

Comparison between the plots of 3DS2, 3DS3 and 3DS4 from Fig.5.22 and Fig.5.15 shows that the RMS velocity fluctuations are highest everywhere in the case of 3DS4 having blockage ratio 32%. The peak intensity in 3DS3(24%) is comparable to 2DF2(32%) which demonstrates the remarkable effect of the staggered co-planar 3DS grid arrangement. The higher peak intensities displayed by 3DS3 and 3DS4 as compared to 2DF2 and 3DS2 is higher all across the yz-plane and it may be an indication of higher turbulence production. However the highest peak intensity in 2DF2 and 3DS2 was along the blue pencil, whereas in 3DS3 and 3DS4 it is along the magenta pencil which is close to the periodic wall of the channel. Otherwise the trends in the results

| (a) 3DS3 | (b) 3DS4 |
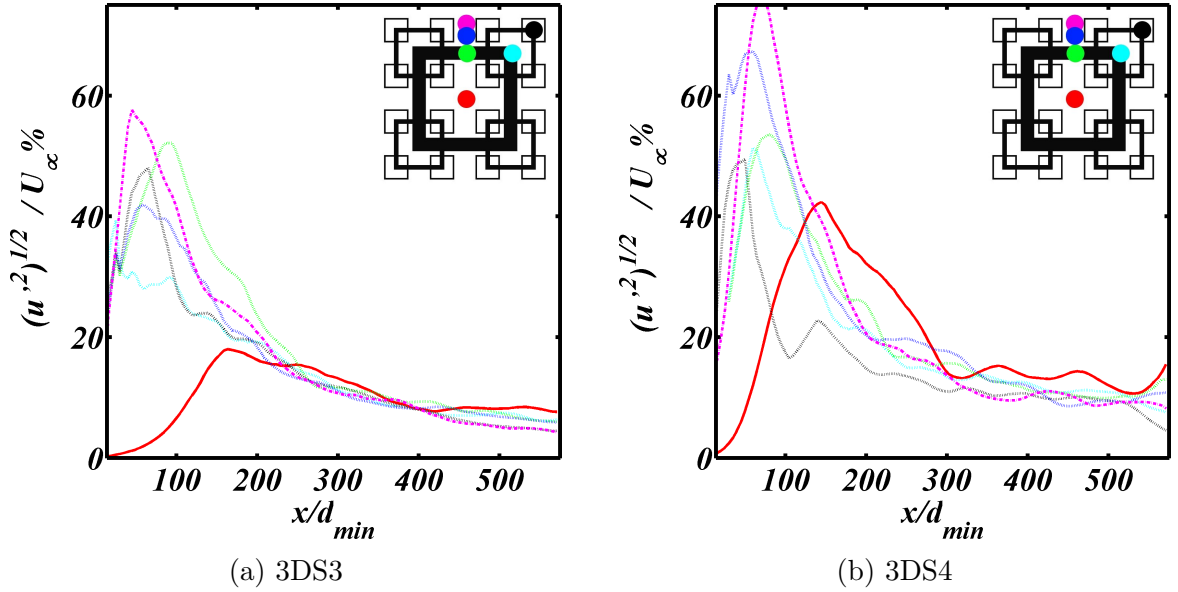
Figure 5.22: Root mean square velocity fluctuations along the channel length at different points on the grid. Each graph is colored according to the position of the pencil in the yz-plane as shown in the legend.

of 3DS3 and 3DS4 are qualitatively similar to the ones seen in 3DS2 and 2DF2. We observe three phases or regimes of flow. The first, in the near field production region from the position of the grid up to $x/d_{min} \approxeq 150$ where turbulence is being generated. Then the decay regime $150 \leq x/d_{min} \leq 300$ where the turbulence is dissipating along the centerline. Finally, in the far field, the slow dissipation region $x/d_{min} \geq 300$ where we see a very slow decay in intensity. We see some evidence of intensity rising again along the centerline in all cases except 2DF2 where the decay is more pronounced. It can be noticed that the location of peaks is similar in all 3DS cases which is probably due the position and arrangement of the frames $\{Z_0, Z_1, Z_2\}$ and which probably generates turbulent structures such as wakes and vortices of similar size and extent but different intensities.

The results indicate that that the maximum persistent turbulent fluctuation inten-

79

sity is along the centerline of the channel meaning that turbulence can be experienced most readily at the centerline. LV2012 [24] shows comparison of different blockage ratios of 2DF grids. We have compared 2DF2 from LV2012 with the 3DS3 grid but another interesting result in LV2012 is the grid 2DF(23%) which is comparable to the results from 3DS2(15%) although some of the peak intensity of 2DF(23%) is higher than 3DS2 but much lower than 3DS3 (which is comparable to 2DF2(32%)). The intensity is sustained most along the centerline where we see a peak at $x/d_{min} \cong 150$ and then the fast decay region up to $x/d_{min} \cong 300$, and then an oscillation region in the far field till the end of the channel. 3DS4 shows higher peaks sustained longer than 2DF2 and 3DS3 in all aspects. The significance of this result is that by adjusting the maximum blockage ratio $\sigma_{3DS}^{Max} = Max\{\sigma_0, \sigma_1, \sigma_2\}$ in the coplanar grid arrangement, we can improve control of the turbulence generated downstream of the channel in a 3DS grid channel configuration. Moreover, even with lower blockage ratios, we still obtain high peak intensity which could be advantageous in engineering applications.

Figs.5.24-5.28 show the mean velocity profiles and the rms turbulence intensity profiles along the y-axis (z=0) at different x-locations, for respectively the u-, v- and w- components of velocity, e.g $U(y)/U_\infty$ and $((u'(y))^2)1/2/U_\infty$ etc., from 3DS3 and 3DS4 grids. Figs.5.29-5.30 show the mean and rms concentration profiles along the centerline from the 3DS3 and 3DS4 grids.

The mean velocity profiles in Fig.5.23, 5.25 and 5.27 show similarity between 3DS2(15%) and 3DS3(24%) grid turbulence statistics, although the 3DS3 grid statistics posses higher mean velocity than 3DS2. Similarly Figs.5.24, 5.26 and 5.28 show higher rms fluctuations in velocity than 3DS2. The difference between rms velocity

(a) 3DS3   (b) 3DS4
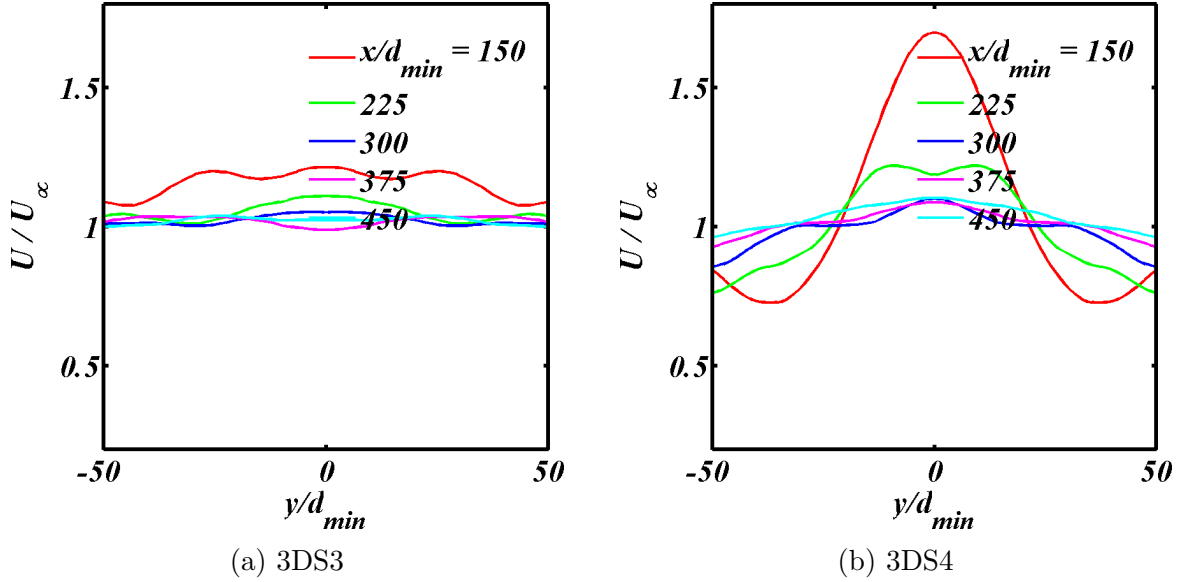
Figure 5.23: Mean x-velocity profile along y-axis at z = 0 , at five different locations in streamwise direction at $x/d_{min} = 150, 225, 300, 375, 450$.

fluctuations of 3DS2 and 3DS3 is around 15%.

There is similarity between turbulence characteristics of 3DS4 and 2DF2 grids which both posses the same blockage ratio (32%), but the levels in 3DS4 are much higher as compared to the levels in 2DF2. For example the central peak in Figs.5.23 and 5.4 shows that the in 3DS3 peak intensity is around $U/U_\infty \cong 1.7$ but in 2DF1 $U/U_\infty \cong 1.2$, and the rms turbulence intensities central plateau in Fig.5.5 for 2DF2 is around 25% where as for 3DS4 in Fig.5.24, it is around 42%. Furthermore the results from 2DF2 and 3DS4 show a pronounced higher velocity central region around the centerline -almost certainly due to the lack of obstacle in the central passage region in the grids. These grids show a jet-like structure due to the increased blockage (32%). The turbulence intensity profiles of each component of the velocity fluctuations in 3DS4 in the centerline region are close to 40% showing a remarkable degree of isotropy, even higher than 2DF1 where the component intensities differ from $\sim 17\%$ to $\sim 25\%$.

(a) 3DS3   (b) 3DS4
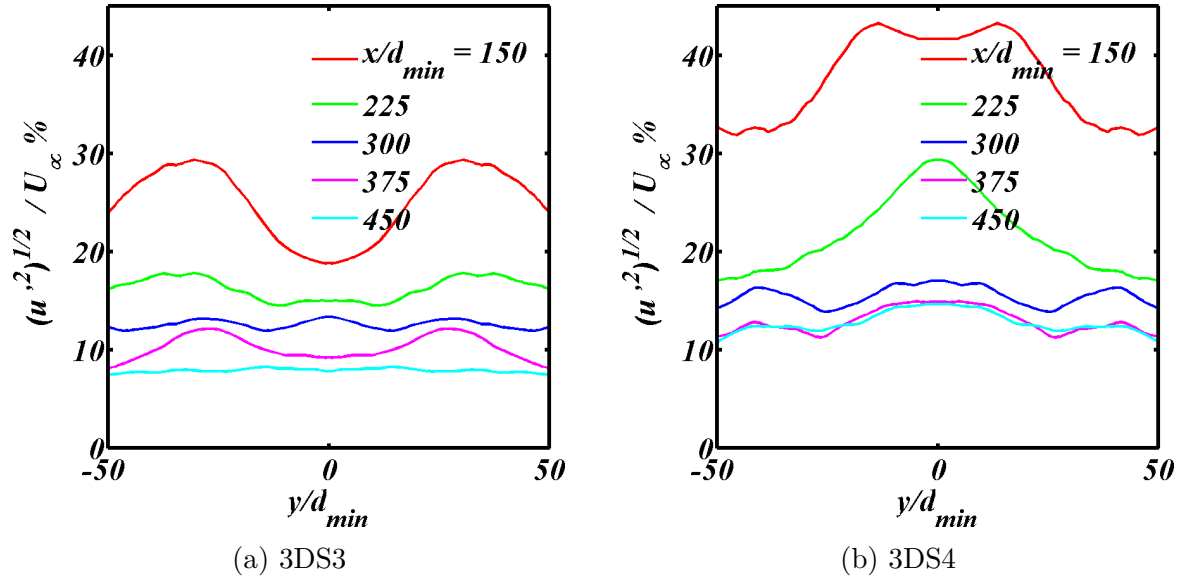
Figure 5.24: Root mean square of x-velocity fluctuations along y-axis at $z = 0$, at five different locations in streamwise direction at $x/d_{min} = 150, 225, 300, 375, 450$.

Further downstream, this isotropy is fairly well sustained in the far field even though the intensity level decays to around 12% and the central region expands across most of the lateral direction.

The sustaining of the turbulence intensity so far downstream, which is also isotropic, suggests that there must be a mechanism responsible for this. The only available mechanism is re-entrainment of turbulent fluid from outside of the central region into the central region. There will be evidence of this when we observe contour plots of the velocity field and scalar field later in this work.

The mean and rms fluctuations in the scalar fields show similar trends in all 2DF and 3DS cases except for 3DS4 in which the level of fluctuations in concentrations is a little higher throughout. This may be related to enhanced re-entrainment of scalars from surrounding fluid which sustains both concentration and velocity fluctuations alike. As such we cannot draw firm conclusions on which grid has better mixing

82

(a) 3DS3   (b) 3DS4
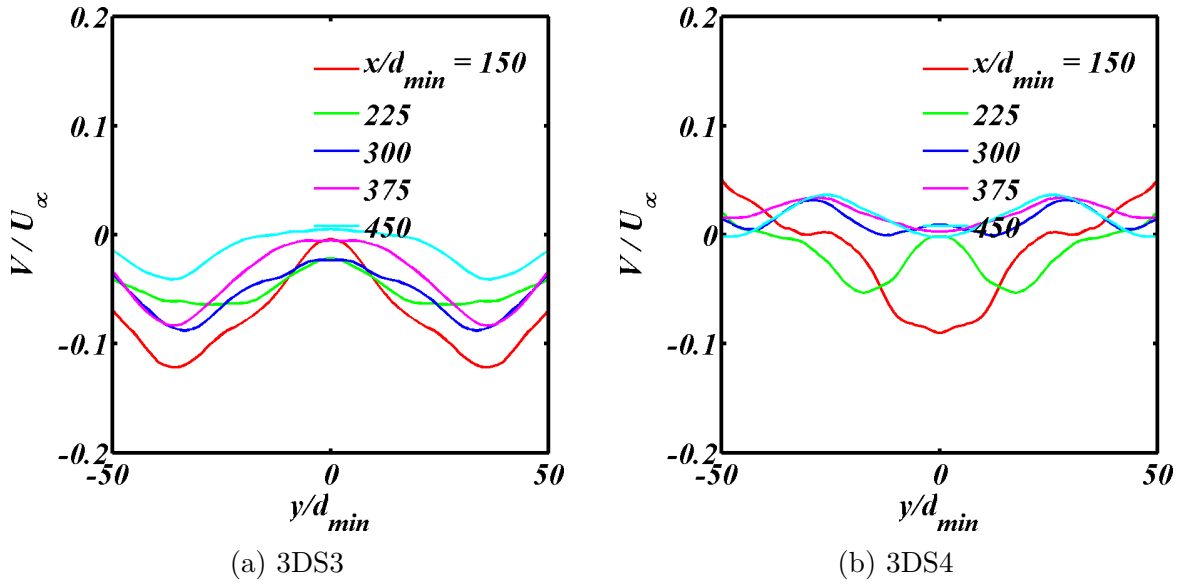
Figure 5.25: Mean y-velocity fluctuations along y-axis at z = 0, at five different locations in streamwise direction at $x/d_{min} = 150, 225, 300, 375, 450$.

(a) 3DS3   (b) 3DS4
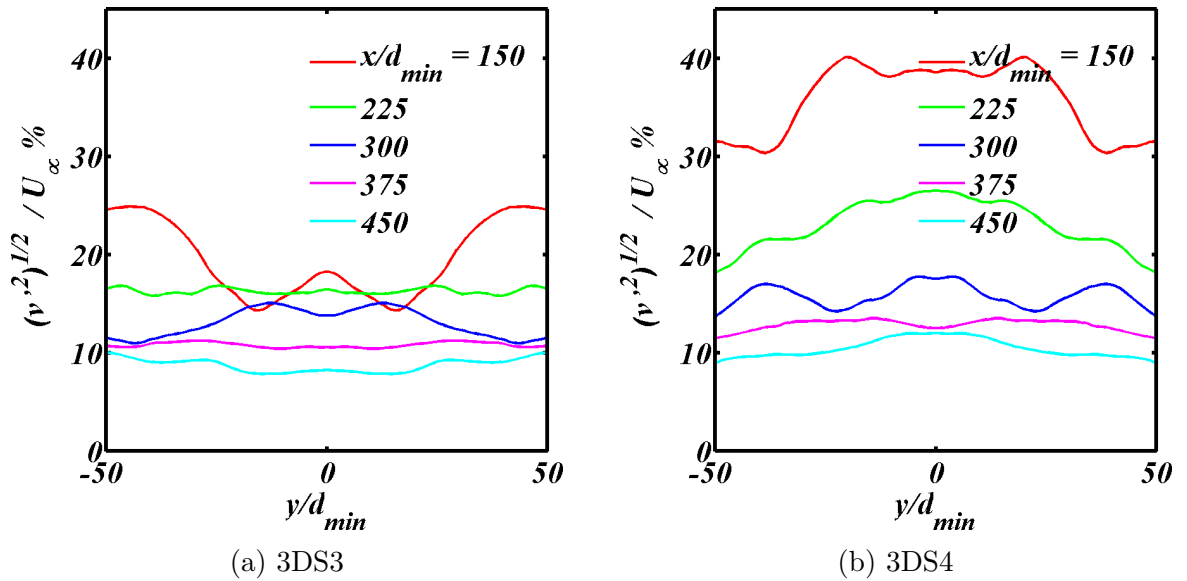
Figure 5.26: Root mean square of y-velocity fluctuations along y-axis at z = 0, at five different locations in streamwise direction at $x/d_{min} = 150, 225, 300, 375, 450$.

(a) 3DS3 (b) 3DS4
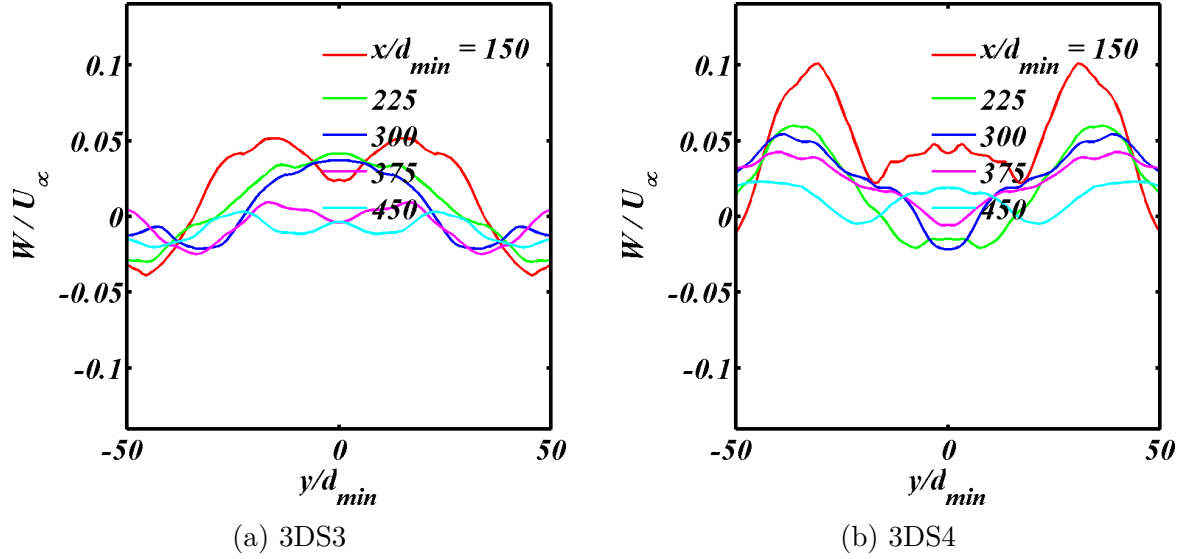
Figure 5.27: Mean z-velocity profile along y-axis at z = 0, at five different locations in streamwise direction at $x/d_{min} = 150, 225, 300, 375, 450$.

properties.

Fig.5.31 shows the RMS voriticity along the streamwise direction given by $(\omega'^2)^{1/2}$ where $\omega = \nabla \times \mathbf{u}'$. Fig.5.31a is from 3DS3 and Fig.5.31b is from 3DS4, we can compare these with the vorticity intensities from 2DF2 and 3DS2 in Fig.5.31. Unlike turbulence intensity, the RMS vorticity fluctuations do not vary a great deal basically 10-40%, even though the peak velocity intensities differ by much more -around 30-90% in Fig.5.22. However the x-locations of the peaks are the same as for the velocity peaks. After the peak vorticity intensity is attained, the decay is smooth and continuous till the end of the channel to low values of around 1-3%.

The figure 5.32 shows the energy density spectrum, obtained from the velocity time signals along the centerline, using Taylor's frozen turbulence hypothesis. The results are plotted in the form $\Phi_{uu}/U_\infty^2 d_{min}$, against $w d_{min}/U_\infty$ where w is the frequency. The figure 5.32 shows energy spectrums for 3DS3 and 3DS4 which are being compared to

(a) 3DS3   (b) 3DS4
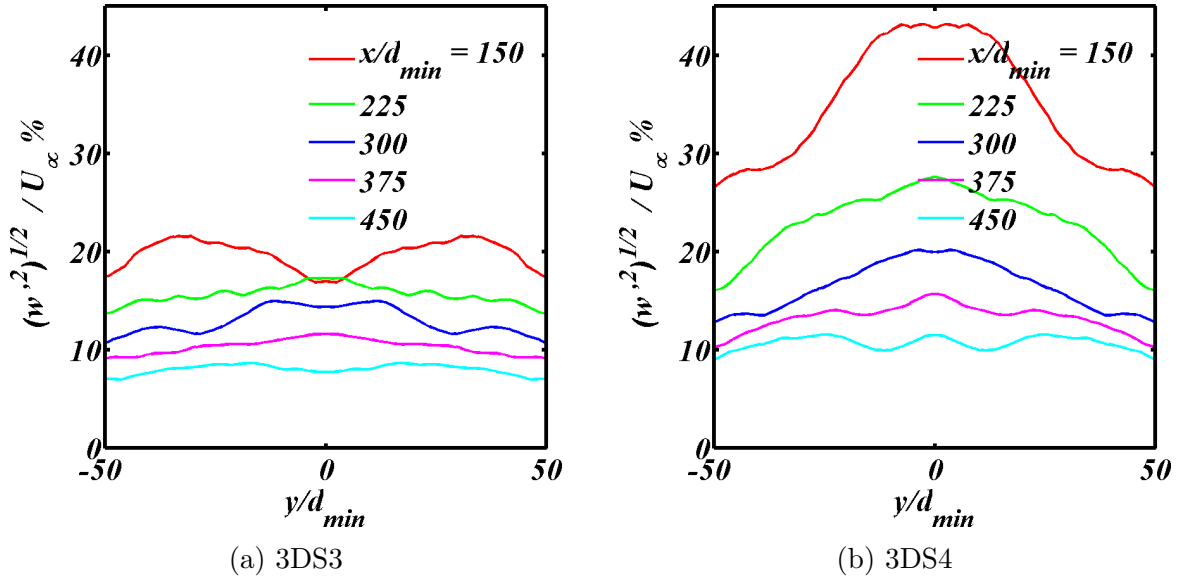
Figure 5.28: Root mean square of z-velocity fluctuations along y-axis at z = 0, at five different locations in streamwise direction at $x/d_{min} = 150, 225, 300, 375, 450$.

(a) 3DS3   (b) 3DS4
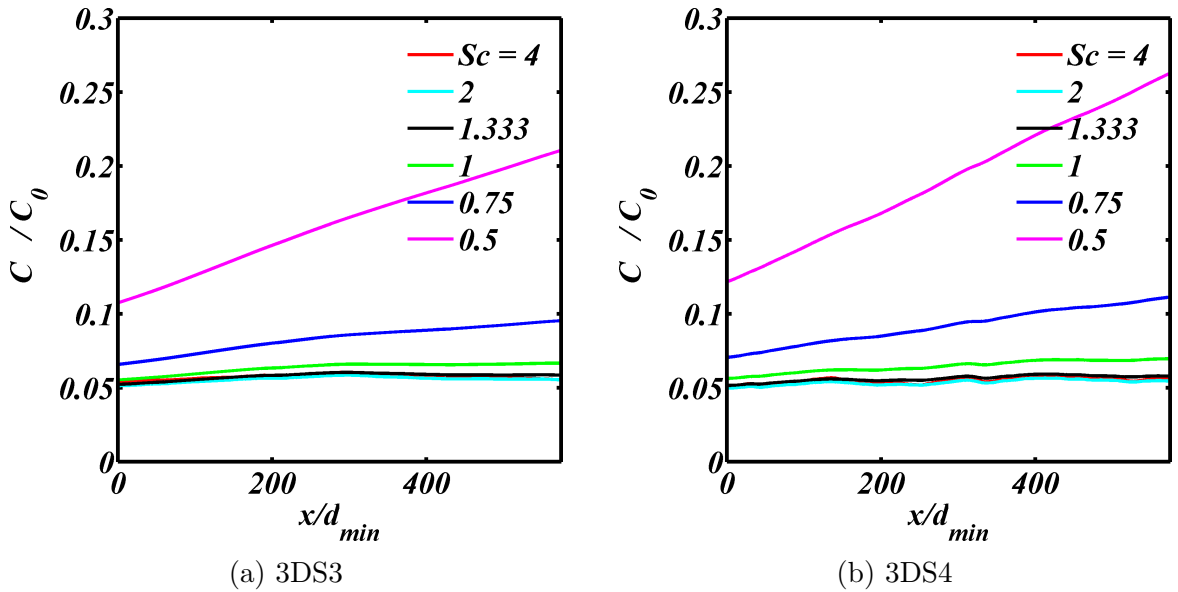
Figure 5.29: Mean scalar concentration graphs along the channel centerline with each color representing different Schmidt number Sc_t as given in the legend.

(a) 3DS3   (b) 3DS4
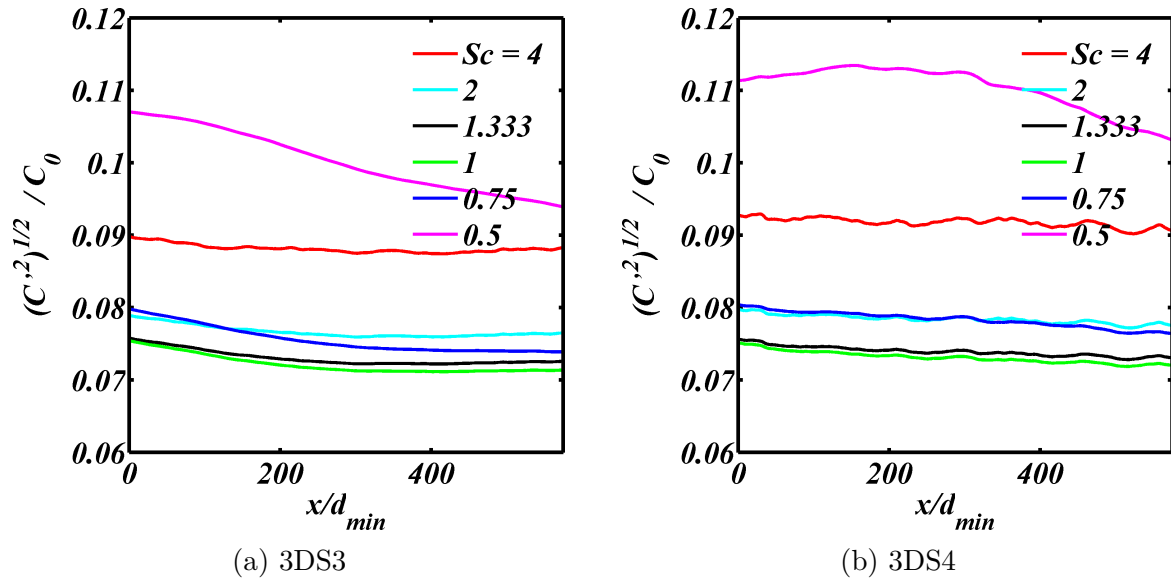
Figure 5.30: Root mean square of concentration fluctuation graphs along the channel centerline with each color representing different Schmidt numbers Sc_t as given in the legend.

(a) 3DS3   (b) 3DS4
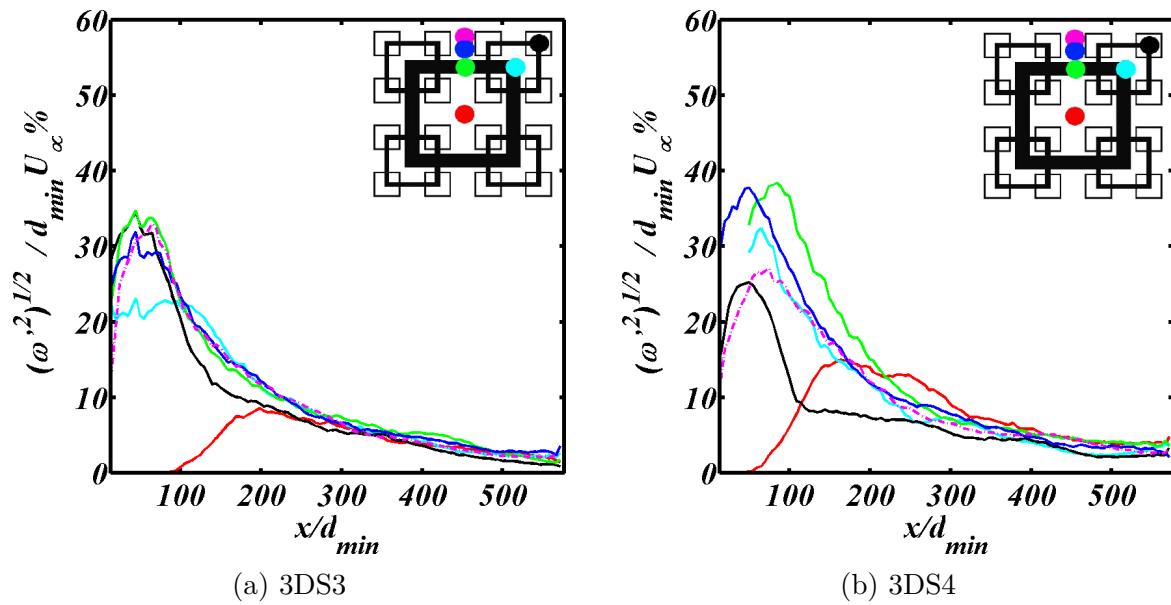
Figure 5.31: Vorticity profiles of four sparse multiscale grids along the streamwise direction in the flow. The legend shows location of pencils along the streamwise direction of the channel along which the vorticity is plotted.
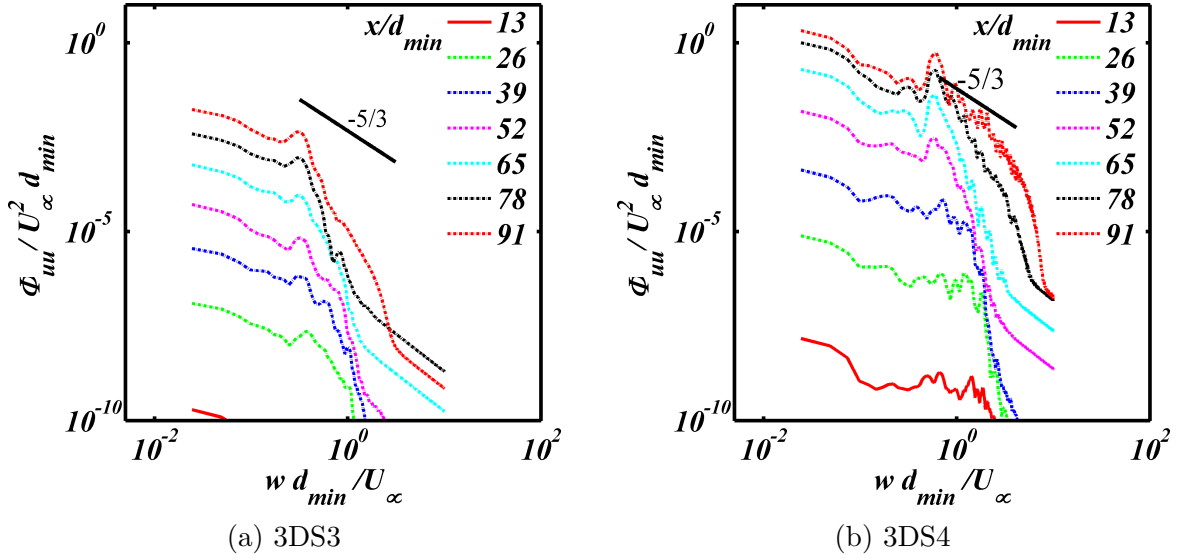
Figure 5.32: Frequency power spectrum of the sparse multiscale grids described in table 4.2 with probes recording velocity $u(t)$ at seven locations along the centerline of the channel where $x/d_{min} = 13, 26, 39, 52, 65, 78, 91$

.

2DF2 and 3DS2 from figures 5.10b and 5.10c. We compared our results of energy density with those of LV2011 with 2DF2(32%) and 2DF2(23%) and found that the 3DS3(24%) spectra sgiw fully developed turbulence $\sim K^{-5/3}$ over a short range at lower wavenumbers over about 1.5 decade. This develops early $2 \times 10^{-2} \lesseqqgtr w d_{min}/U_\infty \lesseqqgtr$ 0.8. There is a small peak at ~ 0.8 and at higher wave numbers the spectrum decays fast. In 2DF(23%) case the spectrum does not attain a fully developed turbulence $K^{-5/3}$. In 3DS4(32%) case and in 2DF1(32%) case we gave comparable fully developed turbulence spectra. However, 3DS4 attains this much faster than in 2DF1 case: from $x/d_{min} \approxeq 26$ in 3DS4 and $\approxeq 65$ in 2DF1 case, just under two decades. The presence of a small peak in the 3DS4 case might be due to the vorticity generated by the smallest frames of thickness $d_{min} = 1$.

(a) 3DS5   (b) 3DS6
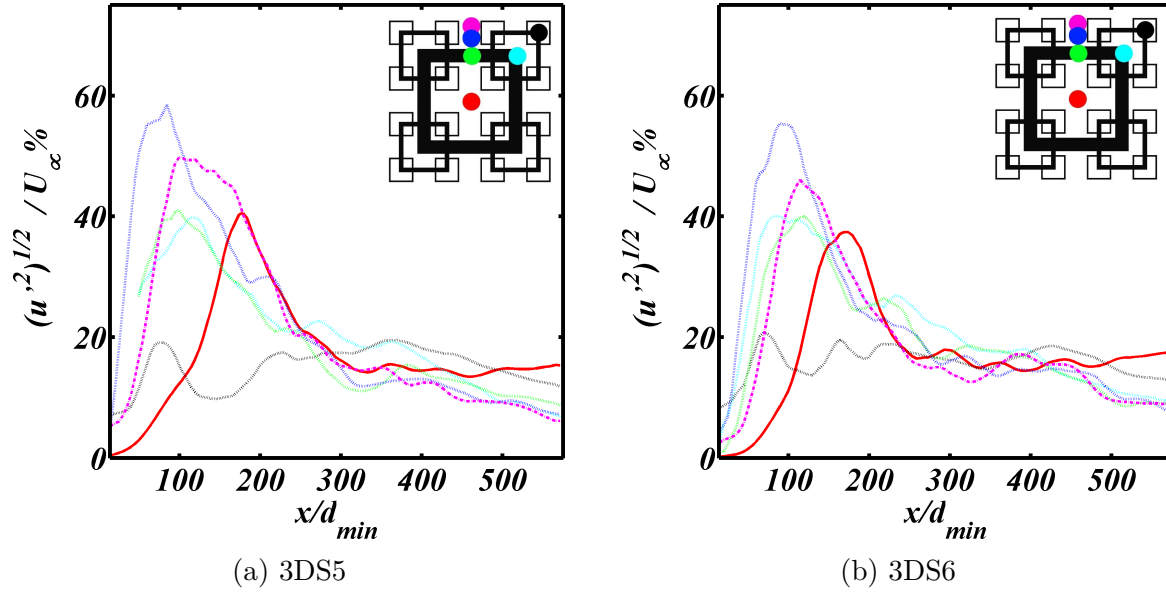
Figure 5.33: Root mean square velocity fluctuations along the channel length at different points on the grid. Each graph is colored according to the position of the pencil in the yz-plane as shown in the legend.

5.4 Comparison 3DS4, 3DS5 and 3DS6

In this section the new 3DS grids are compared in terms of different parameters a channel of dimensions $L_y = L_z = 115.2d_{min}$ and $L_x = 576d_{min}$. The maximum blockage ratios $\sigma_{3DS}^{Max} = 32\%$ for 3DS4, 3DS5 and 3DS6. The difference between 3DS4, 3DS5 and 3DS6 is the order in which the blockages are placed as evident from the Table4.2. The main purpose of this study is to see the effect of changes in order of co-frame arrangement on the flow characteristics such as intensity, vorticity, concentration and mean velocity.

Fig.5.33 shows the rms turbulence intensity of the streamwise velocity component along pencils parallel to the centerline, similar to the previous cases. Cases from 3DS5 and 3DS6 are shown here. 3DS4, 3DS5 and 3DS6 are re-arrangements of the co-frames $\{Z_0, Z_1, Z_2\}$.

3DS4: $[x_0, x_1, x_2] = [Z_0, Z_1, Z_2]$

3DS5: $[x_0, x_1, x_2] = [Z_2, Z_0, Z_1]$

3DS6: $[x_0, x_1, x_2] = [Z_1, Z_2, Z_0]$

Thus in 3DS6, the largest scale Z_0 is the third frame downstream, $x_2 = Z_0$. All three of the 32% 3DS grids above produce peak intensities which are generally higher than from the 32% 2DF2 grid. The 3DS4 produces the highest peaks of any grid examined here. The location of the peaks shifts slightly downstream from 3DS4 to 3DS5 to 3DS6 -almost certainly due to the shift in Z_0 downstream which indicates that the peak location is governed by the location of Z_0 of the largest fractal scale. This in turn suggests that the peaks are a manifestation of flow structure (jet, wake, vortex) of characteristic size.

The purple line close to the domain periodic boundary, shows the highest peak in 3DS4. Overall, it is important to note that nearly all the three 32% 3DS grids show higher peaks than 2DF indicating higher turbulence energy in the entire cross-sectional plane. There are fine differences between the 3DS4, 3DS5 and 3DS6 grids but it is clear overall that the staggered co-planar arrangement of the grids produces significantly different characteristics to 2DF2 with generally higher peaks in intensity. Furthermore, the level of turbulence intensity is sustained generally at higher level further downstream than in 2DF2. Fig.5.34 shows the centerline mean and rms turbulence intensity from 3DS5 and 3DS6. Here the far field intensity seams to be actually increasing downstream in the far field. This is something new which has not been previously observed in any grid system. The question is what mechanism causes the turbulence intensity to rise downstream of the channel along the centerline?
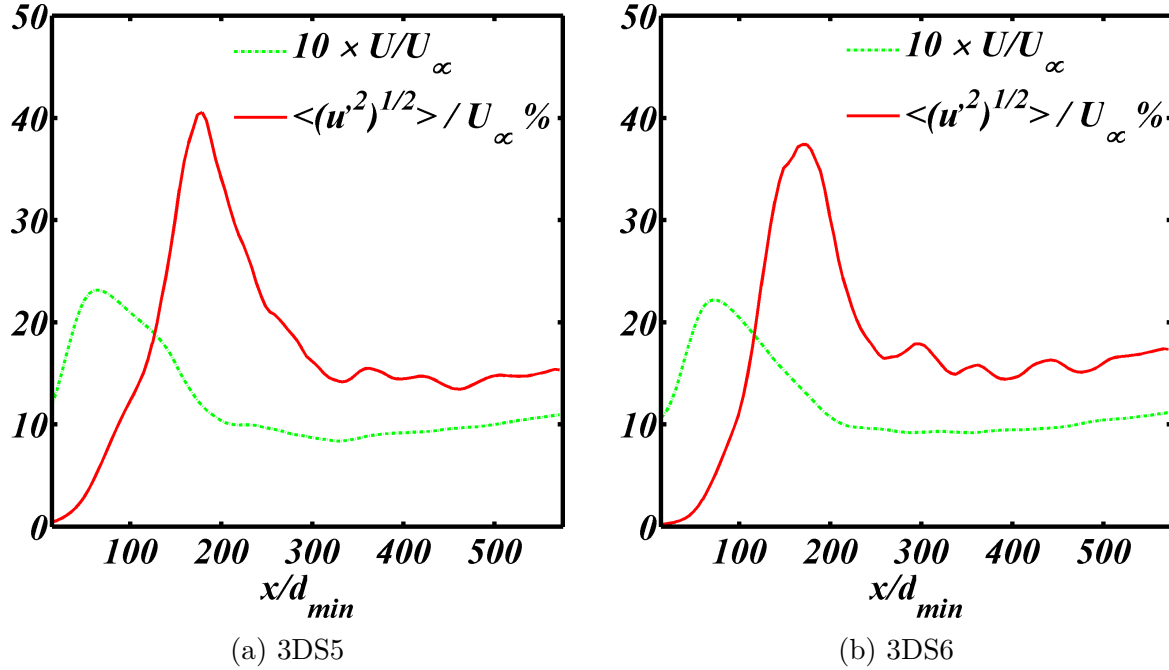
Figure 5.34: Root mean square velocity fluctuations along the channel length at different points on the grid. Each graph is colored according to the position of the pencil in the yz-plane as shown in the legend.

In the absence of any source of turbulence generation, the only mechanism must be re-entrainment of turbulent fluid from outside of the central region towards the central region. There is evidence of this from the contour plots of velocity and scalar, to be presented later.

Compared to the fractal grid of the same blockage ratio, the 3DS4, 3DS5 and 3DS6 display much higher turbulence intensity and it is sustained longer downstream along the centerline as displayed by the red curves in figure 5.33. The peak is reached at around $x/d_{min} = 150$ in all four cases which is interesting considering the different order of arrangements of the grids. However 3DS4 shows a higher average intensity in streamwise direction which is understandable as in 3DS4, the blockages are placed in order of descending blocakge ratios of the fractal iterations in agreement with the

theory of energy cascade. 3DS4 shows a higher intensity even along other pencils in the channel. In 3DS5 and 3DS6, the peak is shifted slightly downstream as compared to 3DS3 and 3DS4. The reason is because the main contribution to the intensity seems to be coming from the thickest grid iteration. However the peak does not seem to be based on the blockage ratio of the grids as for grid with blockage ratio 24%, the peak intensity lies at around 20, where as for other grids it rises to about 40. In fractal square grid 2DF2, the blockage ratio was 32% and the peak intensity was around 25. This difference in peak intensity by 3DS grids is a significant deviation.

Figure 5.34 shows percentage root mean square velocity along the centerline of the channel in red and mean velocity profile in green multiplied by a factor of 10. Mean velocity is also significantly higher in case of grids having blockage ratio 32%. The average velocity sustains longer down the channel in 3DS4, 3DS5 and 3DS6 and becomes constant after $x/d_{min} = 300$. We donot see a fall in the average or root mean square velocity profiles which means that turbulence is sustained all the way down the channel. For a powerlaw decay defined by

$$\frac{u'^2}{U_\infty} = c \left(\frac{x}{d_{min}} \right)^{-n} \tag{5.2}$$

the value of n is highest for 3DS6 in the decay region $n \cong 0.3$ and smallest in the decay region of 3DS3 $n \cong 0.05$. The decay region is always in the range $80 \leq x/d_{min} \leq 250$ -this strongly suggests that a local flow structure, such as a jet or wake or vortex has formed which depends only upon the grid size. Therefore the rate of decay is higher in grids having higher blockage ratio as previously observed by Laizet and Vassilicos

(a) 3DS5 (b) 3DS6
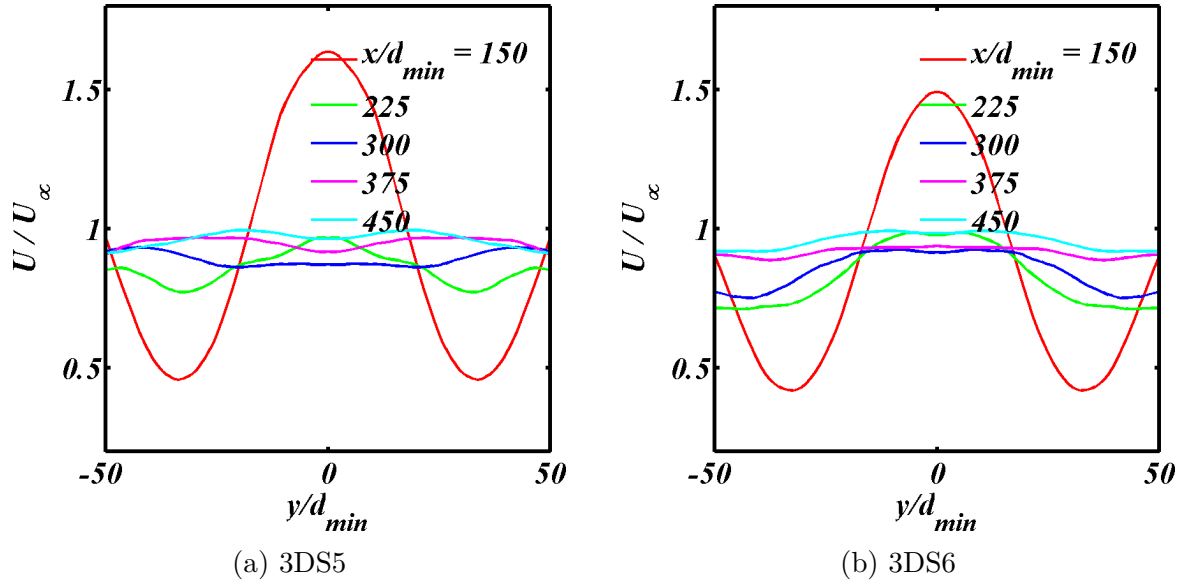
Figure 5.35: Mean x-velocity profile along y-axis at z = 0 , at five different locations in streamwise direction at $x/d_{min} = 150, 225, 300, 375, 450$.

in [23], [10], [13].

Mean streamwise velocity component profile along spanwise direction in the channel along pencils at $x/d_{min} = 150, 225, 300, 375$ and 450 are shown in figure 5.35. The lateral profiles of velocity field components at different x-locations along the channel are shown in Figs.5.34-5.40. The mean and rms turbulence profiles can be seen in these images at locations as in the previous cases.

The near field profile, the red lines, clearly show the sinosidal-like variation which is a signature of the grid close to the grid. Further downstream, all the mean and rms profiles follow trends similar to those observed in 3DS3 and 3DS4. It is important to note that an approximate isotropy is observed in the turbulence intensity from all the 3DS grids. These results indicate that although there are differences in the details of the turbulence characteristics, the mechanism of turbulence generation, decay in the near-field, and turbulence sustenance in the far field downstream are broadly similar.

(a) 3DS5	(b) 3DS6
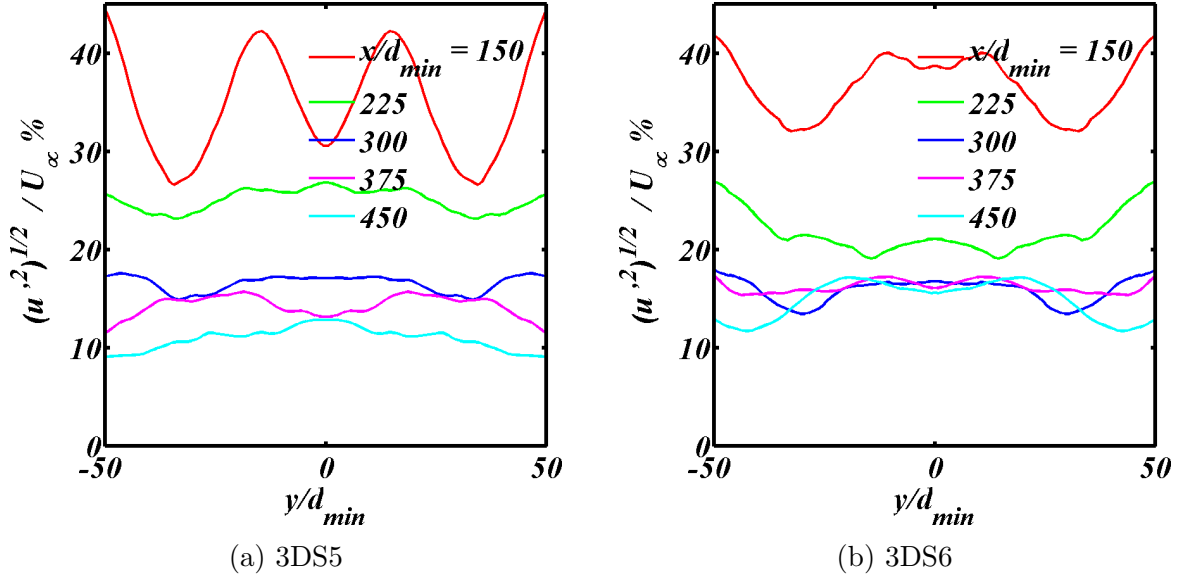
Figure 5.36: Root mean square of x-velocity fluctuations along y-axis at z = 0, at five different locations in streamwise direction at $x/d_{min} = 150, 225, 300, 375, 450$.

The main difference appears to be the level of turbulence generated and sustained.

Figure 5.36 shows the root mean square fluctuation counterpart of 5.35. RMS velocity fluctuations display a similar wave pattern in all the grids. The velocity fluctuations peak away from the center and die down further downstream of the channel and follow a self-similar pattern in general.

Figure 5.37 shows radial mean velocity profile in spanwise direction of the channel at five different locations downstream of the grid. Unlike mean streamwise velocity component, the radial mean velocity components are highly effected by the order of grid arrangement in the channel. Velocity fluctuates around zero in all four grids but consistently remains negative except in the grid where thickest fractal iteration is placed farthest downstream. In 3DS6 radial velocity component is either positive or a small negative number near the center. This is interesting because a slight change in the order of the grid arrangement can alter flow characteristics quite significantly.

93

(a) 3DS5   (b) 3DS6
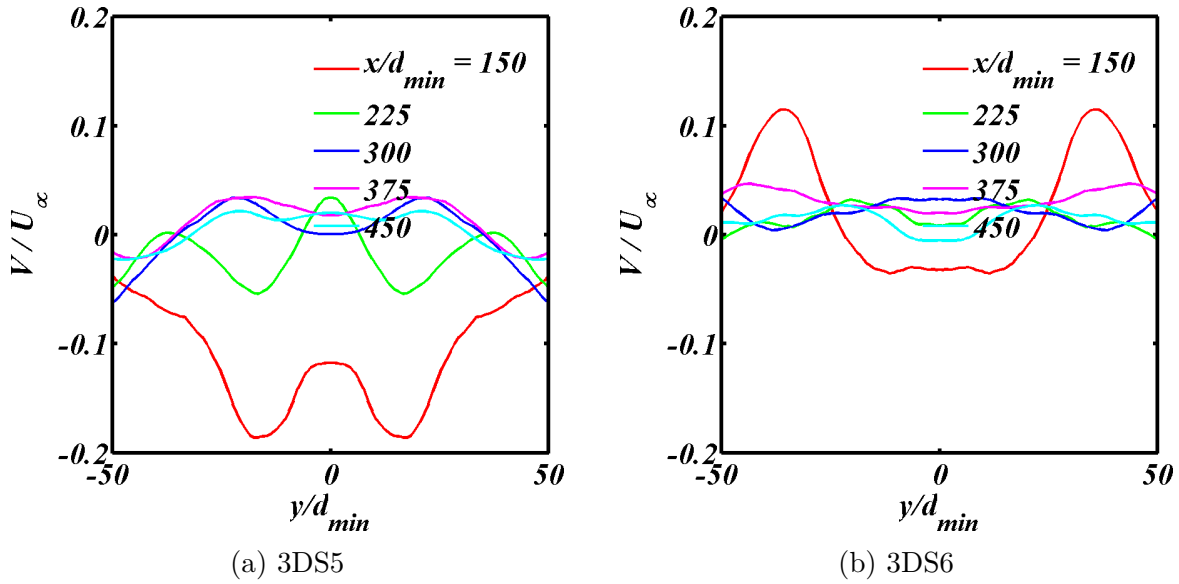
Figure 5.37: Mean y-velocity fluctuations along y-axis at z = 0, at five different locations in streamwise direction at $x/d_{min} = 150, 225, 300, 375, 450$.

(a) 3DS5   (b) 3DS6
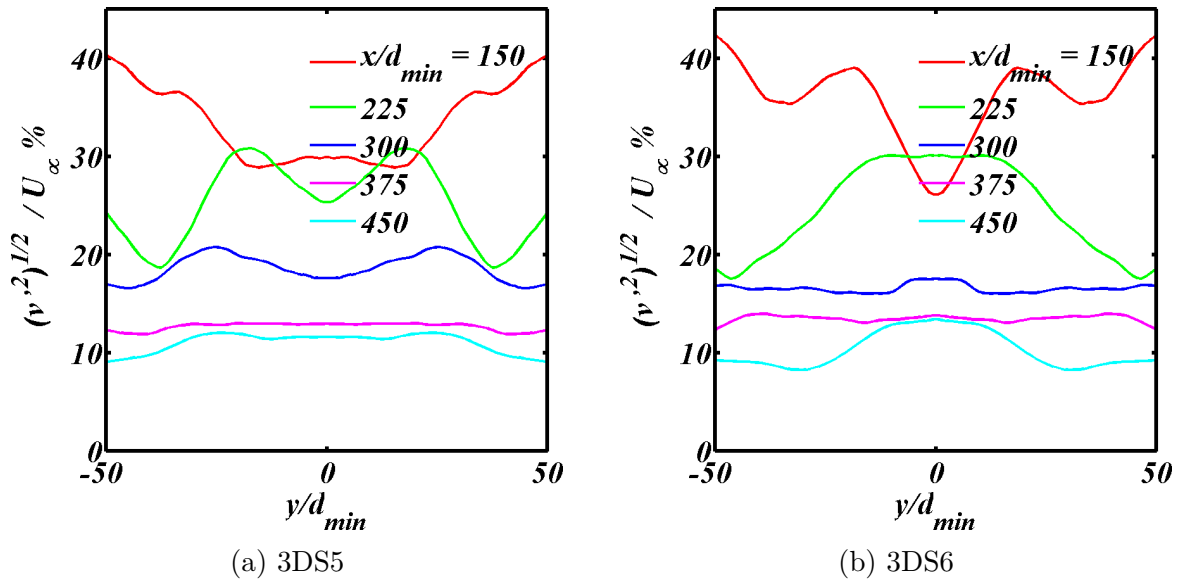
Figure 5.38: Root mean square of y-velocity fluctuations along y-axis at z = 0, at five different locations in streamwise direction at $x/d_{min} = 150, 225, 300, 375, 450$.

$$(a) \; 3DS5 \qquad\qquad (b) \; 3DS6$$
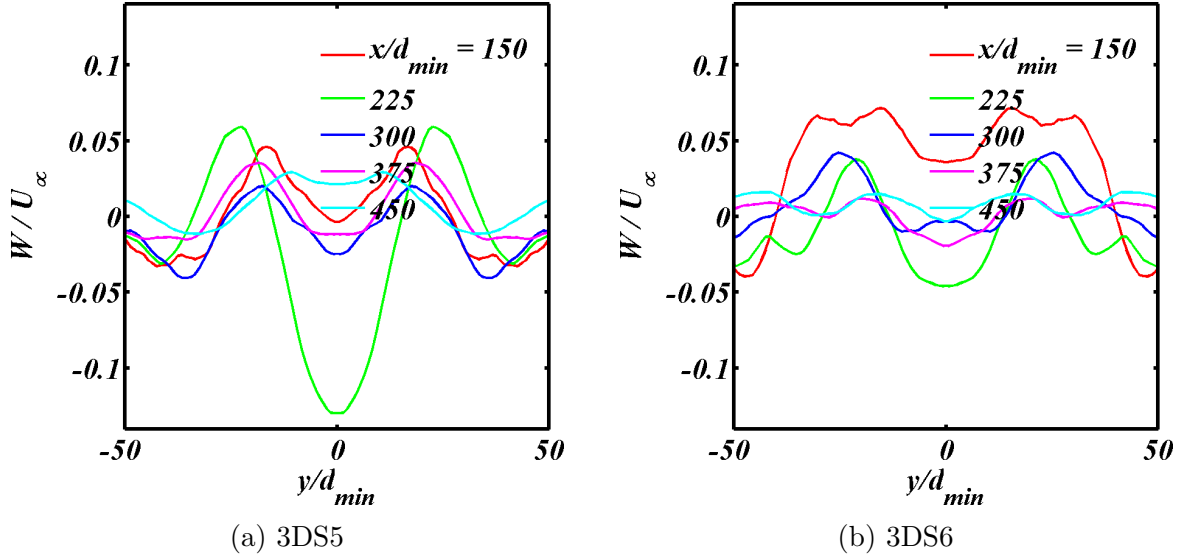
Figure 5.39: Mean z-velocity profile along y-axis at z = 0, at five different locations in streamwise direction at $x/d_{min} = 150, 225, 300, 375, 450$.

Figure 5.38 shows RMS fluctuation of y-component of velocity. In 3DS4 the fluctuations lie between 10 and 30 just like their x-component fluctuation counterpart in figure 5.36. Overall the value of the isotropy indicator is greater than 1 in all grids which is also the case with fractal grids [24].

Mean z-velocity components shown in figure 5.39 are mostly positive as opposed to y-velocity mean which were negative mostly.

The RMS fluctuations of the z-velocity component in figure 5.40 have similar profile as that of y-velocity fluctuations in 5.38 representing the symmetry of the flow.

Figure 5.41 shows the log-log turbulence power spectrum [5] showing how energy cascades down to the smallest scales. Only the production region of the channel is considered $x/d_{min} = 13, ..., 91$ along the centerline of the channel. Three sizes of eddies are produced due to the grids and their interactions reveal three distinct regimes of energy.Inertial subrange is visible in 3DS4 and 3DS6 where $E(K) \sim K^{-5/3}$ law is

(a) 3DS5   (b) 3DS6
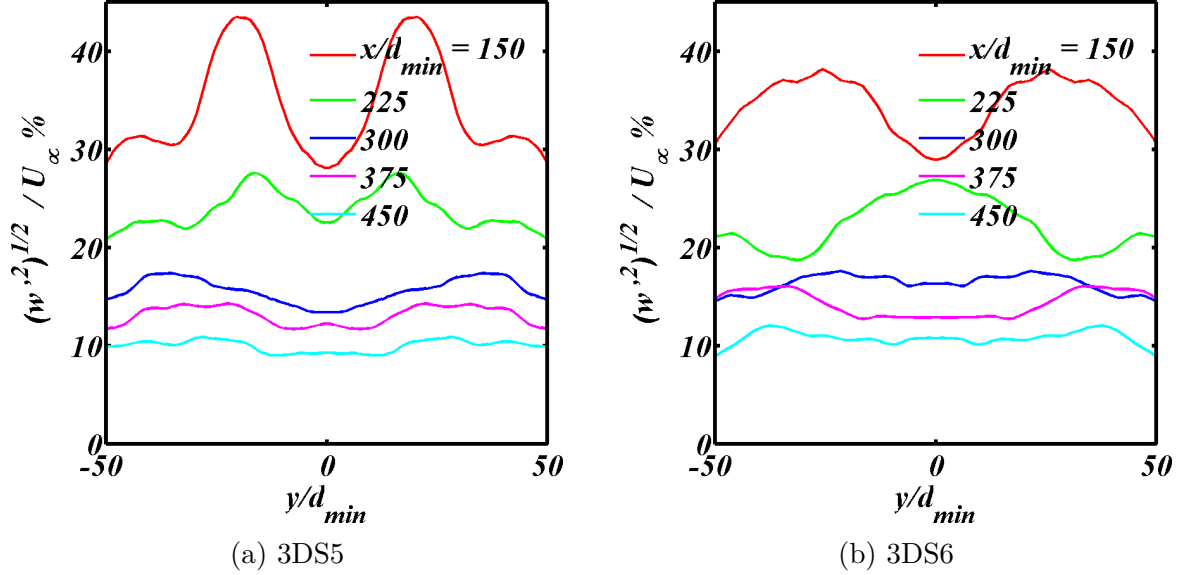
Figure 5.40: Root mean square of z-velocity fluctuations along y-axis at z = 0, at five different locations in streamwise direction at $x/d_{min} = 150, 225, 300, 375, 450$.

(a) 3DS5   (b) 3DS6
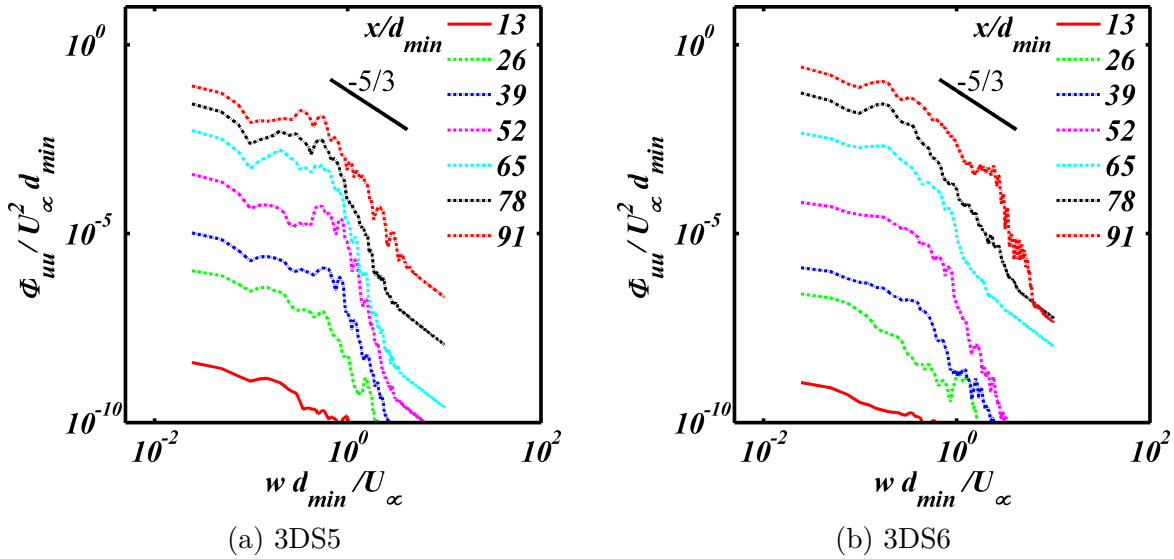
Figure 5.41: Frequency power spectrum of the sparse multiscale grids of case 3 described in table 4.2 with probes recording velocity $u(t)$ at seven locations along the centerline of the channel where $x/d_{min} = 13, 26, 39, 52, 65, 78, 91$

.

(a) 3DS5

(b) 3DS6
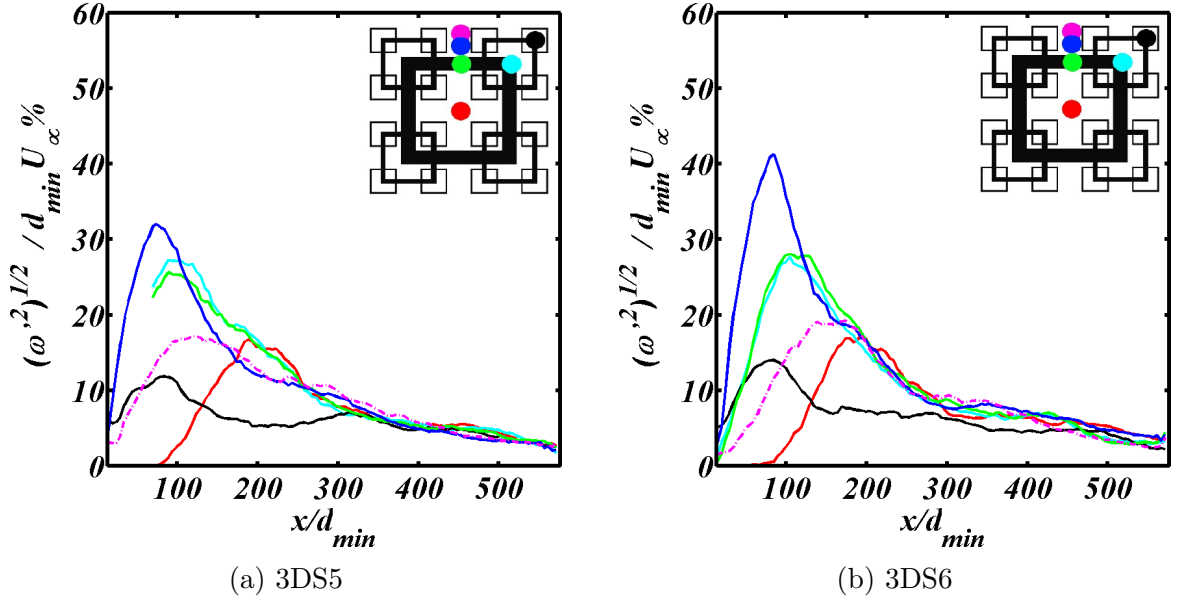
Figure 5.42: Vorticity profiles of four sparse multiscale grids along the streamwise direction in the flow. The legend shows location of pencils along the streamwise direction of the channel along which the vorticity is plotted.

established. This is interesting because these three grids have blockage ratio of 32%, thus indicating that a fully developed $K^{-5/3}$ spectrum may be governed principally by σ_{3DS}^{Max}. All grids show that spectrum falls around the frequency $wd_{min}/U_\infty = 0.8$ which must be close to the Kolmogorov scale η and which corresponds to the smallest thickness in the grid system $d_{min} = 1$.

Figure 5.42 shows the rms turbulence vorticity fluctuation from 3DS5 and 3DS6. Peak in vorticity intensity is observed around $200x/d_{min}$ and a decay in vorticity fluctuation is observed from this point onwards. Vorticity intensity is much higher in the regions away from the centerline of the channel and reaches its peak closer to the grid. Otherwise the vorticity profiles from 3DS5 and 3DS6 differ a great deal from 3DS4 qualitatively or quantitatively. This indicates that the vorticity generation may not be the critical mechanism in these grid systems and it is relatively unaffected by
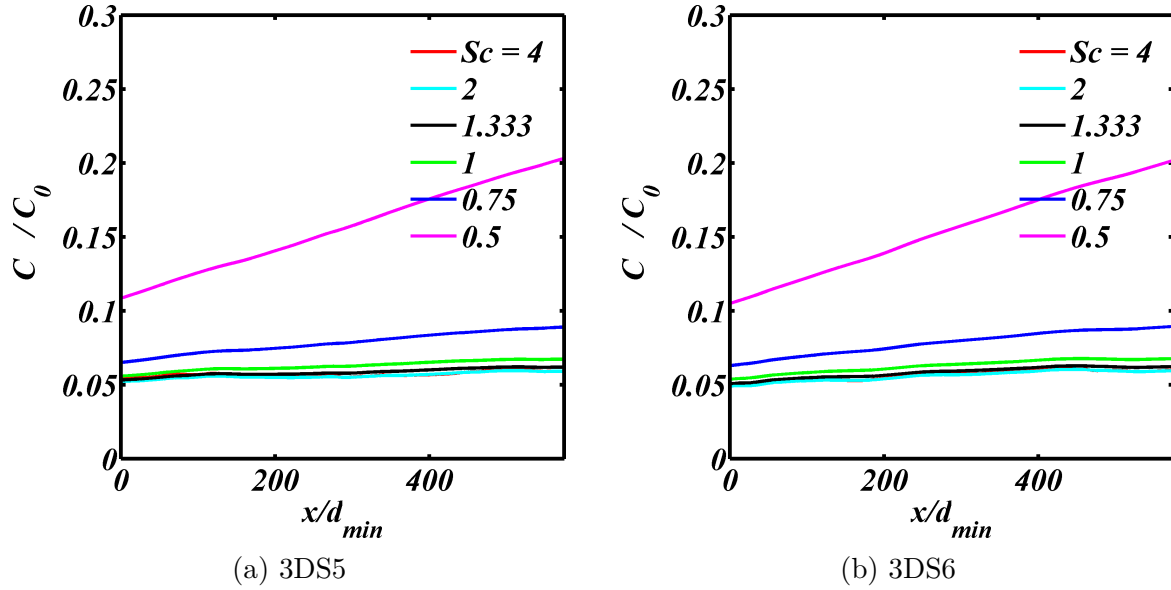
Figure 5.43: Mean scalar concentration graphs along the channel centerline with each color representing different Schmidt numbers as given in the legend.

the grid arrangements as the plots suggest.

Fig.5.43 shows mean scalar concentration profile along the centerline for different schmidt numbers as in previous cases $0.5 \leq Sc \leq 4$. Fig.5.45 shows rms fluctuation profile of scalar concentration along the centerline from 3DS5 and 3DS6. These trends are broadly similar to those in 3DS2, 3DS3 and 3DS4. There may not be much difference in the mixing of scalars in the far field but in the near and intermediate fields, there are fine observable differences between the different grids.

In the Fig.5.44, contour plots of the scalar fields in the yz-plane are shown. For higher schmidt numbers $Sc \geq 1$, the scalar fields look similar. For $Sc \leq 1$ (large diffusivity) the scalar diffuses rapidly downstream and laterally.

Figure 5.45 shows the streamwise variation of the intensity of concentration fluctuations along the centerline of the four sparse grids. For lower diffusion coefficients, the concentration fluctuations have a low peak around $150x/d_{min}$ which is in line with
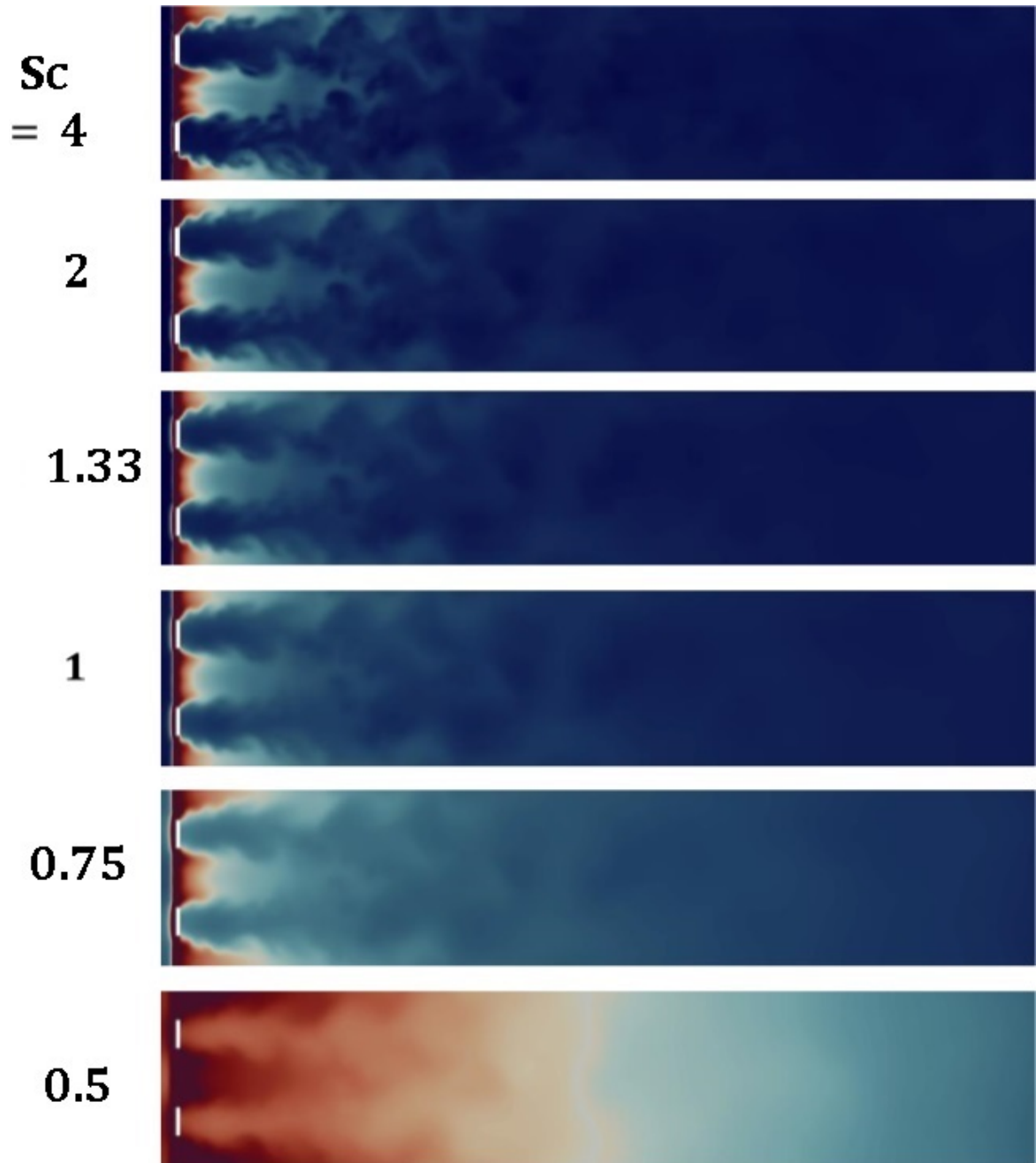
Figure 5.44: Instantaneous passive scalar diffusion profile showing transport of the normalized scalar at time $500T$ with red color indicating concentration of 0 and red color indicating concentration of 0.5 for different values of the Schmidt number Sc in the grid 3DS4 in the xz-plane at y=0.

the peak velocity fluctuations of these grids as seen in 5.34. Higher value of diffusivity represents higher flux and the concentration intensity increases with the rise in mass flux in grid generated turbulence [34], [35].

(a) 3DS5　　　　　　　　　　(b) 3DS6
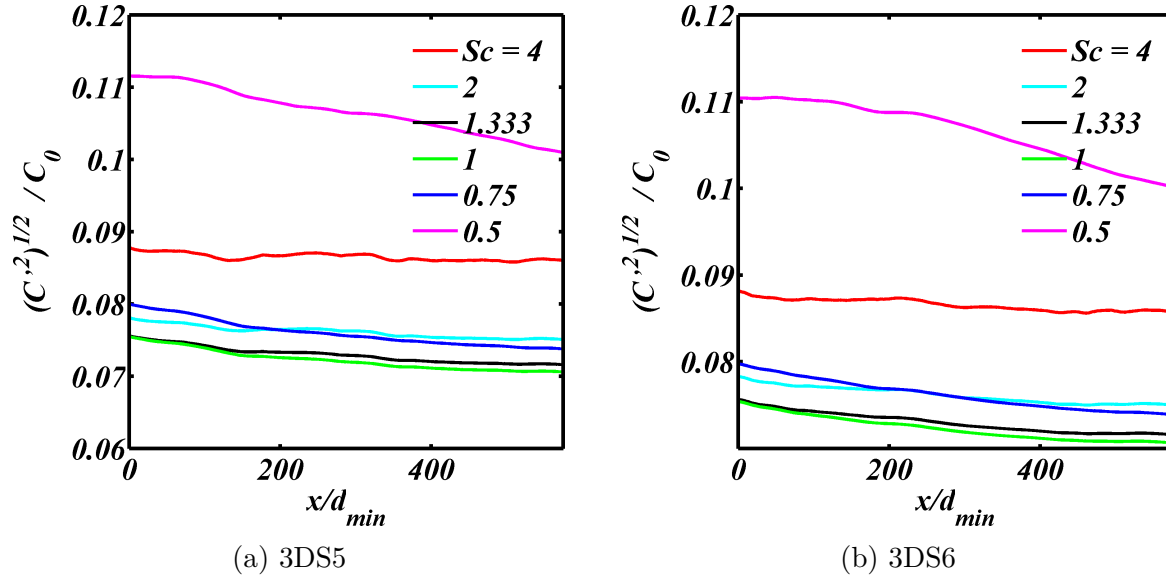
Figure 5.45: Root mean square of concentration fluctuation graphs along the channel centerline with each color representing different Schmidt numbers Sc as given in the legend.

5.5　Discussion

We have investigated turbulence generated by a new type of grid, the three-dimensional sparse multi-scale grid turbulence generator which we refer to as 3DS for short. To our knowledge this is the first study of its kind on 3DS generated turbulence. The investigation was carried out numerically using Direct Numerical Simulations (DNS) which resolves the complete Navier-Stokes equations (NSE) for incompressible flow down to the finest grid imposed on the system. Details of the DNS used here was set out in Chapter 4. Previous studies of flat fractal grids, such as the 2DF in LV2012 show that some flat fractal grids effect turbulence differently as compared to classical regular grids. The main idea behind the flat fractal grids is that multiple turbulence length scales are excited initially simultaneously and in one plane, as opposed to classical grid turbulence which generates turbulence through an

energy cascade forced typically at a single scale, the mesh size M.

The new 3DS grid, due to Malik [27], goes further than the 2DF system by staggering the different length scales in to different grids, or co-frames, in an overall co-planar arrangement, see Fig.5.1. In this manner the generation of different turbulence scales is not limited to a single plane and so provides more flexibility to the system.

An immediate effect of the co-planar 3DS system is that the maximum blockage ratio, or solidity, of the 3DS grid system is greatly reduced as compared to the 2DF flat fractal grid counterpart from which it was obtained. In a three frame 3DS system, for example, the maximum blockage ratio is, $\sigma_{3DS} = Max\{\sigma_0, \sigma_1, \sigma_2\}$, but because $\sigma_{2DF} = \sigma_0 + \sigma_1 + \sigma_2$, then $\sigma_{3DS} << \sigma_{2DF}$. For example, in the 2DF square fractal grid that LV2012 investigated, we have $\sigma_{2DF} \approx 32\%$, and in the counterpart 3DS grid we have $\sigma_{3DS}^{Max} \approx 15\%$. The reduction in maximum blockage ratio is bound to affect the turbulence generated downstream of the grid, and it is a part of the aim of this work to investigate this feature.

Furthermore, the 3DS system has a much greater parameter space than the 2DF or RG systems, because there are several new parameters in the 3DS system. First, there is the inter-frame spacing between successive co-frames, $r_1 = x_1 - x_0, r_2 = x_2 - x_1$.

Second, the co-frame set $\{Z_0, Z_1, Z_2\}$ possesses the blockage ratio set $\{\sigma_0, \sigma_1, \sigma_2\}$; so long as one of the σ_i's is equal to σ_{3DS}^{Max}, say σ_0, then the other two can take arbitrary values less than or equal to σ_{3DS}^{max}, and this provides, potentially, an infinite number of 3DS systems for the same σ_{3DS}^{max}.

Thirdly, for each choice of the co-frame set $\{Z_0, Z_1, Z_2\}$, you can arrange the co-frames in any order to obtain a new 3DS system. For example, swapping the first and

second frames, we obtain $\{Z_1, Z_0, Z_2\}$, with the blockage ratio set $\{\sigma_1, \sigma_0, \sigma_2\}$. In the a 3-frame system there are 3! possible arrangements.

At the current time, the choice of these parameters is somewhat ad hoc because no previous study exists on the 3DS system. For this study, we have chosen parameters values on an approximate physical basis. Thus, the inter-frame distances r_1 and r_2 were chosen to be approximately where we except that the wakes from the upstream grid would intersect. The ordering of the co-frame set $\{Z_0, Z_1, Z_2\}$ was chosen to be the largest scale first Z_0, then the next scale in Z_1, and the smallest scale was in Z_2. The initial blockage ratio set $\{\sigma_0, \sigma_1, \sigma_2\} = \{15\%, 15\%, 15\%\}$ was then obtained directly from the 2DF flat fractal after separating each scale.

The main aim of this study is to begin an investigation of the turbulence generated by the different 3DS grids. Key questions are, how does the turbulence compare to the 2DF system? How do the different parameters affect the turbulence generated? In this study we have investigated these issues through examining the statistics of the generated turbulence, and through contour visualizations of the velocity fields and diffusing scalar fields.

However, using DNS as the numerical method of investigation we cannot investigate the full range of parameters, or even all the new parameters, because the DNS is time consuming. In this study we have therefore limited the calculations to a select number of cases. This has given us an overall view of the sensitivity to some of the parameters, although of course more of the parameter ranges will eventually have to be carried out in the future.

Here, we have opted to investigate only the variation of the blockage ratio set

102

$\{\sigma_0, \sigma_1, \sigma_2\}$, and the order of the co-frames $\{Z_0, Z_1, Z_2\}$. Changes in the inter-frame separations have been left for future studies. In all the 3DS grids simulated here, we have kept $r_1 = 17 d_{min}$ And $r_2 = 8.5 d_{min}$.

LV2012 was chosen as the base case for our initial system, because LV2012 investigated the RG and 2DF through turbulence statistics in a $4 : 1 : 1$ channel with inflow and outflow conditions and periodic wall conditions. Initially, we used this exact system as a comparator, and we simulated the RG1, 2DF1 and the 3DS1 grids in this channel. The RG1 and 2DF1 (which have 32% solidity) results were similar to those in LV2012, which validates our current DNS calculations.

However, channels with aspect ratio 5:1:1 were later adopted to see the turbulence development further downstream – RG2, 2DF2, and 3DS2. The 3DS2 grid, has maximum blockage ratio of 15%. The sensitivity of the turbulence to the blockage ratio was examined by changes to the largest scale co-frame Z_0, keeping all other parameters the same. The thickness of the bars, d_0, was increased, so that in 3DS3 we have $\sigma_{3DS3} = 24\%$, and in the 3DS4 we have, $\sigma_{3DS4} = 32\%$.

Then, the sensitivity of the turbulence to the ordering of the frames was examined, starting from 3DS4 as the base case, such that in 3DS5 we have the order $\{Z_1, Z_2, Z_0\}$ thus $\{\sigma_0, \sigma_1, \sigma_2\} = \{15\%, 15\%, 32\%\}$, and in the 3DS6 we have the order $\{Z_2, Z_0, Z_1\}$ thus $\{\sigma_0, \sigma_1, \sigma_2\} = \{15\%, 32\%, 15\%\}$. Note that in the 3DS4, 3DS5, and 3DS6 we have $\sigma_{3DS}^{max} = 32\%$.

The results show remarkable sensitivity of the turbulence to the system parameters, and significant difference in the turbulence characteristics generated by the 3DS as compared to the Regular Grid RG and the flat fractal grids 2DF.

The peak turbulence intensities from the 3DS2 were much lower than in the RG1 and 2DF1 especially away from the centerline in the near-field region close to the grids; but the turbulence intensity persisted at a level comparable to the 2DF far downstream.

The peak intensities generated in the 3DS4 (32%) is the highest yet observed in any grid system, at times nearly twice the intensity in the 2DF peaking at more than 60% away from the centerline in the near-field region. Furthermore, in the turbulence persisted far downstream at a high level of around 15% till the end of the channel. In fact, in the three 32% 3DS grids, in the far-field region $x > 300d_{min}$ the mean flow and the turbulence intensity along the centerline actually increased towards the end of the channel, perhaps due to a high level of entrainment.

The 24% 3DS3 grid approached the profiles observed from the 3DS4, although the peaks were not so high especially along the centerline, and the turbulent spectrum was not so well developed. The significance of this result is that most of the turbulence statistics from 32% grids can be matched to fair approximation from a 24% 3DS grid system. This is important in applications where the blockage ratio, and the associated mean pressure gradient, can be reduced while retaining most of the turbulence. There could be applications where this is an acceptable trade off.

The turbulence also showed some sensitivity to the order of arrangement of the co-frames, although the differences for the same blockage ratio 32% was not as great as between cases with different blockage ratios. The development of fully developed turbulence was best in the 3DS4 grid where the order of co-frames is from large scales to successively smaller and smaller scales. The other orderings, in 3DS5 and 3DS6,

104

for the same maximum blockage ratio of 32% produced lower the peak intensities and the turbulence did not develop such a clear -5/3 spectrum over a wide range of wavenumbers.

Overall, the blockage ratio was the most important parameter in the cases that we investigated.

Broadly, the turbulence downstream can be divided in to three regions. First, the near-grid turbulence production region in the approximate range $0 < x < 50d_{min}$ where the turbulence intensities rise rapidly to their peak values. This is follows by the mid-range region $50 < x < 250$ where the turbulence intensities decrease rapidly. Finally, there is the far-field range $x > 250d_{min}$ where the turbulence appears to be reasonably well mixed, though not entirely homogeneous, and the turbulence intensity appears to be well sustained, at least close to the centerline.

The 3DS systems are characterized by a central core region close to the centerline where the turbulence is reasonable homogeneous and approximately steady in the far-field region. However, far from the central core region in the lateral directions the turbulence dies down. This is important for experiments because in the past, the RG grids have produced fully developed homogeneous and isotropic turbulence but only over a very short near field region. But by optimizing the 3DS parameters, it may be possible to produce a core region over an extended region downstream that is reasonably homogeneous, isotropic, and steady. This could allow such turbulence to be examined more easily and greater detail than in the past.

In view of the limited number of calculations that we have carried out, it is difficult at this stage to draw definitive conclusions on the overall performance of the 3DS.

105

However, a few tentative ideas can be highlighted for future work.

With the sensitivity of the turbulence to system parameters so clearly in evidence, it is critical to find and understand optimal limiting cases, such as which parameter ranges will produce the most turbulence intensity for the minimum pressure gradient; and what parameter settings will produce the best homogeneous turbulence in a core region?

It is important to relate the turbulence statistics in the three regions to the local flow structures. For example, is the length of the near-region directly related to the scale of the vortex structure that arise, or to the length scale of wake interactions?

Does the decay of the turbulence intensity in the mid-region follow a power law decay law – if so, then what is the value of the power law?

Another questions of interest, is what is the mechanism that sustains the turbulence intensity for so long at such a high level downstream in some of the 3DS systems?

5.6   Conclusion

We have investigated, for the first time, the new 3D sparse grid turbulence generator (3DS) which is a system of co-planar arrangement of grids as detailed in [27]. The 3DS possess a much bigger parameter space than previous grid such as the regular grid RG and 2D flat fractal grid 2DF. The 3DS has much lower maximum blockage ratio, $\sigma_{3DS}^{Max} << \sigma_{2DF}$, than the corresponding 2DF grid.

We have examined turbulence characteristics generated by 3DS systems with dif-

ferent σ_{3DS}^{Max} and with different order of the co-frames $[x_0, x_1, x_2] = [Z_0, Z_1, Z_2]$ etc. However, in this study we have kept the inter-frame distances unchanged, $r_1 = 17d_{min}$, $r_2 = 8.5d_{min}$.

In summary we can draw the following conclusions from our numerical investigation.

- For 3DS2, $\sigma_{3DS}^{Max} = 15\% << \sigma_{2DF} = 32\%$, the turbulence intensities are much reduced and the onset of fully developed turbulence is delayed significantly.

- The 3DS3, $\sigma_{3DS}^{Max} = 24\%$, is the closes to the performance of 2DF2 in LV2012.

- The three cases with $\sigma_{3DS}^{Max} = 32\%$- 3DS4, 3DS5 and 3DS6- produced the highest level of peak turbulence intensity yet observed in multi-scale grid systems.

- Fully developed Kolmogorov spectrum $E \sim K^{-5/3}$ was observed in the 3DS4 system.

- In 3DS4, 3DS5 and 3DS6 systems, a central core region around the centerline is observed where the turbulence is approximately homogeneous and isotropic, and turbulence intensity is sustained downstream into the far-field, and even increases most likely due to the re-entrainment of turbulent fluid from the surround regions. To our knowledge this is the first time that such a mechanism is identified for sustained turbulence intensity in such a grid system.

It is clear that, by adjusting different system parameters, we can adjust the fine details of the turbulence produced. This can be useful for control of turbulence in practical applications. For example the 3DS3 (24%) system was close to the 2DF

(32%) system; it may be possible to produce similar turbulence but with lower applied pressure gradient.

In future we will investigate 3DS further for adjustments in various parameters especially inter-frame distances r_1 and r_2.

CHAPTER 6

TURBULENT INERTIAL

PARTICLE PAIR DIFFUSION

It has recently been shown that turbulent fluid particle pair diffusion is governed by local and non-local diffusional processes which produces non-Richardson diffusion regimes in the inertial subrange [N. A. Malik, *PLoS ONE, 13(10): e0202940 (2018)*] . Here, we extended this concept to inertial particle pair diffusion and show that in general this leads to a two parameter family of regimes in which the scale dependent inertial particle pair diffusion coefficients, K_p, are functions of the size of the inertial subrange R_k, and the Stokes' number St, where l is the pair separation variable. Initially the relative diffusion is always ballistic because the inertia dominates over the turbulent energies in the smallest scales. The diffusion then transits sowly over an extended range of scales towards the non-Richardson fluid particle regimes, $K_p \to K_f$; except if the Stokes number is high, $St > R_k$, then the ballistic regimes persist through the entire inertial subrange. By considering the balance of momentum and energies,

the transition length scale l_c at which the ballistic regime starts to transit towards the non-ballistic regimes scales like, $l_c/\eta \sim St^{0.5}$ if $St < 1$, and scales like $l_c/\eta \sim St^1$ if $St > 1$, where η is the Kolmogorov scale; a crossover between these two scalings occurs at $St = 1$. All of these theoretical predictions are confirmed and observed using the Kinematic Simulations (KS) [R. H. Karichnan, *Phys. Fluids 13, 22 (1970)*; N. A. Malik, *PLoS ONE, 10(10): e0189917 (2017)*].

6.1 Introduction

The transport of particles through dispersion and convection is one of the main features of turbulent flows. It is common place in nature, from the movement of particle laden dust storms, clouds, hail, snow, and other forms of percipitation to climate modeling. Pollution from soot, and plastics, in the atmosphere and oceans are mostly in the form of small inertial particles, sometimes chemically reacting. The dispersion of pollens and seeds which are essential for life are inertial particles which are carried by the wind and ocean currents. Turbulent particle transport also plays an important role in many engineering systems wherever turbulence is present, sometimes in multi-phase turbulent systems such as suspensions of droplets, bubbles, and finite-size particles, [36], [37], [38], [39], [40], [41].

Inertial particles deviate from streamlines which makes their transport difficult to model. The transport equations that describe the motion of individual inertial particles is not fully developed yet, although simplified descriptions in specific contexts have been proposed, for example by Maxey & Riley [42] and Reeks [43]. Furthermore,

the suspended particles have drag, and finite size, and densities that are different from that of the carrier fluid, and the interactions between the particle and the underlying flow structures plays an important role in their movement. It is well known, for instance, that heavy particles are expelled out of vortical structures, while light particles tend to concentrate in their cores leading to preferential concentration and the formation of inhomogeneities in the particle distribution [44], [45], [46].

The motion of groups of particles is important in understanding the clustering of particles in to regions of preferential concentration. It is a challenging phenomena caused by particles' interactions with the fluid flow, and has been the subject of a great number of research articles of which [47], [48], [49], [50], [51], [52], [53], [54], [55], [56], [57], [58], [59], [60] is a sample.

Such group dispersion can often be related to the relative motion of particles pair diffusion. In 1926 Richardson [61], [62], [63] proposed a theory for turbulent fluid particle pair diffusion based on a locality hypothesis. However, recently it has been shown that fluid pair diffusion is in fact governed by both local and non-local processes and this leads to different, non-Richardson, scaling laws for the fluid pair diffusion coefficient [64], [27].

The main purpose of this article is to investigate whether the principle of local and non-local diffusional processes can be extended to inertial particle pair diffusion, and to test the new theory numerically using Kinematic Simulations (KS) [65], [66], [67].

In Section II, we summaries fluid particle pair diffusion theory. In Section III, we develop a new theory for turbulent inertial pair diffusion based on the idea of local and of non-local diffusionla processes. In Section IV, we present a theory for the scaling

111

of the transition scale between ballistic and non-ballistic regimes. In Section V, we use KS to simulate inertial particle pair trajectories to test the predictions of the new theory. The KS results are presented in Section VI. We conclude with discussion of the results in Section VII.

All the plots that will be presented here are in color. For interpretation of the references to color in the figure legends, the reader is referred to the web version of this article.

6.2   Fluid Particle Pair Diffusion

Richardson's theory of pair diffusion of fluid particles was based upon the idea of a scale dependent pair diffusivity, $K_f(l)$, where l is the distance between two fluid particles, and on the locality hypothesis which states that only energy in the turbulent scales which are of a similar size to the pair separation itself is effective in further increasing the pair separation. This yields the 4/3-scaling for the pair diffusion coefficient,

$$K_f(l) \quad \sim \quad l^{4/3} \tag{6.1}$$

Obukhov [62] showed that this is equivalent to $\sigma_l^2 = \langle l^2 \rangle \sim t^3$ known as the RO-t^3- regime. $\langle \cdot \rangle$ is the ensemble average. In the ensuing discussions, we follow the usual convention of replacing the scaling on l with its rms value, i.e. $l \sim \sigma_l$.

However, recent studies in turbulent particle pair diffusion [67], [64], [27] has shown that both local and non-local processes govern turbulent pair diffusion. For generalised

112

energy spectrum, $E(k) \sim k^{-p}$, $k_1 < k \leq k_\eta$, $1 < p \leq 3$, in the limit of very large inertial subrange, $R_k = k_\eta/k_1 \to \infty$, the theory predicts the non-Richardson regimes,

$$K_f(l) \quad \sim \quad \sigma_l^\gamma, \ (1+p)/2 < \gamma(p) < 2, \quad \text{as } R_k \to \infty \tag{6.2}$$

where $\gamma(p)$ is intermediate between the purely local, $(1+p)/2$, and the purely non-local, 2, limits.

It was also shown that a second non-Richardson quasi-local regime exists for short inertial subranges, $R_k \approx 10^2$, because then the entire inertial subrange is effectively local to the pair separation,

$$K_f(l) \quad \sim \quad \sigma_l^\gamma, \ \gamma(p) \approx (1+p)/2, \quad \text{for } 1 \ll R_k \ll \infty \tag{6.3}$$

Kinematic Simulations (KS) has verified all of these predictions [27]. For example, it was found that for Kolmogorov spectrum, $E(k) \sim k^{-5/3}$, KS yielded,

$$K_f(l) \quad \sim \quad \sigma_l^{1.525}, \quad \text{for } R_k = 10^6. \tag{6.4}$$

and,

$$K_f(l) \quad \sim \quad \sigma_l^{4/3}, \quad \text{for } R_k = 10^2 \tag{6.5}$$

113
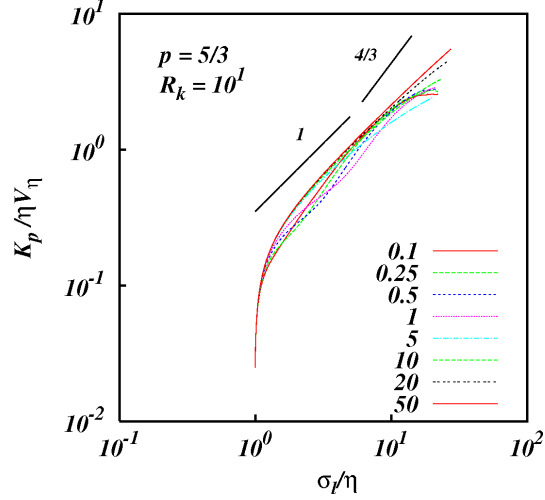
Figure 6.1: Log-log of the inertial pair diffusion coefficient $K_p/\eta v_\eta$ against the rms pair separation σ_l/η from KS simulations with energy spectrum $E(k) \sim k^{-5/3}$ and inertial subrange of size $R_k = 10^1$, and for different Stokes numbers between $St = 0.1$ and 50 as indicated. (For interpretation of the references to color in the figure legend, the reader is referred to the web version of this article.)

For turbulence with intermittent power law spectrum $E(k) \sim k^{-1.72}$, KS yielded,

$$K_f(l) \quad \sim \quad \sigma_l^{1.556}, \quad \text{for } R_k = 10^6. \tag{6.6}$$

and,

$$K_f(l) \quad \sim \quad \sigma_l^{1.43}, \quad \text{for } R_k = 10^2 \tag{6.7}$$

Equation (6.6) is particularly important because this is within 1% of the re-appraised 1926 geophysical dataset, see Fig. 1 in [64].
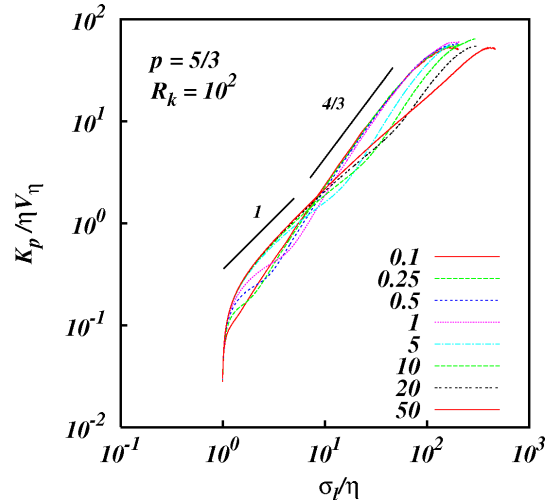
Figure 6.2: Similar to Fig. 1, except for inertial subrange size $R_k = 10^2$.

6.3 Turbulent Inertial Pair Diffusion: a new theory

Diffusion of inertial particle pairs has received some interest in recent works, such as [68], [69], [70], [71] in the limit of Stoke's drag, and Kelken et al [72] who consider inertial particle pair diffusion in the presence of gravity. Bragg et al [73], [74] consider the form of the diffusion coefficient in forward and backward time dispersion. See also [75], [76], [77], [78]. In [74], the diffusion coefficient for inertial particles is derived using PDF phase-space theories, and it involves two contributions, one of which is the second order inertial particle-pair relative velocity structure function, which dominates the behavior of the diffusion coefficient for $St \geq O(1)$ in the dissipation range. This structure function is known to have a power law behavior in the dissipation range, where the exponent is related to the correlation dimension for the inertial particle spatial distribution.
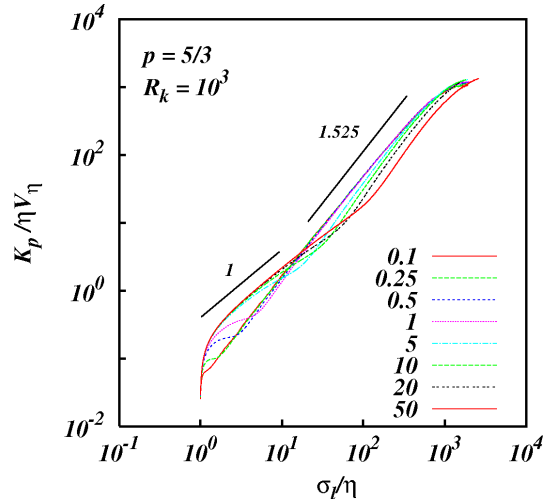
Figure 6.3: Similar to Fig. 1, except for inertial subrange size $R_k = 10^3$.

Here, we focus only on inertial subrange scalings for the inertial pair diffusion coefficient.

Although a general theory for inertia particle transport has not been developed, the theory of Maxey & Riley [42] has gained widespread acceptance. Maxey & Riley's transport equation contains up to seven terms, including terms associated with added mass, density differences, gravity, and memory effects. Like many previous researchers in the field, we neglect all terms except the Stoke's drag term. We investigate turbulent pair diffusion in the inertial subrange for different sizes of the inertial subrange and in the Stokes drag limit.

A particle trajectory is then obtained by integrating the coupled particle tansport equations,

$$\frac{d\vec{x}}{dt} = \vec{v}(t) \tag{6.8}$$

$$\frac{d\vec{v}}{dt} = -\frac{1}{\tau_p}\left(\vec{v}(t) - \vec{u}(\vec{x}, t)\right) \tag{6.9}$$

116
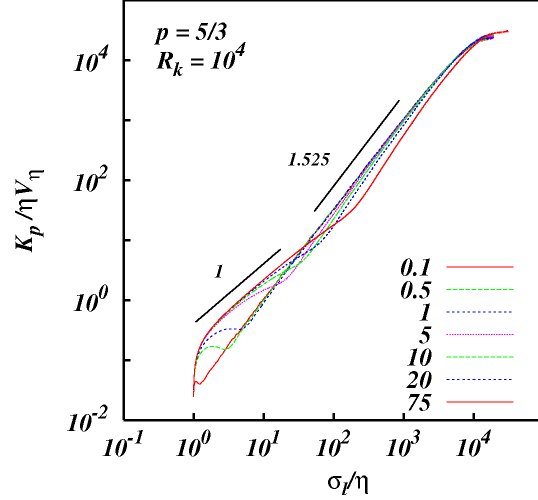
Figure 6.4: Similar to Fig. 1, except for inertial subrange size $R_k = 10^4$, and St between 0.1 and 75 as indicated.

where $\vec{u}(\vec{x}, t)$ is the fluid velocity at $(\vec{x}, t)$, and $\vec{v}(t)$ is the particle velocity at the same location and time, and τ_p is the particle relaxation time which accounts for the particle inertia.

The global Stokes number St is defined to be,

$$St = \frac{\tau_p}{t_\eta} \tag{6.10}$$

where $t_\eta \sim \varepsilon^{-1/3}\eta^{2/3}$ is the Kolmogorov time scale of the turbulence. ε is the rate of energy dissipation per unit mass, and η is the Kolmogorov length scale.

A local Stoke's number $St(l)$, which depends on the local separation, can also be defined as,

$$St(l) = \frac{\tau_p}{t_l} \tag{6.11}$$

117
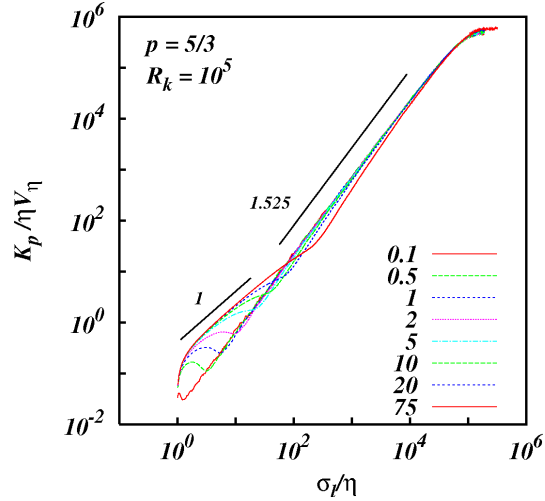
Figure 6.5: Similar to Fig. 1, except for inertial subrange size $R_k = 10^5$, and St between 0.1 and 75 as indicated.

where $t_l \sim \varepsilon^{-1/3} l^{2/3}$ is the turbulence time scale at length scale l.

Equations (6.8) and (6.9) are particle transport equations for inertial particles in a fluid flow – they are not field equations. However, following Richardson's reasoning we will assume that turbulent particle transport can be modelled by a diffusion equation. The correctness of a diffusion equation for turbulent pair diffusion is questionable; however, it is known to be correct in the limit of point source release. We will therefore consider an effective point source release of inertial particles and assume that inertial pair diffusion can be described by a diffusion equation with a scale dependent diffusion coefficient K_p (also called the diffusivity).

In the limit of Stoke's drag, the system of equations (6.8) and (6.9) describes a two-parameter family of diffusion regimes yielding diffusion coefficient, $K_p(l) = K_p(l; St, R_k)$, where St and R_k are the governing parameters; R_k is the size of the

118
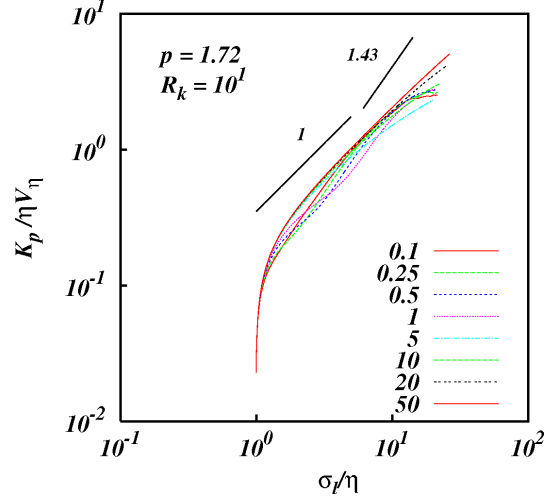
Figure 6.6: Log-log of the inertial pair diffusion coefficient $K_p/\eta v_\eta$ against the rms pair separation σ_l/η from KS simulations with energy spectrum $E(k) \sim k^{-1.72}$ and inertial subrange of size $R_k = 10^1$, and for different Stokes numbers between $St = 0.1$ and 50 as indicated. (For interpretation of the references to color in the figure legend, the reader is referred to the web version of this article.)

inertial subrange which is defined by,

$$R_k \quad \sim \quad \frac{k_\eta}{k_1} \tag{6.12}$$

where the inertial subrange is in the wavenmber range, $k_1 \leq k \leq k_\eta$.

An effective point source release means that the initial separation is small compared to all other length scales in the system; in application, it is sufficient that the initial separation is equal to the Kolmogorov scale, $l_0 = \eta$.

After release, for small separations and for all Stokes numbers $St > 0$ the particle inertia should dominate over the small scale turbulent energy. The motion remains well correlated to its initial conditions, and this should lead to ballistic relative motion

119
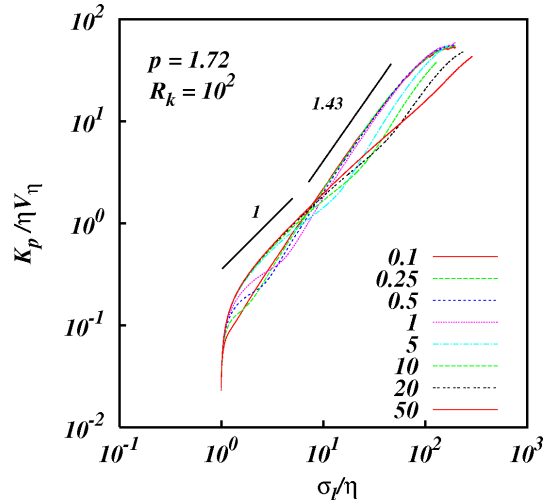
Figure 6.7: Similar to Fig. 6, except for inertial subrange size $R_k = 10^2$.

and a diffusion coefficient that is linear in the separation,

$$K_p \ \sim \ \sigma_l^1, \qquad \sigma_l < \sigma_c. \tag{6.13}$$

Although this relationship should be independent of St and R_k, the length scale up to which this ballistic regime persists is itself a function of these two parameters, $\sigma_c = \sigma_c(St, R_k)$.

If $R_k < \sigma_c/\eta$ then the ballistic regime will persist through the entire inertial subrange. We will show later that this corresponds to the case of very large inertia, $St > R_k$ equation (6.25), when the turbulent energies are not strong enough to force the particles to deviate from their initial conditions.

If $R_k > \sigma_c/\eta$, as the Stokes number increases then the ballistic regime will penetrate further up the inertial subrange before decorrelating with its initial conidtions at the transition scale σ_c. After that, the pair diffusion will then asymptote towards the fluid particle pair regime because the energies in the larger inertial scales begin to

120
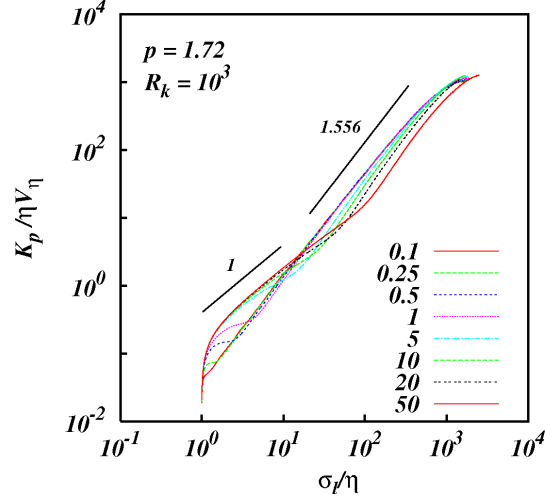
Figure 6.8: Similar to Fig. 6, except for inertial subrange size $R_k = 10^3$.

dominate over the inertia of the particles. Whether this transition occurs quickly or slowly, and how σ_c scales with St are unknown and are questions of interest which we address below. If the Stokes number is small enough the diffusion will attain to the quasi-local fluid particle regimes, equations (6.5) and (6.7).

Thus, for $E(k) \sim k^{-5/3}$ and short inertial subrange, $R_k \approx 10^2$, the new theory predicts that provided $St < R_k$ then,

$$K_p(l) \rightarrow K_f(l) \sim \sigma_l^{1.34}, \qquad \sigma_l \gg \sigma_c, \ R_k \ll \infty \qquad (6.14)$$

and for large inertial subranges the diffusion will asymptote towards the non-local fluid paticle regime, equations (6.4) and (6.6),

$$K_p(l) \rightarrow K_f(l) \sim \sigma_l^{1.525}, \qquad \sigma_l \gg \sigma_c, \ R_k \rightarrow \infty \qquad (6.15)$$
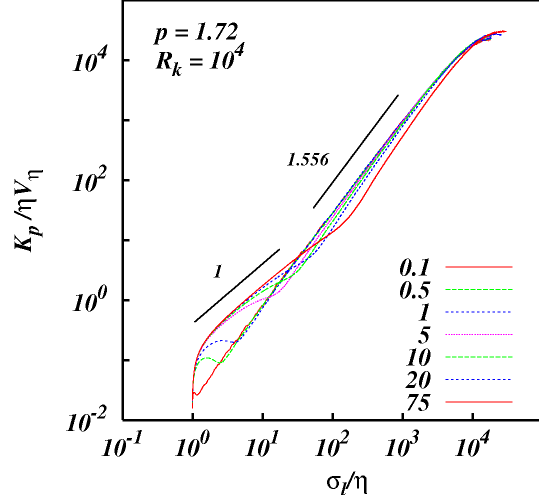
Figure 6.9: Similar to Fig. 6, except for inertial subrange size $R_k = 10^4$, and St between 0.1 and 75 as indicated.

For the intermittent spectrum, $E(k) \sim k^{-1.72}$, these regimes are, respectively,

$$K_p(l) \rightarrow K_f(l) \sim \sigma_l^{1.43}, \qquad \sigma_l \gg \sigma_c, \ R_k \ll \infty \qquad (6.16)$$

and,

$$K_p(l) \rightarrow K_f(l) \sim \sigma_l^{1.556}, \qquad \sigma_l \gg \sigma_c, \ R_k \rightarrow \infty \qquad (6.17)$$

As the Stokes' number increases, $St \rightarrow R_k$ we expect the ballistic regime to penetrate further in to the inertial subrange before transition.

6.4 Transition from ballistic to inertial scaling

An important question is, at what separation after release do the ballistic regimes transition to the non-ballistic regimes? This occurs when the particle pair relative

122
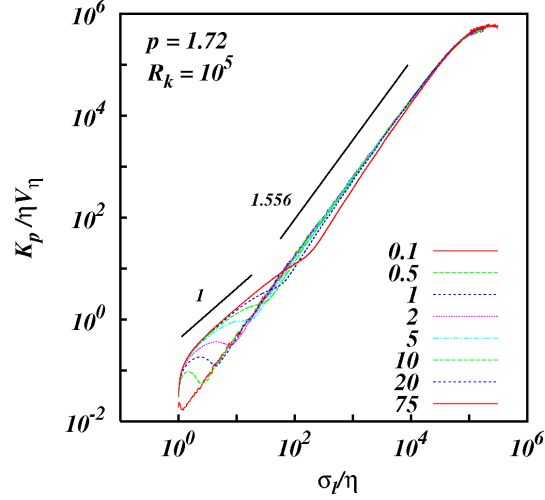
Figure 6.10: Similar to Fig. 6, except for inertial subrange size $R_k = 10^5$, and St between 0.1 and 75 as indicated.

velocity decorrelates with its initial relative velocity. This time we call the transition time, t_c, and the length scale at which this occurs we call the transition scale σ_c.

Bec et al [71] have argued on the basis of locality that the transition will occur when the local time scales of turbulence and inertia are in balance, i.e. when the local Stokes number is unity, $St(\sigma_c) = 1$, which occurs when $t_c = \tau_p$. On this basis, they obtain a scaling between the σ_c and the Stokes number St,

$$\frac{\sigma_c}{\eta} \sim St^{3/2}. \tag{6.18}$$

However, time scales alone do not take in to account the momentum or energy of the particles. Physically, for inertial particles with large Stokes number, $St > 1$, we might expect that their momemtum will cause them to 'punch' their way through the fluid flow independently of the turbulence. If we make the assumption that the relative velocity $v(\sigma_c)$ of the inertial pair when $\sigma_l = \sigma_c$ scales like $\sim \sigma_c/\tau_p$, and that

123

this takes a constant value independent of turbulence characterisics, then we obtain

$$v(\sigma_c) \quad \sim \quad \frac{\sigma_c}{\tau_p} \sim C, \quad \text{for } St > 1. \tag{6.19}$$

This yields,

$$\frac{\sigma_c}{\eta} \frac{\eta}{\tau_\eta} \frac{\tau_\eta}{\tau_p} \quad \sim \quad C, \quad \text{for } St > 1 \tag{6.20}$$

$$\text{or} \quad \frac{\sigma_c}{\eta} \quad \sim \quad St, \quad \text{for } St > 1. \tag{6.21}$$

For small Stokes numbers, $St < 1$, we make the assumption that the inertial particle pair will behave like fluid particle pairs; thus the diffusion coefficient will be approximately the same as the fluid pair diffusion coeffiicient, leading to,

$$K_p(\sigma_c) \quad \approx \quad K_f(\sigma_c), \tag{6.22}$$

$$\text{or} \quad \frac{\sigma_c^2}{\tau_p} \quad \approx \quad \frac{\eta^2}{t_\eta}. \tag{6.23}$$

This leads to the following scaling,

$$\frac{\sigma_c}{\eta} \quad = \quad St^{1/2}, \quad \text{for } St < 1. \tag{6.24}$$

The two regimes in equations (6.21) and equation (6.24) are coincident when $St = 1$, where we can expect a crossover in the scalings.

Note that the assumption in equation (6.22) is consistent with the linear ballistic scaling and with equation (6.19) because, $K_p(\sigma_c) \sim \sigma_c^2/\tau_p \sim C\sigma_c^1$.

124
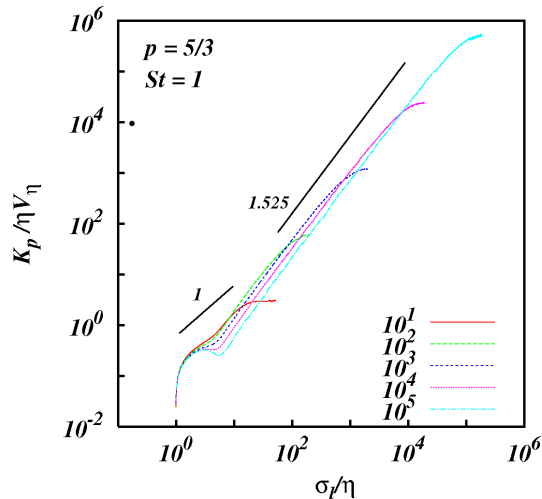
Figure 6.11: Log-log of the inertial pair diffusion coefficient $K_p/\eta v_\eta$ against the rms pair separation σ_l/η from KS simulations with energy spectrum $E(k) \sim k^{-5/3}$ for different inertial subranges as indicated, and for Stokes numbers $St = 1$. (For interpretation of the references to color in the figure legend, the reader is referred to the web version of this article.)

For large Stokes numbers, we can obtain an estimate for the Stokes number needed for the ballistic regime to penetrate through the inertial subrange, by combining $R_k = \sigma_c/\eta$ mentioned earlier with equation (6.21). Together, we find that the ballistic regime will penetrate through the inertial subrange if,

$$St \;>\; R_k. \tag{6.25}$$

6.5   Numerical Simulations

6.5.1   Previous works

The Lagrangian diffusion model Kinematic Simulations (KS) was used to obtain the statistics of particle pair diffusion. KS is an established method, and we refer the
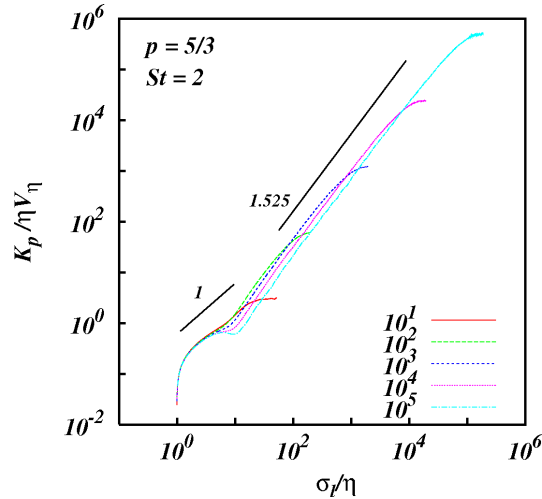
Figure 6.12: Similar to Fig. 11 except for Stokes number $St = 2$.

reader to [65], [66], [67], [79] for details. Here we give a summary of the method.

In KS one specifies the second order Eulerian structure function through the power spectrum $E(k)$ which can take any form. Here we examine Kolmogorov turbulence with $E(k) \sim k^{-5/3}$, and also a case of intermittent turbulence with $E(k) \sim k^{-1.72}$. KS can generate inertial subranges large enough to test pair diffusion scaling laws over extended inertial subranges.

KS generates turbulent-like non-Markovian particle trajectories by releasing particles in flow fields which are prescribed as sums of energy-weighted random Fourier modes. By construction, the velocity fields are incompressible and the energy is distributed among the different modes by a prescribed Eulerian energy spectrum, $E(k)$. The essential idea behind KS is that the flow structures in it - eddying, straining, and streaming zones - are similar to those observed in turbulent flows, although not precisely the same, which is sufficient to generate turbulent-like particle trajectories.

KS has been used to examine single particle diffusion [80], [81], and pair diffusion
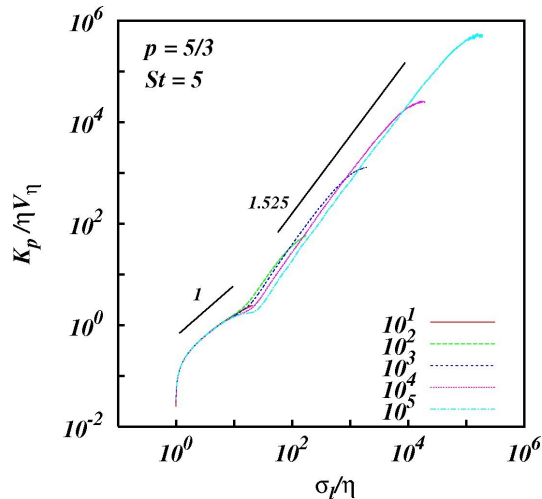
Figure 6.13: Similar to Fig. 11 except for Stokes number $St = 5$.

[66], [82], [83], [25], [84], [64], [27]. KS has also been used in studies of turbulent diffusion of inertial particles [30], [85]. Meneguz & Reeks [30] found that the statistics of the inertial particle segregation in KS generated flow fields for statistically homogeneous isotropic flow fields are similar to those generated by DNS.

KS pair diffusion statistics have been found to produce close agreement with DNS at low Reynolds numbers, incuding the flatness factor of pair separation [25].

Concerns about KS has been expressed because it produces fluid particle pair diffusion scalings that are not consistent with Richardson's 4/3 locality scaling law, [86], [84], [87]. It has been speculated by these authors that this is because KS does not possess the correct dynamical sweeping of the small inertial scales by the large convective scales, leading to larger than expected power law scalings for the diffusion coefficient. However, these concerns have been addressed in [67] where a detailed numerical analysis has shown that such errors are in fact very small and therefore it is the hypothesis of locality that is in error not KS.
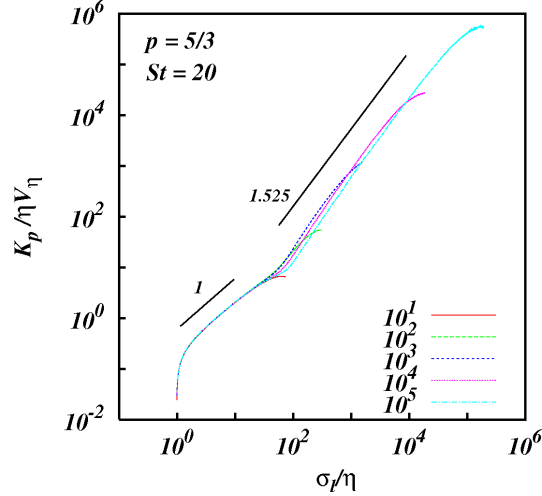
Figure 6.14: Similar to Fig. 11 except for Stokes number $St = 20$.

6.5.2 The KS velocity fields and energy spectra

An individual Eulerian turbulent flow field realization in KS is generated as a truncated Fourier series,

$$
\begin{aligned}
\mathbf{u}(\mathbf{x}, t) \;=\; & \sum_{n=1}^{N_k} \Big((\mathbf{A}_n \times \widehat{\mathbf{k}}_n) \cos(\mathbf{k}_n \cdot \mathbf{x} + \omega_n t) \\
& + \quad (\mathbf{B}_n \times \widehat{\mathbf{k}}_n) \sin(\mathbf{k}_n \cdot \mathbf{x} + \omega_n t) \Big)
\end{aligned}
\tag{6.26}
$$

where N_k is the number of representative wavenumbers, typically hundreds for very long spectral ranges, $R_k \gg 1$. $\hat{\mathbf{k}}_n$ is a random unit vector; $\mathbf{k}_n = k_n \hat{k}_n$ and $k_n = |\mathbf{k}_n|$. The coefficients $\mathbf{A}_n$ and $\mathbf{B}_n$ are chosen such that their orientations are randomly distributed in space and uncorrelated with any other Fourier coefficient or wavenumber, and their amplitudes are determined by $\langle \mathbf{A}_n^2 \rangle = \langle \mathbf{B}_n^2 \rangle \propto E(k_n) dk_n$, where $E(k)$ is the energy spectrum in some wavenumber range $k_1 \leq k \leq k_\eta$. The angled brackets $\langle \cdot \rangle$ denotes the ensemble average over space and over many random flow fields. The associ-

128
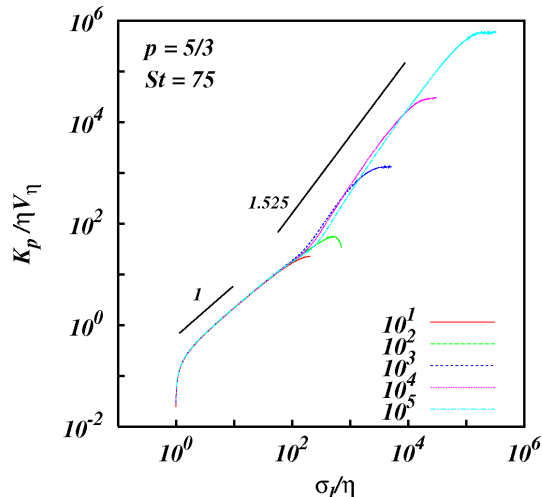
Figure 6.15: Similar to Fig. 11 except for Stokes number $St = 75$.

ated frequencies are proportional to the eddy-turnover frequencies, $\omega_n = \lambda\sqrt{k_n^3 E(k_n)}$. There is some freedom in the choice of λ, so long as $0 \leq \lambda < 1$. The construction in equation (6.26) ensures that the Fourier coefficients are normal to their wavevector which automatically ensures incompressibility of each flow realization, $\nabla \cdot \mathbf{u} = 0$. The flow field ensemble generated in this manner is statistically homogeneous, isotropic, and stationary.

The energy spectrum $E(k)$ can be chosen freely within a finite range of scales, even a piecewise continuous spectrum, or an isolated single mode are possible. To incorporate the effect of large scale sweeping of the inertial scales by the energy containing scales, the simulations are carried out in the sweeping frame of reference by setting $E(k) = 0$ in the largest scales, for $k < k_1$ [67]. We choose the energy spectrum in the inertial subrange to be,

$$E(k) \sim k^{-p}, \qquad k_1 \leq k \leq k_\eta \tag{6.27}$$
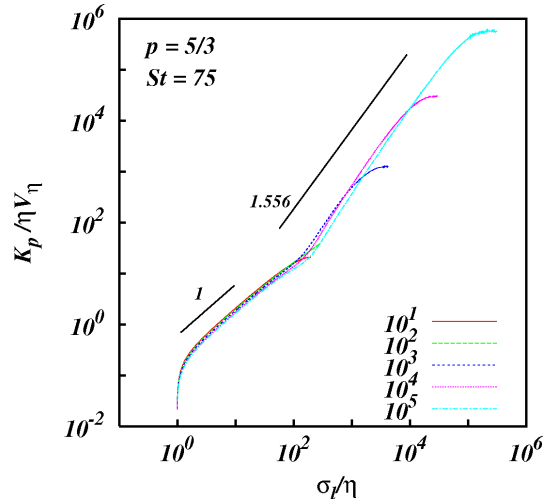
Figure 6.16: Similar to Fig. 11 except from KS with spectrum of $E(k) \sim k^{-1.72}$, and $St = 75$.

for $p = 5/3$ and 1.72. The spectrum is normalised such that the total energy is always equal to, $\int_{k_1}^{k_\eta} E(k)dk = 3/2$. The largest represented scale of turbulence is $2\pi/k_1$ and smallest is the Kolmogorov micro-scale $\eta = 2\pi/k_\eta$.

A particle trajectory, $\mathbf{x}(t)$, is obtained by solving equations (6.8) and (6.9) in time. Pairs of trajectories are harvested from a large ensemble of flow realizations and pair statistics are then obtained from it for analysis.

6.6   Results

6.6.1   Scaling for $K_p(l; St, R_k)$

KS was run for two diferrent spectra, first the Kolmogorov spectrum $E(k) \sim k^{-5/3}$, and then for an intermittent spectrum $E(k) \sim k^{-1.72}$. A parametric study for a wide range of Stokes number and inertial subranges was carried out for the two spectra. Each run contained an ensemble of about 30,000 inertial particle pair trajectories.
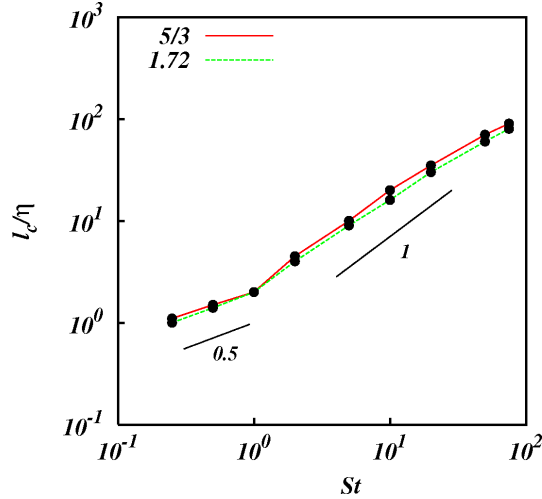
Figure 6.17: Log-log of the pair separation σ_c where transition occurs against the Stokes number St. The cases for $E(k) \sim k^{-5/3}$ and $\sim k^{-1.72}$ are shown. Lines of slope 0.5 and 1 are shown for comparison. (For interpretation of the references to color in the figure legend, the reader is referred to the web version of this article.)

Fig. 1 shows the log-log plot of the inertial pair diffusion coefficient, $K_p/\eta v_\eta$, against the rms separation, σ_l/η, for Kolmogorov turbulence $E(k) \sim k^{-5/3}$, and for an inertial subrange size of $R_k = 10^1$; cases for Stokes number from $St = 0.1$ to 75 are shown. Figs. 2 to 5 are similar to Fig. 1 except for inertial subrange sizes of, $R_k = 10^2$, 10^3, 10^4, and 10^5 repectively.

In these figures, lines of slope 1 are shown for comparison with ballistic motion, and lines of slope 4/3 is shown for comparison with the Richardson's locality hypothesis, and lines of slope 1.525 are shown to compare with the asymptotic fluid pair diffusion for large inertial subranges [27].

The results show initial ballistic regimes, equation (6.13), in all cases. However, the ballistic regimes penetrate further and further in to the inertial subrange as the Stoke's number increases.

The $St = 0.1$ cases are always close to fluid pair diffusion.

For very large Stokes numbers the ballistic regimes penetrate through the entire inertial subrange.

In Fig. 1, the inertial subrange is too short, $R_k = 10^1$, to observe inertial subrange scalings.

In Figs. 2 to 5, after the initial ballistic period, either the quasi-local fluid pair diffusion $\sim \sigma_l^{1.34}$ is observed for short inertial subranges and small Stokes number, Fig. 2, or it asymptotes to the fluid non-local regime if the inertial subrange is big enough, $K_p \to K_f \sim \sigma_l^{1.525}$ as $R_k \to \infty$, see [67], [64].

Figs. 6 to 10 for enegy spectrum of $E(k) \sim k^{-1.72}$ show similar trends to Figs. 1 to 5. Lines of slope 1, 1.43, and 1.556 are shown to compare with the asymptotic fluid pair diffusion for large inertial subranges for this spectrum [27].

Inspection of all the plots presented here shows that the the ballistic regimes penetrate the entire the entire inertial subrange if $St > R_k$, to fair approximation, thus confirming the validity of the prediction in eqution (6.25)

The results also show that the transition between the ballistic and fluid pair diffusion regimes, if it occurs, takes place slowly over an extended range of scales.

Finally, it is important to note that it is apparent from Figs. 1-10 that the inertial pair diffusion is initially faster than fluid pair diffusion at small separations, but this behaviour reverses at larger separations. This effect is enhanced as the Stokes number increases. This is probably because initially at very small separations the inertial pair 'punch' their way through the flow like bullets, but later as the turbulence energy begins to dominate at larger separations the inertia acts like a drag on the particle motion thus reducing their realtive diffusivity as compared to fluid pairs at the same

average separation.

6.6.2 Scaling for the transition scale σ_c

The transition scale between the ballistic and non-ballistic regimes is obtained by replotting the results for different R_k, for each Stokes number. Fig. 11 shows the plots for the case $E(k) \sim k^{-5/3}$ and for $St = 1$. The transition point is indentified where the ballistic regimes diverge for the different $R'_k s$. Figs. 12 to 15 are similar except for $St = 2, 5, 20$ and 75 respctively. The results for $E(k) \sim k^{-1.72}$ show a similar trend, and only the cases for $St = 75$, Fig. 16, is shown here.

Fig. 17 shows the plot of σ_c/η against St obtained from the KS results for both spectra as indicated. For $St < 1$, we observe an approximate $\sigma_c/\eta \sim St^{0.5}$ scaling. For $St > 1$ we observe an approximate $\sigma_c/\eta \sim St^1$ scaling. It is apparent in Fig. 18 that the crossover between the two scalings occurs at $St = 1$, as predicted.

These results confirms the theory developed in Section V.

6.7 Discussion

Understanding the transport processes governing turbulent inertial particle motion and their statistical properties is of great importance in many areas of science and engineering. In this aticle, the concept of local and non-local diffusional processes, first ellucidated in [64], [27] has been extended to inertial particle pair diffusion in the inertial subrange. This study is important because of its possible application to the theory and modeling of inertial particle transport and to the spreading of groups

133

of inertial particles, such as in the spread of clouds, percipitation, dust storms, and pollen and pollution dispersion.

In general, inertial particle pair diffusion forms a two parameter family of diffusion regimes characterised by the diffusion coefficient $K_p(l; St, R_k)$, with governing parameters being the Stokes number St and the size of the inertial subrange R_k, and l is the pair separation variable.

The theory developed here predicts short time ballistic regimes where the inertia is dominant, and long time asymptotic regimes approaching fluid particle pair diffusion where the turbulent energy dominates over the inertia, provided that the Stokes number is finite. For very large Stokes number, $St > R_k$, the ballistic regimes penetrate through the entire finite inertial subrange.

All predictions of the theory have been observed and validated using KS for Kolmogorov energy spectrum, $E(k) \sim k^{-5/3}$, and for an intermittent spectrum, $k^{-1.72}$.

For large inertial subranges corresponding to $R_k > St$, the long time regime approches the fluid particle non-local scaling predicted in [64], [27], which justifies our inital assumption of extending the concept of local and non-local diffusional processes to inertial particle pair diffusion.

The scaling for the transition scale σ_c at which the ballistic regime begins to transits asymptotically to the fluid pair diffusion regime differs from the theory of Bec et al [71] who argued that the transition occurs when particle and turbulent frequencies are equal, $St_c = 1$, which leads to the scaling $\sigma_c/\eta \sim St^{3/2}$. Here, we argue that consideration of momentum and energies is more important, and this leads to the scalings $\sigma_c/\eta \sim St^{0.5}$ for $St < 1$, and $\sigma_c/\eta \sim St^1$ for $St > 1$. The results from KS

presented here supports this new theory.

It is important to note that initally the inertial particle pair diffusion is faster than the fluid pair diffusion because the inertial pair 'punch' their way through the small scale turbulent energies like bullets, but this reverses at bigger separations as the tubulent energies increase and dominate the motion because the inertia than most probably acts like a drag thus reducing the diffusion compared to fluid pairs.

APPENDIX A

SUPPLEMENTARY MATERIAL

1. **Dynamical system** A dynamical system is a mathematical description of a real world phenomenon using equations and inequalities with assumptions and conditions.

2. **Trajectory** The path followed by point in a dynamical system.

3. **Flow** The parametric set of trajectories of a dynamical system is called flow.

4. **Continuum** The concept that the fluid continuously distributed and fills the entirety of the region in which it is present. This assumption is vital for the fluid mechanics.

5. **Eddy** An eddy is a structure in flow which carries some mass and momentum of the flow. A vortex is an example of an eddy.

6. **Intermittent** Intermittency is the irregular kinetic energy dissipation which causes a shift in the behavior of the dynamical system.

7. **Autocorrelation** Autocorrelation is a function that describes the memory of a signal.

8. **Structure Function** Structure functions are averages of differences between turbulence quantities measured at different locations in a flow.

9. **Ensemble Average** The average taken over an ensemble of some quantities in a dynamical system over space or time is called ensemble average. It is denoted by $\langle . \rangle$.

10. **Flatness or Kurtosis** It represents a comparison with Gaussian distribution in that higher flatness means sharper peak. Its formula is:

$$F(u) = \frac{\langle u^4 \rangle}{\langle u^2 \rangle^2} \tag{A.1}$$

where $\langle u \rangle$ represents an average and u represents some signal.

11. **Skewness** It is the third moment of fluctuation normalized by the intensity of the signal. Its formula is

$$S(u) = \frac{\langle u'^3 \rangle}{\langle u'^2 \rangle^{\frac{3}{2}}} \tag{A.2}$$

12. **Probability density function (pdf) pdf** of a random variable expresses the probability of finding a particular value of the variable over the range of definition of the variable.

$$\int_{\infty}^{\infty} P(u)\, du = 1 \qquad\qquad (A.3)$$

where $P(u)\, du$ is the probability of a value to be between u and $u + du$. As expected $P(u) \in [0, 1]$.

13. **Power spectral density, PSD** The power spectrum of a signal is a function that gives the power (amplitude) of the signal (usually in decibels, dB) as a function of frequency or wavenumber.

14. **Fractal** An object that has a pattern repeating over different scales.

15. **Fractal Dimension** A fractal dimension is the ratio of some geometric characteristic of self similar patterns having different scales.

16. **Multifractal** Multi-fractal has multiple fractal characteristics.

17. **Stationary** Stationary means that dynamical system is time independent.

18. **Dissipation range** Range of scales over which dissipation occurs is called dissipation range.

19. **DNS** DNS stands for for the direct numerical simulation in which Navier-Stokes Equations are solved without any modeling, on a high resolution mesh to capture all the scales on which turbulence occurs.

20. **Eddy turnover time** The time taken for an eddy to perform one complete rotation.

21. **Eddy Viscosity** The constant of proportionality between turbulent stresses and mean strain rate.

22. **Taylor's Hypothesis** For a moderately turbulent flow, characteristics over space are nearly equal to the characteristics at a point in time.

23. **Energy cascade** Energy cascade refers to the transfer of kinetic energy from large, macroscopic scales of motion, where it is presumed to be input to the flow, through successively smaller scales, ending with viscous dissipation and conversion to heat.

24. **Homogeneous turbulence** Turbulence that is independent of position is called homogeneous turbulence.

25. **Inertial range** The range of scales in a flow where inertial forces are dominant is called inertial range.

26. **Compressibility** The measure of change in volume due to change in pressure.

27. **Isotropic** Turbulence that is independent of direction is called isotropic turbulence.

28. **K41 theory** The K41 theory refers to results published by Kolmogorov in a series of papers in 1941.

29. **LES** LES stands for Large-Eddy Simulation.

30. **RANS** Reynolds-Averaged Navier–Stokes approach for turbulence studies.

31. **Taylor Microscale** The intermediate length scales between the integral scale and the dissipation scale.

32. **Turbulence kinetic energy** Turbulence kinetic energy is the kinetic energy calculated with turbulent fluctuating velocities as given by:

$$k = \sqrt{\frac{\overline{u'^2} + \overline{v'^2} + \overline{w'^2}}{3}} \tag{A.4}$$

33. **Turbulence energy dissipation rate** Turbulence energy dissipation rate is the rate at which turbulence energy is being converted to thermal energy by viscous effects on small scales as given by:

$$\epsilon = \nu \overline{\frac{\partial u_i'}{\partial x_j} \frac{\partial u_i'}{\partial x_j}} \tag{A.5}$$

34. **Equilibrium** We say that turbulent flow has reached equilibrium if production and dissipation of energy balance out. At this point the averaged flow characteristics are consistent and robust.

35. **Weak Solution** Weak solution of a partial differential equation is a solution that satisfies the partial differential equation but all the derivatives involved may not exist.

36. **Strong Solution** Strong solution of a partial differential equation is one which not only satisfies the equation, but all derivatives of all orders exist everywhere.

37. **Vorticity** The curl of velocity is called vorticity.

38. **Enstrophy** The squared L^2 norm vorticity is called enstrophy. It is a measure of the energy density.

39. **Vortex stretching** Vortex deformation due to turbulence where the eddies are visibly stretched is called vortex stretching. It marks a difference between homogeneous and in-homogeneous turbulence.

40. **Reynolds stress** RANS model produces Reynolds stress that effects mean flow just like pressure or viscosity.

41. **Blockage Ratio** Blockage ratio is the ratio between solid area of the grid and frontal area of the model. In a channel flow environment, it is the surface area of the blockage divided by the cross-sectional area of the channel.

42. **Boussinesq hypothesis** The Boussinesq hypothesis states that small-scale turbulent stress should be linearly proportional to the mean strain rates.

43. **Closure** Terms such as Reynolds stress in RANS are such that there is no way to remove the fluctuation from the Reynolds Averaged Navier Stokes Equations and hence require modeling to have a solvable system. This is called the problem of closure.

REFERENCES

[1] J. M. McDonough, "Introductory lectures on turbulence: physics, mathematics and modeling," 2007.

[2] G. K. Batchelor, *An introduction to fluid dynamics.* Cambridge university press, 2000.

[3] L. Prandtl, *The essentials of fluid dynamics.* Blackie & Son Limited, 1963.

[4] G. K. Batchelor, *The theory of homogeneous turbulence.* Cambridge university press, 1953.

[5] S. B. Pope, "Turbulent flows," 2001.

[6] O. K. G. Tietjens and L. Prandtl, *Applied hydro-and aeromechanics: based on lectures of L. Prandtl.* Courier Corporation, 1957, vol. 2.

[7] E. Beutler. New York: McGraw-Hill, 1994, vol. 2, ch. 7, pp. 654–662.

[8] J. Nelson, TWI Report 666/1999, Jan. 1999, required institution missing.

[9] J. Boon, S. Yip, J. Burgers, H. Van de Hulst, S. Chandrasekhar, F. Chen, C. De Loore, D. Frenkel, and B. Smit, *An introduction to fluid mechanics.* Cambridge: Cambridge University Press, 1988.

[10] D. Hurst and J. Vassilicos, "Scalings and decay of fractal-generated turbulence," *Physics of Fluids*, vol. 19, no. 3, p. 035103, 2007.

[11] R. J. Hearst and P. Lavoie, "Decay of turbulence generated by a square-fractal-element grid," *Journal of Fluid Mechanics*, vol. 741, pp. 567–584, 2014.

[12] S. Laizet, J. Nedić, and C. Vassilicos, "Influence of the spatial resolution on fine-scale features in dns of turbulence generated by a single square grid," *International Journal of Computational Fluid Dynamics*, vol. 29, no. 3-5, pp. 286–302, 2015.

[13] S. Laizet, E. Lamballais, and J. Vassilicos, "A numerical strategy to combine high-order schemes, complex geometry and parallel computing for high resolution dns of fractal generated turbulence," *Computers & Fluids*, vol. 39, no. 3, pp. 471–484, 2010.

[14] M. Van Dyke, *Perturbation methods in fluid mechanics.* Academic press New York, 1964, vol. 136.

[15] D. E. Knuth, *Seminumerical Algorithms*, 2nd ed., ser. The Art of Computer Programming. Reading, Massachusetts: Addison-Wesley, 10 Jan. 1981, vol. 2, a full BOOK entry.

[16] J. C. Knvth, "The programming of computer art," Vernier Art Center, Stanford, California, Feb. 1988, a full BOOKLET entry.

[17] L. Davidson, *An introduction to turbulence models*, 1997.

[18] C.-Y. Chow, "An introduction to computational fluid mechanics," *New York, John Wiley and Sons, Inc., 1979. 408 p.*, 1979.

[19] H. Versteeg and W. Malalasekera, "Computational fluid dynamics," *The finite volume method*, 1995.

[20] B. Mazzi and J. C. Vassilicos, "Fractal-generated turbulence," *Journal of Fluid Mechanics*, vol. 502, pp. 65–87, 2004.

[21] W. V. Oz and M. Yannakakis, Eds., *Proc. Fifteenth Annual*, ser. All ACM Conferences, no. 17, ACM.   Boston: Academic Press, Mar. 1983, a full PROCEEDINGS entry.

[22] W. Chow and Y. Cheung, "Comparison of the algorithms piso and simpler for solving pressure-velocity linked equations in simulating compartmental fire," *Numerical Heat Transfer, Part A Applications*, vol. 31, no. 1, pp. 87–112, 1997.

[23] S. Laizet and J. C. Vassilicos, "Direct numerical simulation of fractal-generated turbulence," in *Direct and Large-Eddy Simulation VII*.   Springer, 2010, pp. 17–23.

[24] ——, "Dns of fractal-generated turbulence," *Flow, turbulence and combustion*, vol. 87, no. 4, pp. 673–705, 2011.

[25] N. A. Malik and J. C. Vassilicos, "A lagrangian model for turbulent dispersion with turbulent-like flow structure: comparison with direct numerical simulation for two-particle statistics," *Phys. Fluids*, vol. 11, pp. 1572–1580, 1999.

[26] Y. Nakayama, *Introduction to fluid mechanics*.   Butterworth-Heinemann, 2018.

[27] N. A. Malik, "Turbulent particle pair diffusion: Numeical simulations," *PLoS ONE*, vol. Under review, 2018.

[28] C. L. Fefferman, "Existence and smoothness of the navier-stokes equation," *The millennium prize problems*, vol. 57, p. 67, 2006.

[29] G. K. Batchelor, *The Theory of Homogeneous Turbulence.* Cambridge University Press, 1953.

[30] E. Meneguz and M. W. Reeks, "Statistical properties of particle segregation in homogeneous isotropic turbulence," *J. Fluid Mech.*, vol. 686, pp. 338–351, 2011.

[31] C. M. Venier, C. I. Pairetti, S. M. Damian, and N. M. Nigro, "On the stability analysis of the piso algorithm on collocated grids," *Computers & Fluids*, vol. 147, pp. 25–40, 2017.

[32] I. Demirdžić, Ž. Lilek, and M. Perić, "A collocated finite volume method for predicting flows at all speeds," *International Journal for Numerical Methods in Fluids*, vol. 16, no. 12, pp. 1029–1050, 1993.

[33] H. Kawamura, H. Abe, and K. Shingai, "Dns of turbulence and heat transport in a channel flow with different reynolds and prandtl numbers and boundary conditions," *Turbulence, Heat and Mass Transfer*, vol. 3, pp. 15–32, 2000.

[34] P. Geipel, K. H. Goh, and R. P. Lindstedt, "Fractal-generated turbulence in opposed jet flows," *Flow, turbulence and combustion*, vol. 85, no. 3-4, pp. 397–419, 2010.

[35] R. Seoud and J. Vassilicos, "Dissipation and decay of fractal-generated turbulence," *Physics of Fluids*, vol. 19, no. 10, p. 105108, 2007.

[36] R. A. Shaw, "Particle-turbulence interactions in atmospheric clouds," *Ann. Rev. Fluid Mech.*, vol. 35, pp. 183–227, 2003.

[37] G. Falkovich and A. Pumir, "Sling effect in collision of water droplet in turbulent clouds," *J. Atm. Sci.*, vol. 64, pp. 4497–4505, 2007.

[38] D. L. E. Calzavarini, M. Kerscher and F. Toschi, "Dimensionality and morphology of particle and bubble clusters in turbulent flow," *J. Fluid Mech.*, vol. 607, pp. 13–14, 2008.

[39] F. Toschi and E. Bodenschatz, "Lagrangian properties of particles in turbulence," *Ann. Rev. Fluid Mech.*, vol. 41, pp. 375–404, 2009.

[40] M. S. M. and K.-C. Bergmann. Dordrecht: Springer, 2013.

[41] M. W. Reeks, "Transport, mixing and agglomeration of particles in turbulent flows," *Flow Turb. Combust.*, vol. 92, pp. 3–25, 2014.

[42] M. R. Maxey and J. R. Riley, "Equation of motion for a small rigid sophere in a non-uniform flow," *Phys. Fluids*, vol. 26, p. 883, 1983.

[43] M. W. Reeks, "On a kinetic equation for the transport of particles in turbulent flows," *Phys. Fluids A*, vol. 3, p. 446, 1991.

[44] N. M. Qureshi, M. Bourgoin, C. Baudet, and A. C. Y. Gagne, "Turbulent transport of material particles: An experimental study of finite size effects," *Phys. Rev. Lett.*, vol. 99, p. 184502, 2007.

[45] M. Caporaloni, F. Tampieri, F. Trombetti, and O. Vittori, "Transfer of particles in nonisotropic air turbulence," *J. Atmos. Sci.*, vol. 32, pp. 565–568, 1975.

[46] M. W. Reeks, "The transport of discrete particles in inhomogeneous turbulence," *J. Aerosol. Sci.*, vol. 14, pp. 729–739, 1983.

[47] K. D. Squires and J. K. Eaton, "Preferential concentration of particles by turbulence," *Phys. Fluids A*, vol. 3, pp. 1196–1178, 1991.

[48] L.-P. Wang and R. M. Maxey, "Settling velocity and concentration distribution of heavy particles in homogeneous isotropic turbulence," *J. Fluid Mech.*, vol. 256, pp. 27–68, 1993.

[49] S. Sundaram and L. R. Collins, "Collision statistics in an isotropic particle-laden turbulent suspension. part 1. direct numerical simulations," *J. Fluid Mech.*, vol. 335, pp. 75–109, 1997.

[50] E. Balkovsky, G. Falkovich, and A. Fouxon, "Intermittent distribution of inertial particles in turbulent flows," *Phys. Rev. Lett.*, vol. 86, pp. 2790–2793, 2001.

[51] A. Aliseda, A. Cartellier, F. Hainaux, and J. C. Lasheras, "Effect of preferential concentration on the settling velocity of heavy particles in homogeneous isotropic turbulence," *J. Fluid Mech.*, vol. 468, pp. 77–105, 2002.

[52] G. Falkovich and A. Pumir, "Intermittent distribution of heavy particles in a turbulent flow," *Phys. Fluids*, vol. 16, pp. L47–50, 2004.

[53] O. Simonin, P. Février, and J. Laviéville, "On the spatial distribution of heavy-particle velocities in turbulent flow: from continuous field to particulate chaos," *J. Turbulence*, vol. 3, p. 040, 2002.

[54] K. Duncan, B. M. S. Östlund, and M. Wilkinson, "Clustering in mixing flows," *Phys. Rev. Lett.*, vol. 95, p. 240602, 2005.

[55] A. M. Wood, W. Hwang, and J. K. Eaton, "Preferential concentration of particles in homogeneous and isotropic turbulence," *Int. J. Multiphase Flow*, vol. 31, pp. 1220–1230, 2005.

[56] T. Elperin, N. Kleeorin, M. A. Liberman, V. S. L'vov, and I. Rogachevskii, "Clustering of aerosols in atmospheric turbulent flow," *Environ. Fluid Mech.*, vol. 7, p. 173, 2007.

[57] L. I. Zaichik and V. M. Alipchenkov, "Refinement of the probability density function model for preferential concentration of aerosol particles in isotropic turbulence," *Phys. Fluids*, vol. 19, p. 113308, 2007.

[58] E. W. Saw, R. A. Shaw, S. Ayyalasomayajula, P. Y. Chuang, and A. Gylfason, "Inertial clustering of particles in high-reynolds-number turbulence," *Phys. Rev. Lett.*, vol. 100, p. 214501, 2008.

[59] Y. Ammar and M. Reeks, "Agglomeration of inertial particles in a random rotating symmetric straining flow," *Int. J. Multiphase Flow*, vol. 35, pp. 840–853, 2009.

[60] R. H. A. Ijzermans, M. W. Reeks, E. Meneguz, M. Picciotto, and A. Solidati, "Measuring segregation of inertial particles in turbulence by a full lagrangian approach," *Phys. Fluids E*, vol. 80, p. 015302(R), 2010.

[61] L. F. Richardson, "Atmospheric diffusion shown on a distance-neighbour graph," *Proc. Roy. Soc. Lond. A*, vol. 100, pp. 709–737, 1926.

[62] A. Obukhov, "Spectral energy distribution in a turbulent flow," *(Translation : Ministry of Supply. p. 21 1097), Izv. Akad. Xauk. SSSR. Ser. Geogr. i Geojz*, vol. 5, pp. 453–466, 1941.

[63] G. K. Batchelor, "Diffusion in a field of homogeneous turbulence: Ii. the relative motion of particles," *Math. Proc. Camb. Philos. Soc.*, vol. 48(2), pp. 345–362, 1952.

[64] N. A. Malik, "Turbulent particle pair diffusion: A theory based on local and non-local diffusional processes," *PLoS ONE*, vol. 13(10), p. e0202940, 2018.

[65] R. H. Kraichnan, "Diffusion by a random velocity field," *Phys. Fluids*, vol. 13, pp. 22–31, 1970.

[66] J. C. H. Fung, J. C. R. Hunt, N. A. Malik, and R. J. Perkins, "Kinematic simulation of homogeneous turbulence by unsteady random fourier modes," *J. Fluid Mech.*, vol. 236, p. 281, 1992.

[67] N. A. Malik, "Residual sweeping errors in turbulent particle pair diffusion in a lagrangian diffusion model," *PLoS ONE*, vol. 10(10), p. e0189917, 2017.

[68] L. I. Zaichik and V. M. Alipchenkov, "Pair dispersion and preferential concentration of particles in isotropic turbulence," *Phys. Fluids*, vol. 15, pp. 1776–1787, 2003.

[69] A. ElMaihy and F. C. G. A. Nicolleau, "Investigation of the dispersion of heavy-particle pairs and richardson's law using kinematic simulation," *Phys. Rev. E*, vol. 71, p. 046307, 2005.

[70] L. I. Zaichik and V. M. Alipchenkov, "Statistical models for predicting pair dispersion and particle clustering in isotropic turbulence and their applications," *New Journal of Physics*, vol. 11, no. 10, p. 103018, 2009. [Online]. Available: http://stacks.iop.org/1367-2630/11/i=10/a=103018

[71] J. Bec, L. Biferale, A. Lanotte, A. Scagliarini, and F. Toschi, "Turbulent pair dispersion of inertial particles," *J. Fluid Mech.*, vol. 645, pp. 497–528, 2010.

[72] K. Chang, B. J. Malec, and R. A. Shaw, "Turbulent pair dispersion in the presence of gravity," *New J. Physics*, vol. 17(3), p. 033010, 2015.

[73] A. D. Bragg, P. J. Ireland, and L. R. Collins, "Forward and backward in time dispersion of fluid and inertial particles in isotropic turbulence," *Phys. of Fluids*, vol. 28(1), 2016.

[74] A. D. Bragg, "Analysis of the forward and backward in time pair-separation probability density functions for inertial particles in isotropic turbulence," *J. Fluid Mech.*, vol. 830, p. 63192, 2017.

[75] J. Bec, L. Biferale, M. Cencini, A. Lanotte, and F. Toschi, "Intermittency in the velocity distribution of heavy particles in turbulence," *J. Fluid Mech.*, vol. 646, pp. 527–536, 2010.

[76] K. Gustavsson and B. Mehlig, "Distribution of relative velocities in turbulent aerosols," *Phys. Rev. E*, vol. 84, p. 045304, 2011.

[77] K. Gustavsson, S. Vajedi, and B. Mehlig, "Clustering of particles falling in a turbulent flow," *Phys. Rev. Lett.*, vol. 112, p. 214501, 2014.

[78] A. D. Bragg and L. R. Collins, "New insights from comparing statistical theories for inertial particles in turbulence: Ii. relative velocities of particles," *New J. Physics*, vol. 16, p. 055014, 2014.

[79] S. M. Usama and N. A. Malik. Springer, 2018, ch. Turbulent Diffusion of Inertial Particle Pairs such as in Pollen and Sandstorms, p. 259.

[80] C. Turfus and J. C. R. Hunt. Berlin, Heidelberg: Springer, 1987, ch. A stochastic analysis of the displacements of fluid element in inhomogeneous turbulence using Kraichnan's method of random modes, pp. 191–203.

[81] S. Murray, M. F. Lightstone, and S. Tullis, "Single-particle lagrangian and structure statistics in kinematically simulated particle-laden turbulent flows," *Phys. Fluids*, vol. 28, p. 033302, 2016.

[82] N. A. Malik. Dordrecht: Kluwer, 1996, ch. Structural diffusion in 2D and 3D random flows, pp. 619–620.

[83] J. C. H. Fung and J. C. Vassilicos, "Two-particle dispersion in turbulent-like flows," *Phys. Rev. E*, vol. 57, p. 1677, 1998.

[84] F. C. G. A. Nicolleau and A. F. Nowakowski, "Presence of a richardson's regime in kinematic simulations," *Phys. Rev. E*, vol. 83, p. 056317, 2011.

[85] M. Farhan, F. C. G. A. Nicolleau, and A. F. Nowakowski, "Effect of gravity on clustering patterns and inertial particle attractors in kinematic simulations," *Phys. Rev. E*, vol. 91, p. 043021, 2015.

[86] D. J. Thomson and B. J. Devenish, "Particle pair separation in kinematic simulations," *J. Fluid Mech.*, vol. 526, pp. 277–302, 2005.

[87] G. L. Eyink and B. J. Benveniste, "Suppression of particle dispersion by sweeping effects in synthetic turbulence," *Phys. Rev. E*, vol. 87, p. 023011, 2013.

VITAE

- Name: Syed Muhammad Usama

- Nationality: Pakistani

- Date of Birth: March 08, 1986

- Email: *usama784@gmail.com*

- Permenant Address: House no. 3, Street no. 4, Korang Safari Town, Islamabad 45720, Pakistan

- Ph.D. Mathematics, King Fahd University of Petroleum and Minerals, Dhahran, Saudi Arabia (2014-2019)

- M.S. Matheamtics, COMSATS Institute of Information Technology, Islamabad, Pakistan (2008-2010)

- B.S. Mathematics, COMSATS Institute of Information Technology, Islamabad, Pakistan (2004-2008)

- Pre-Engineering, F.G. Sir Syed College, Rawalpindi, Pakistan (2002-2004)

Publications

- S.M. Usama, J.T. Alverez J.Kopec, K. Kwiatkowski, J. M. Redondo, N.A. Malik, "Turbulence Behind 3D Multi-Scale Sparse Grids", Journal of Physics Conference Series 1101(1):012048, DOI: 10.1088-1742-6596-1101-1-012048, 2018

- S.M. Usama, N.A. Malik, "Turbulent Diffusion of Inertial Particle Pairs Such as in Pollen and Sandstorms", IV AMMCS International Conference, Waterloo, Canada, August 20–25, 2017 and Book Chapter: Recent Advances in Mathematical and Statistical Methods, 10.1007-978-3-319-99719-3-22, 2018

- S.M. Usama, J.T. Alverez J.Kopec, K. Kwiatkowski, J. M. Redondo, N.A. Malik, "Fractal Intermittent Wakes in a Wind Tunnel", Topical Problems of Fluid Mechanics, 10.14311-TPFM.2018.033, 2018

- S.M. Usama, N.A. Malik, "Turbulent Diffusion of Inertial Particle Pairs such as in Pollen and Sandstorms", AMMCS-2017 International Conference: Applied Mathematics, Modeling and Computational Science Conference, 2017

- S.M. Usama, N.A. Malik, "Turbulence Generated by 3D Sparse Multi-Scale Grids with Low Blockage Ratio", AMMCS-2017 International Conference: Applied Mathematics, Modeling and Computational Science Conference, 2017

154

- S.M. Usama, J.T. Alverez J.Kopec, K. Kwiatkowski, J. M. Redondo, N.A. Malik, "Mixing and Turbulence Generated by 3D Sparse Multi-Scale Grid", The 4th Applied Mathematics, Modeling, and Simulation International Conference, 10.13140-RG.2.2.13359.64168, 2017

- S.M. Usama, N.A. Malik, "Turbulent Diffusion of Inertial Particle Pairs such as in Pollen and Sandstorms", The 4th Applied Mathematics, Modeling, and Simulation International Conference, 10.13140-RG.2.2.18392.80645, 2017

- S.M. Usama, N.A. Malik, "Turbulence and Mixing Generated by 3D Sparse Multi-Scale Grid", Abdul Salam International Center for Theoratical Physics Conference, Turbulent Mixing and Beyond, Triest, Italy, 2017

- N.A. Malik, Y.T. Terada, S.M. Usama, "Particle pair diffusion of inertial particles such as dust in the atmosphere", European Geo-sciences Union, General Assembly, Volume: 18, EGU2016-7264, 2016